Surface-Plasmon-Polariton-Waveguide Superluminescent Diode: Design, Modeling and Simulation

SURFACE-PLASMON-POLARITON-WAVEGUIDE SUPERLUMINESCENT DIODE: DESIGN, MODELING AND SIMULATION

BY

MEHDI RANJBARAN, M.Sc.

A THESIS

SUBMITTED TO THE DEPARTMENT OF ELECTRICAL & COMPUTER ENGINEERING

AND THE SCHOOL OF GRADUATE STUDIES

OF MCMASTER UNIVERSITY

IN PARTIAL FULFILMENT OF THE REQUIREMENTS

FOR THE DEGREE OF

DOCTOR OF PHILOSOPHY

Doctor of Philosophy (2012) McMaster University

(Electrical & Computer Engineering) Hamilton, Ontario, Canada

TITLE:	Surface-Plasmon-Polariton-Waveguide Superluminescent Diode: Design, Modeling and Simulation
AUTHOR:	Mehdi Ranjbaran M.Sc. (Sharif University of Technology, Iran) B.Sc. (Isfahan University of Technology, Iran)
SUPERVISOR:	Prof. X. Li, Department of Electrical and Computer Engineering
NUMBER OF PAGES:	xxi, 152

To my dear parents and beloved wife

Abstract

Since the inception of integrated electronic circuits there has been a trend of miniaturizing as many electronic, optical and even mechanical circuits and systems as possible. For optical applications this naturally led to the invention of semiconductor optical sources such as the laser diode (LD) and the light emitting diode (LED). A third device, the superluminescent diode was later invented to offer an output with a power similar to that of an LD and spectral width similar to that of an LED. However, there is usually a trade off between the output power and spectral width of the generated beam. The main challenge in the development of SLD is, therefore, finding ways to mitigate the power-spectral linewidth trade off.

Previous work has two major directions. In the first one the goal is to eliminate facet reflections thus preventing lasing from happening. The detrimental effect of lasing is that even before it starts the spectral width quickly narrows down. In the second research direction the goal is to make the material gain spectrum wider by playing with different parameters of quantum well active regions.

This research work explores yet another way of broadening output spectrum of SLD while allowing the power to increase at the same time. The surface-plasmon waveguide (SPWG) has been proposed to replace the dielectric waveguide, for the first time. A novel SPWG structure is introduced and designed to optimize the

device performance in terms of the output power, spectral width and their product known as the power-linewidth product. The effect of different parameters of the new structure on the output light is investigated and attention is given to the high power, high spectral width and high power-linewidth product regimes.

Notation and abbreviations

AR	active region
ARC or AR coating	antireflection coating
ASE	amplified spontaneous emission
BC	boundary condition
CMC	cladding-metal-cladding
CBMBC	cladding-buffer-metal-buffer-cladding
CS	cross section
DFB	distributed feedback
FWHM	full width at half maximum
FP	Fabry-Perot
IMI	insulator-metal-insulator
LD	laser diode
LED	light emitting diode
LRSP	long range surface plasmon
LSHB	longitudinal spatial hole burning
MIM	metal-insulator-metal
MQW	multi-quantum well

PL	power-linewidth
QW	quantum well
SERS	surface enhanced Raman scattering
SHB	spatial hole burning
SLD	superluminescent diode
SOA	semiconductor optical amplifier
SP	surface plasmon
SPP	surface plasmon polariton
SPWG	surface plasmon waveguide
SRSP	short range surface plasmon
TE	transverse electric
TM	transverse magnetic
TW	traveling wave
A	Shockley-Reed-Hall recombination rate [1/s],
	active region cross section area [m^2]
A_{eff}	effective active area [m^2]
B	bimolecular recombination rate [m^3/s]
C	Auger recombination rate [m^6/s]
b	dipole decay rate (damping coefficient) [1/s]
$\hat{b}_{\perp,r}$	normalized radiative decay rate of perpendicular dipole [1/s]
$\hat{b}_{\perp,nr}$	normalized nonradiative decay rate of
	perpendicular dipole [1/s]
$\hat{b}_{\|\|,r}$	normalized radiative decay rate of parallel dipole [1/s]
$\hat{b}_{\|\|,nr}$	normalized nonradiative decay rate of parallel dipole [1/s]

c	speed of light in free space
d_z	length of a device subsection [m]
E	electric field intensity [V/m]
E_i, E_r, E_t	incident, reflected and transmitted electric field amplitueds [V/m]
E_i^+, E_i^-	electric field wave of region i propagating in the +/- direction [V/m]
$E_{f,r}$	forward/backward complex traveling electric fields [$1/\text{cm}^{3/2}$]
E_g	bandgap energy [J]
E_{en}, E_{hm}	conduction and valence subband energies [J]
E_{hm}^{en}	conduction/valence subband energy difference [J]
e	magnitude of the electron charge [C]
F_c, F_v	quasi-Fermi energy levels [J]
f_c, f_v	Fermi-Dirac distribution functions
f_c^n, f_v^m	Fermi-Dirac distribution functions for QW
G	device gain
g	material optical gain [1/m]
g_0	peak material gain [1/m]
H	magnetic field intensity [A/m]
H_i, H_r, H_t	incident, reflected and transmitted magnetic field amplitueds [A/m]
H_i^+, H_i^-	magnetic field wave of region i propagating in the +/- direction [A/m]
h	Planck constnt [Js]

$\hbar$	reduced Planck constnt [Js]
h_c	cutoff thickness [m]
I	electric current [A]
I_{hm}^{en}	conduction-valence overlap integral
J	electric current density [A/m^2]
$J_m(\cdot)$	Bessel function of the first kind and m-th order
k	wavenumber [rad/m]
k_B	Boltzmann constant [J/K]
L, w, d	device length, width and thickness [m]
L_x	quantum well width [m]
M_b^2	bulk momentum matrix element
M_{if}	momentum matrix element
m	effective dipole mass [Kg]
m_0	free electron mass [Kg]
m_e, m_h	effective electron and hole masses [Kg]
m_{hh}, m_{lh}	effective heavy hole and light hole masses [Kg]
m_r	reduced mass [Kg]
N	carrier density [1/m^3]
N_t	transparency carrier density [1/m^3]
n	refractive index
n_{eff}	effective index of optical mode
n_g	group refractive index
n_{sp}	population inversion factor
$P_{f,r}$	forward/backward traveling optical power waves [J/s]

$P^s_{f,r}$	forward/backward traveling optical spontaneously emitted power waves [J/s]
P_{out}	output facet power [W]
q	dipole moment [C·m]
R_r, R_l	power reflectivities of right and left facets
$R^{\|\|}$, r_{TM}	Fresnel reflection coefficient of TM polarized plane wave
$R^{\perp}$, r_{TE}	Fresnel reflection coefficient of TE polarized plane wave
R_{sp}	spontaneous photon generation rate [1/cm^{3}s]
R_{spon}	spontaneous emission rate per unit energy [1/cm^{3}sJ]
R_{TE}	TE plane wave reflectivity
R_{TM}	TM plane wave reflectivity
$\tilde{s}_{f,r}$	spontaneous emission contribution in the full-wave model [1/cm$^{5/2}$]
R_{stim}	stimulated recombination rate [1/cm^3·s]
T	absolute temperature [K]
T_{TE}	TE plane wave transmissivity
T_{TM}	TM plane wave transmissivity
t_b	buffer layer thickness [m]
t_{TE}	Fresnel transmission coefficient of TE polarized plane wave
r_{TM}	Fresnel transmission coefficient of TM polarized plane wave
v_g	wave packet group velocity [m/s]
y_0	free space wave impedance [Ω]
x, y, z	Cartesian coordinate variables [m]
α	optical propagation loss coefficient [1/m]

α_m	linewidth enhancement factor
β	spontaneous emission coupling factor
β'	real part of modal propagation constant [1/m]
β''	imaginary part of modal propagation constant [1/m]
Δz, Δt	space [m] and time [s] increments
$\Delta\lambda_{FWHM}$	full width at half maximum of Gaussian approximated spectrum of output power [m]
$\delta(\cdot)$	dirac delta function
δ_{mn}	Kronecker delta function
Γ	confinement factor, or, linewidth factor of gain profile
γ	complex propagation constant [1/m]
ϵ_0	permittivity of free space [F/m]
ϵ	relative permittivity
η	quantum yield of dipole emitting state, or injection efficiency
ϕ	scalar potential field [V]
λ	wavelength [m]
λ_k	central wavelength of k-th spectral subsection [m]
λ_p	peak gain wavelength [m]
λ_w	half width of parabolic gain profile [m]
μ	permeability [H/m]
ν_k	width of k-th spectral subsection [Hz]
τ	dipole life time [s]
Ω	solid angle [sr]
ω	angular frequency [rad/s],or complex dipole frequency [rad/s]

ω_p	plasma frequency [rad/s]
Π	Hertz vector potential [Vm]
ρ_r	reduced density of states [$1/\mathrm{m}^3\mathrm{J}$]
ρ_r^{2D}	2D reduced density of states [$1/\mathrm{m}^2\mathrm{J}$]
ρ, ϕ, z	cylindrical coordinate variables [m], [rad], [m]

Contents

List of Figures

List of Tables

Chapter 1

Introduction

1.1 Motivation

Superluminescent diode (SLD) is a semiconductor light source which was invented in the 1970s and mainly developed in the 1980s [2, 3]. It is essentially, a forward biased pn junction with an optically active region (AR) where electrons and holes meet to first recombine spontaneously and generate initial photon seeds. Some of these photon seeds are, then, captured by a waveguide and are amplified as they propagate toward the facets. This amplified spontaneous emission (ASE) is the result of the broadband optical gain in the AR achieved through the stimulated recombination process. If reflection from facets is avoided the amplified photons leave the device forming a spectrally broadband radiation. Also, since the generated light is directed by a waveguide, the output is a well-defined beam. In other words, SLD output is spectrally incoherent, but spatially coherent.

A good SLD is supposed to have a smooth low-ripple broadband spectrum and a sufficiently high power output beam. These are exactly the characteristics demanded

by a number of applications including optical coherence tomography (OCT), fibre optic gyroscopes, fibre optic sensors and optical testings [4–7]. In these applications, usually, a high output power is needed for better signal to noise ratio and a broad spectrum is needed for a better resolution.

Compared to laser diode (LD), SLD has a broader spectrum and less power with equal structure and injection current. The reason is that the lasing action which is the main contributor to the LD output power is avoided in SLD and the output of SLD contains photons that have been exposed to single pass amplification. Therefore, to have a significant output power the injection current of SLD is usually high (several tens or even hundreds of mAmps). In LED, on the other hand, photons generated spontaneously escape from every direction and do not undergo amplification. Since amplification makes the spectrum narrower, LED usually has lower power, but broader spectrum than SLD does. Therefore, SLD is a device where output power and spectral width compete.

An important challenge in the design and fabrication of SLD is to minimize the optical feedback. Residual facet reflection makes the spectrum narrower, brings ripples on the spectrum (spectral modulation) and gives rise to cavity modes which can lead to lasing for some modes and creating spikes in the spectrum. In a severe situation it could even damage the device, because, as mentioned above, SLD is usually a high gain device. To control facet reflections one or more of these techniques are often used: a) tilting the waveguide so that the waveguide is not perpendicular to the facets and reflections from facets do not couple back to the waveguide [8]; b) adding a section at one end of the device which provides optical loss rather than gain [9]. The section attenuates the optical field as it propagates toward the end of the

section. The loss section is usually realized by cutting the injection current to the active region; c) coating facets with antireflection layers.

A one dimensional analysis of SLD in reference [10] gives simple analytical expressions relating the output power and the spectral width to several operational and structural parameters under the assumptions of parabolic gain profile and zero facet reflectivities. Although these assumptions make the resulting expressions not applicable to all SLDs with different structures, the general implications understood are qualitatively valid. It has been shown that the output power is characterized by a peak value of [10]

$$P_p = \frac{2\beta\, n_{sp}\, h\, c^2}{\lambda_p^3}\, \exp\{-\alpha L + G(N)\} \tag{1.1}$$

and a Gaussian-like spectrum with a full-width at half-maximum (FWHM) of

$$\Delta\lambda_{FWHM} \propto \frac{\lambda_w(N)}{\sqrt{G(N)}} \tag{1.2}$$

Parameters in (1.1) and (1.2) are: h the Planck constant; c the speed of light in vacuum; β portion of the spontaneously emitted light coupled to the guided wave; n_{sp} the population inversion factor; λ_p the peak-gain wavelength; λ_w half width of the parabolic material gain profile (full width defined by zero crossing points); α the modal loss; L the device length; N the carrier density; and, G the total device gain given by [10]

$$G(N) = L\Gamma g_0(N) \tag{1.3}$$

in which Γ is the confinement factor and g_0 is the peak material gain.

As seen from (1.2) the spectral width of material gain profile has a direct effect on the spectral width of the output light. To make the gain profile wider a mainstream trend is engineering material and structure of multi-quantum well (MQW) active regions such as using asymmetric MQW stack where different quantum wells have partly overlapping luminescence spectra such that their superposition make a broad profile [11, 12].

According to (1.1)-(1.3) an attempt to increase the output power by increasing the device length will reduce the spectral width. This shows that there is a tradeoff between output power and spectral width. When the injection current (and consequently carrier density) is increased, however, two counter acting effects take place: the total device gain $G(N)$ increases because material gain increases and the gain profile becomes broader due to the so called band-filling effect. The first effect, as seen from (1.2), tends to reduce the spectral width, λ_{FWHM}, while the second one increases it. Whichever effect wins the competition determines whether λ_{FWHM} will increase or decrease. Therefore, for an optimized material gain profile, if the spectral width sets an upper limit on total device gain, output power cannot be further increased. Equation (1.1) also shows that the peak power is directly affected by β (usually referred to as the spontaneous emission coupling factor). This suggests that increasing β can increase the output power without sacrificing the spectral width.

Photons generated by the spontaneous recombination of carriers assume all directions and a wide range of wavelengths. In an SLD with a dielectric waveguide only a small fraction of these photons couple to the guided modes resulting in a small β. The nature of small spontaneous emission coupling to a dielectric waveguide can be explained by using a ray optical model. Spontaneously generated photons inside a

dielectric waveguide are assumed to be rays incident on the core-cladding interface. Firstly, only rays with angles greater than the critical angle will have a chance to remain inside the waveguide (total internal reflection condition). Moreover, guided modes supported by a dielectric waveguide must satisfy the transverse resonance condition [13]. This further limits the acceptable angles of incidence to a set of discrete values. Another type of optical waveguides considered in the thesis (see Chapter 2), namely, surface plasmon waveguides (SPWG) do not have these requirements and are expected to present higher spontaneous emission coupling factors. The purpose of this research was to find the spontaneous emission coupling factor as well as other parameters important to SLD operation such as optical loss and confinement factor for some types of SPWGs. These parameters are, then, used to simulate the performance of an SLD in which the dielectric waveguide has been replaced with SPWG. An SLD with a new SPWG structure is proposed and its performance is compared with a similar device equipped with a dielectric waveguide.

1.2 Organization of the thesis

In the following chapters, first, important elements in operation of superluminescent diode are discussed. These elements have direct influences on the power and spectral linewidth characteristics of the output light and are each represented by a parameter in a physics-based device model. Calculated parameters are, next, used in a device operation simulation model to obtain device output characteristics. These characteristics are, then, compared between a conventional SLD (with dielectric waveguide) and the proposed SPWG device. Chapter 2 introduces some of the most important planar SPWG structures. Attention is paid to modes, their propagation constants

and propagation loss coefficients.

In Chapter 3 the coupling of spontaneously generated photons to SPWG is looked at as an electromagnetic problem. The result is a model for calculating the 'spontaneous emission coupling factor' (β parameter in (1.1)) whose importance is already discussed.

Chapter 4 addresses the optical wave reflection from device facets. To get output with maximum spectral width it is absolutely necessary to avoid facet reflection as much as possible. The chapter briefly reviews the common practiced methods of facet reflection suppression including the antireflection (AR) coating. Then, a method of design for two-layer wide-band AR coatings is discussed in detail. The reflectivities of some example designs are examined.

Once the necessary parameters are obtained, a model is need to simulate the device operation. The model must be able to handle the wide band output of SLD. Hence, the narrow band models used for simulating laser diode are not suitable. A multi wavelength time domain method is presented in Chapter 5 and its capabilities are shown by putting it into work for a dielectric waveguide SLD.

In Chapter 6 a SPWG structure is, for the first time, proposed to be implemented in SLD. Next, equipped with the necessary tools of calculating device parameters and simulation of its operation, the output characteristics of the proposed device are investigated and compared to those of a conventional device.

Chapter 2

Surface Plasmon Waveguides

2.1 Plasmonics

'Plasmonics' is a relatively new term in Optics which refers to applications or phenomena in which surface plasmons (SP) are involved [14, 15]. SPs are the interaction of surface electrons of metals with electromagnetic fields. Although the difference between the behaviour of surface electrons and those in the bulk of metals has been known for a long time, only recently have scientists and engineers of several disciplines turned their attention to these peculiarities and their applications. This is because advances in technology have allowed fabrication and patterning of metallic structures in nanometre scale. SPs are of either propagating or localized type.

2.1.1 Propagating SPs

SPs can propagate along metal/dielectric interfaces of metallic objects. Unlike dielectric waveguides in which the optical field is trapped in a region with a refractive index

usually higher than that in the surrounding media, SPs propagate along interfaces. The simplest example is a two dimensional planar interface of a metal and a dielectric [16]. While propagating, the electromagnetic field is confined at the interface decaying exponentially in both metal and dielectric in the direction perpendicular to the interface. The interfaces can have more complicated geometries or even be patterned (grating). For certain geometries the above mentioned exponential decay of electromagnetic field can be exploited to make surface plasmon waveguides with cross sections of only a few nanometres. An example is a very thin dielectric film sandwiched between metal claddings (MIM structure) [17]. Since fields diminish in metal much faster than they do in dielectric, the effective thickness of this type of waveguide is just a few nanometres. Dielectric waveguides, on the other hand, have a fundamental limit for the mode size, the diffraction limit. According to the diffraction limit rule the dimensions of optical mode of a dielectric waveguide cannot be smaller than half the wavelength in the waveguide core [18]. This is a result of an upper limit imposed on the transverse wave numbers in a dielectric waveguide in order for the dispersion equation to be satisfied. Therefore, SP waveguides can replace the conventional dielectric waveguides leading to more compact optical systems.

2.1.2 Localized SPs

If a metallic nanoparticle is illuminated with light, free electrons of the nanoparticle start responding to the electromagnetic field. If, further, the diameter of the particle (let's say a nanosphere) is much smaller than the wavelength of light, the free electrons all move in phase and oscillate with a defined frequency that depends on the shape, size and material of the particle as well as properties of the surrounding medium

and the wavelength of the exciting field. The charge oscillation over a very small distance is theoretically modeled by an electric dipole. Energy builds up in the dipole field to such extent that the near field of the dipole could be enhanced by several orders of magnitude relative to the driving field. This electromagnetic field enhancement resulting from confining free electrons to a very small volume is the basis for a number of applications including single molecule detection [19], microscopy [20] and small particle manipulation [21]. The strong near field of the nanoparticle could easily provoke nonlinear effects which are promising for novel applications such as all optical switching.

Another interesting situation is when metallic nanoparticles are brought close enough to interact with one another. Each particle acts as an electric dipole and couples to adjacent particles. Using this interaction, a one dimensional array of particles has been shown to act as a waveguide [22] with a very small cross section. Sharp bends along this type of waveguide have also been realized [23]. Two dimensional arrays of such particles can be arranged to form gratings with different functionalities [24].

2.2 Single-interface SPWG

Consider a planar interface between two homogeneous media with dielectric constants (relative permitivities) ϵ_1 and ϵ_2 as shown in Fig. 2.1(a). We assume that both media are isotropic, linear, nonmagnetic and sourceless. We seek guided waves along the z direction. In a two dimensional sourceless structure like this ($\partial/\partial y = 0$) the Maxwell curl equations

$$\nabla \times \mathcal{E} = -j\omega\mu\mathcal{H} \tag{2.1}$$

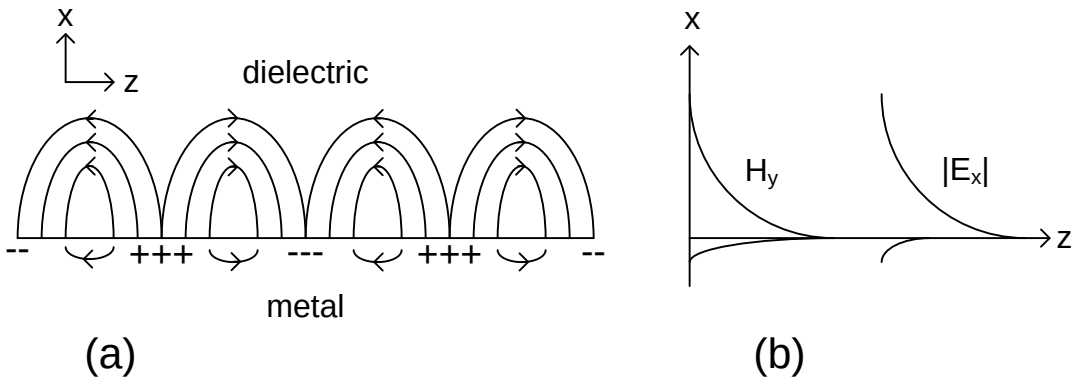

Figure 2.1: (a) Single interface SPWG schematic showing the electric field lines. (b) Amplitudes of magnetic and normal electric fields above and below the interface indicating the penetration depth in each region.

$$\nabla \times \mathcal{H} = j\omega\epsilon\mathcal{E} \tag{2.2}$$

decouple into two sets of equations

TE mode (no z component for electric field):

$$\frac{\partial \mathcal{E}_y}{\partial z} = j\omega\mu\mathcal{H}_x \tag{2.3}$$

$$\frac{\partial \mathcal{E}_y}{\partial x} = -j\omega\mu\mathcal{H}_z \tag{2.4}$$

$$\frac{\partial \mathcal{H}_x}{\partial z} - \frac{\partial \mathcal{H}_z}{\partial x} = j\omega\epsilon\mathcal{E}_y \tag{2.5}$$

TM mode (no z component for magnetic field):

$$\frac{\partial \mathcal{H}_y}{\partial z} = -j\omega\epsilon\mathcal{E}_x \tag{2.6}$$

$$\frac{\partial \mathcal{H}_y}{\partial x} = j\omega\epsilon\mathcal{E}_z \tag{2.7}$$

$$\frac{\partial \mathcal{E}_x}{\partial z} - \frac{\partial \mathcal{E}_z}{\partial x} = -j\omega\mu\mathcal{H}_y \tag{2.8}$$

In the TE case for a guided mode with propagation constant β we separate the z coordinate dependence as

$$\mathcal{E}_y(x,z) = E_y(x)\, e^{-j\beta z} \tag{2.9}$$

Equations (2.3) to (2.5) result in the wave equation

$$\frac{d^2E_y}{dx^2} + (\omega^2\mu\epsilon - \beta^2)E_y = 0 \tag{2.10}$$

The solutions to the wave equation are exponential functions. Taking into account that a physical solution cannot contain unbounded growth as distance increases from the interface we obtain [16]

$$E_y = \begin{cases} A_1 e^{-k_{x1}x} & , \quad x > 0 \\ A_2 e^{k_{x2}x} & , \quad x < 0 \end{cases} \tag{2.11}$$

where A_1 and A_2 are constants and k_x is the x component of the wave vector given by

$$\beta^2 - k_{x\,1,2}^2 = \omega^2\mu\epsilon_0\epsilon_{1,2} \tag{2.12}$$

The interface conditions rule that E_y and H_z (or equivalently $\frac{\partial E_y}{\partial x}$) must be continuous at $x = 0$. The first condition leads to $A_1 = A_2$ which makes the second condition impossible to hold. This means that a single planar interface between two media cannot support TE modes. For the case of TM waves, however, things turn

out to be different. Here we have

$$\frac{d^2H_y}{dx^2} + (\omega^2\mu\epsilon - \beta^2)H_y = 0 \tag{2.13}$$

with the solution

$$H_y = \begin{cases} A_1 e^{-k_{x1}x} & , \quad x > 0 \\ A_2 e^{k_{x2}x} & , \quad x < 0 \end{cases} \tag{2.14}$$

with $k_{x\,1,2}$ given by (2.12). Interface conditions demand H_y and $\frac{1}{\epsilon}\frac{\partial H_y}{\partial x}$ be continuous across the interface leading to $A_1 = A_2$ and

$$\frac{k_{x1}}{\epsilon_1} = -\frac{k_{x2}}{\epsilon_2} \tag{2.15}$$

First, we notice that (2.15) requires ϵ_1 and ϵ_2 have different signs (if they are real). Using (2.12) in (2.15) we find the dispersion equation

$$\beta = k_0\left(\frac{\epsilon_1\epsilon_2}{\epsilon_1 + \epsilon_2}\right)^{\frac{1}{2}} \tag{2.16}$$

where $k_0 = \omega\sqrt{\mu\epsilon_0}$, wave number of vacuum is used. In practice ϵ_1 is commonly a dielectric material with small or negligible loss and $\epsilon_2 = \epsilon_2' - j\epsilon_2''$ is a metal with $\epsilon_2' < 0$ and $|\epsilon_2'| > \epsilon_2''$. In this case real and imaginary parts of the propagation constant in (2.16) can be written as [16]

$$\beta' = k_0\left(\frac{\epsilon_1\epsilon_2'}{\epsilon_1 + \epsilon_2'}\right)^{\frac{1}{2}} \tag{2.17}$$

$$\beta'' = k_0\left(\frac{\epsilon_1\epsilon_2'}{\epsilon_1 + \epsilon_2'}\right)^{\frac{3}{2}} \frac{\epsilon_2''}{2(\epsilon_2')^2} \tag{2.18}$$

For β' to be real we must have $|\epsilon_2'| > \epsilon_1$. β'' reflects the decay of the guided mode due to the loss of metal represented by ϵ_2''. In a metal/dielectric interface collective movement of free electrons of metal at the surface (surface plasmons) can be viewed as the cause of the guided SP mode. Electric field lines at the surface are drawn in Fig. 2.1(a). The field assumes its maximum at the interface and decays exponentially into the two media. For the sake of simplicity, if we assume that the metal is lossless (real negative dielectric constant), then from (2.12) for the decay constant in the dielectric region we have $k_{x1} < \beta$, but in the metal region $k_{x2} > \beta$. This means that the fields decay faster in metal than they do in dielectric. Fig. 2.1(b) shows field profiles of the guided mode.

Fig. 2.2 shows the dispersion curve (frequency vs. propagation constant) of single interface SPWG according to (2.17) for an interface between air and a metal. For simplicity it is assumed that the dielectric function of the metal obeys the lossless Drude model:

$$\epsilon_2 = 1 - (\frac{\omega_p}{\omega})^2 \tag{2.19}$$

in which ω_p is the plasma frequency. For simulation the plasma frequency of silver ($\omega_p = 2\pi \times 2.18 \times 10^{15}\,\mathrm{rad}/s$) is used. The dotted line is the light line in the dielectric material represented by $\omega = \dfrac{kc}{n_1}$ where c is the speed of light in vacuum, n_1 is the refractive index of dielectric region and k is the wavenumber in the dielectric region. Any field whose dispersion curve falls to the right of the light line of dielectric region cannot propagate in that region because of momentum (k) mismatch ('nonradiative' fields), but for regions to the left of light line, field propagates into the dielectric region ('radiative' fields). The dispersion curve of single interface SPWG has two

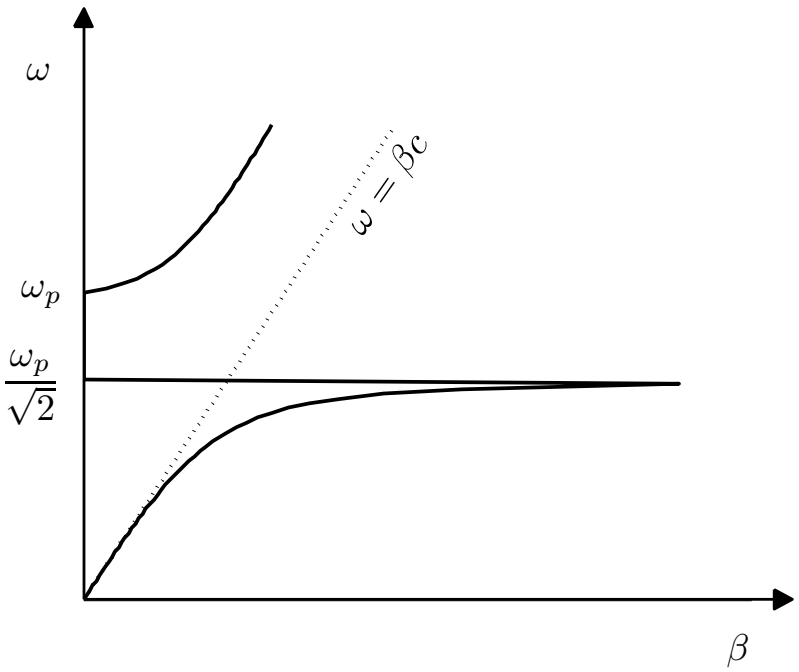

Figure 2.2: Single-interface SPWG dispersion curve.

branches, one nonradiative and the other radiative. There is a singularity at $\omega = \frac{\omega_p}{\sqrt{2}}$ where $|\epsilon_2| = \epsilon_1 = 1$. As frequency increases toward this frequency propagation constant becomes very large and phase and group velocities approach zero. In the realistic case of a lossy metal, however, the propagation constant does not increase unboundedly, but reaches a maximum which depends on the value of loss.

As pointed out before, fields of the surface plasmon mode take on their maximum at the interface and decrease exponentially into the surrounding regions. The distance

at which the fields reach $1/e$ times their maximum (skin depth) is

$$x_d = \begin{cases} \dfrac{1}{k_{x1}} = \dfrac{1}{k_0}\left(\dfrac{\epsilon_1 + \epsilon_2'}{-\epsilon_1^2}\right)^{\frac{1}{2}} , & x > 0 \\ \\ \dfrac{1}{k_{x2}} = \dfrac{1}{k_0}\left(\dfrac{\epsilon_1 + \epsilon_2'}{-\epsilon_2^2}\right)^{\frac{1}{2}} , & x < 0 \end{cases} \tag{2.20}$$

For silver/air interface the skin depth in air at the wavelength of 1.55 μm is $x_1 = 2.65$ μm while in silver it is $x_2 = 22.81$ nm showing that the extension of fields into the dielectric is over 100 times of that in metal.

A major drawback of the single interface SPWG is its modal propagation length due to the metal loss. The imaginary part of the dielectric function of metal makes the propagation constant complex indicating fields decay exponentially as $\exp(-|\beta''|z)$. The propagation length is defined as the distance by which the electromagnetic field intensity attenuates to $1/e$. Since intensity is proportional to $\exp(-2|\beta''|z)$, the propagation length is $L = \dfrac{1}{2|\beta''|}$. Also, $\alpha = 2|\beta''|$ is called the attenuation constant. For the example of silver/air interface at the wavelength of 1.55 μm the propagation length is about 300 μm and the attenuation constant is 33 cm^{-1}. The shallow penetration of field into the metal is enough to cause a large attenuation value that limits the application of single interface SPWG at visible and near infrared wavelengths.

2.3 Thin metallic film SPWG

Now, we investigate the existence of guided modes for a planar double-interface structure depicted in Fig. 2.3. Regions 1 to 3 have refractive indices (dielectric functions)

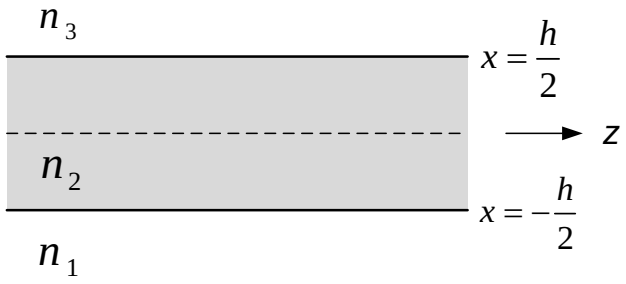

Figure 2.3: Schematic of thin-film SPWG.

$n_1(\epsilon_1)$ to $n_3(\epsilon_3)$, respectively. The film (middle layer) thickness is h and the boundaries of the film are at $x = -\frac{h}{2}$ and $x = \frac{h}{2}$ and$z$ is the propagation direction. The structure is also called IMI (insulator-metal-insulator). We start with the TE mode for which the eigenvalue equation (2.10) has already been found. The solution to the equation applying the radiation boundary condition for regions 1 and 3 is [25]

$$E_y = \begin{cases} A_1 e^{k_{x1}x} & x \leq -\dfrac{h}{2} \\ A_2 \cosh(k_{x2}x) + A_3 \sinh(k_{x2}x) & -\dfrac{h}{2} \leq x \leq \dfrac{h}{2} \\ A_4 e^{-k_{x3}x} & \dfrac{h}{2} \leq x \end{cases} \tag{2.21}$$

in which A_1 to A_4 are constants and wavenumbers k_{x1}, k_{x2} and k_{x3} in the x direction are obtained, as before, from

$$\beta^2 - k_{x\,i}^2 = \omega^2 \mu \epsilon_0 \epsilon_i \ , \qquad i = 1, 2, 3$$

The boundary conditions, again, require E_y and its derivative be continuous across the two interfaces. This gives us four equations in terms of the four unknown constants

A_1 to A_4:

$$\begin{aligned}
&A_1 e^{-k_{x1}\frac{h}{2}} - A_2\cosh(-k_{x2}\frac{h}{2}) - A_3\sinh(-k_{x12}\frac{h}{2}) &&= 0\\
&k_{x1}A_1 e^{-k_{x1}\frac{h}{2}} - k_{x2}A_2\sinh(-k_{x2}\frac{h}{2}) - k_{x2}A_3\cosh(-k_{x12}\frac{h}{2}) &&= 0\\
&A_2\cosh(k_{x2}\frac{h}{2}) + A_3\sinh(k_{x2}\frac{h}{2}) - A_4 e^{-k_{x3}\frac{h}{2}} &&= 0\\
&k_{x2}A_2\sinh(k_{x2}\frac{h}{2}) + k_{x2}A_3\cosh(k_{x2}\frac{h}{2}) + k_{x3}A_4 e^{-k_{x3}\frac{h}{2}} &&= 0
\end{aligned} \tag{2.22}$$

Since the equations are homogenous, in order to have nontrivial solutions for the constants the determinant of the system of equations must be zero:

$$D = \begin{vmatrix}
e^{-k_{x1}\frac{h}{2}} & -\cosh(-k_{x2}\frac{h}{2}) & -\sinh(-k_{x12}\frac{h}{2}) & 0\\
k_{x1}e^{-k_{x1}\frac{h}{2}} & -k_{x2}\sinh(-k_{x2}\frac{h}{2}) & -k_{x2}\cosh(-k_{x12}\frac{h}{2}) & 0\\
0 & \cosh(k_{x2}\frac{h}{2}) & \sinh(k_{x2}\frac{h}{2}) & -e^{-k_{x3}\frac{h}{2}}\\
0 & k_{x2}\sinh(k_{x2}\frac{h}{2}) & k_{x2}\cosh(k_{x2}\frac{h}{2}) & k_{x3}e^{-k_{x3}\frac{h}{2}}
\end{vmatrix} = 0$$

After simplification we have

$$\tanh(k_{x2}h)(1 + \frac{k_{x1}k_{x3}}{k_{x2}^2}) + (\frac{k_{x1}}{k_{x2}} + \frac{k_{x3}}{k_{x2}}) = 0$$

or

$$\tanh(k_{x2}h)(1 + s_1 s_3) + (s_1 + s_3) = 0 \tag{2.23}$$

if we define

$$s_1 = \frac{k_{x1}}{k_{x2}}\,,\; s_3 = \frac{k_{x3}}{k_{x2}} \tag{2.24}$$

Equation (2.23) does not have a solution for β and consequently for k_{x1}, k_{x2} and k_{x3}. We only prove this in the limiting case of lossless waveguide where, k_{x1}, k_{x2}, k_{x3} and

β are all real and positive. In this case, all terms in (2.23) are real and positive and the equation cannot have a real solution for β. Therefore, similar to a single-interface SPWG, a thin film SPWG does not support TE guided modes.

Now, we investigate the existence of TM guided modes for the thin film structure. Here,

$$H_y = \begin{cases} A_1 e^{k_{x1}x} & x \leq -\frac{h}{2} \\ A_2 \cosh(k_{x2}x) + A_3 \sinh(k_{x2}x) & -\frac{h}{2} \leq x \leq \frac{h}{2} \\ A_4 e^{-k_{x3}x} & x \geq \frac{h}{2} \end{cases}$$

with the x-direction wavenumbers given by

$$\beta^2 - k_{x\,i}^2 = \omega^2 \mu \epsilon_0 \epsilon_i \quad , \qquad i = 1, 2, 3 \tag{2.25}$$

Next, boundary conditions are applied on the two interfaces. These are the continuity of H_y and $\frac{1}{\epsilon}\frac{dH_y}{dx}$ which generate four equations:

$$\begin{cases} A_1 e^{-k_{x1}\frac{h}{2}} - A_2 \cosh(-k_{x2}\frac{h}{2}) - A_3 \sinh(-k_{x12}\frac{h}{2}) = 0 \\ \\ \frac{k_{x1}}{\epsilon_1} A_1 e^{-k_{x1}\frac{h}{2}} - \frac{k_{x2}}{\epsilon_2} A_2 \sinh(-k_{x2}\frac{h}{2}) - \frac{k_{x2}}{\epsilon_2} A_3 \cosh(-k_{x12}\frac{h}{2}) = 0 \\ \\ A_2 \cosh(k_{x2}\frac{h}{2}) + A_3 \sinh(k_{x2}\frac{h}{2}) - A_4 e^{-k_{x3}\frac{h}{2}} = 0 \\ \\ \frac{k_{x2}}{\epsilon_2} A_2 \sinh(k_{x2}\frac{h}{2}) + \frac{k_{x2}}{\epsilon_2} A_3 \cosh(k_{x2}\frac{h}{2}) + \frac{k_{x3}}{\epsilon_3} A_4 e^{-k_{x3}\frac{h}{2}} = 0 \end{cases} \tag{2.26}$$

Setting the determinant of the above equations to zero brings us to the same dispersion

equation given by (2.23) [25]:

$$\tanh(k_{x2}h)(1 + s_1 s_3) + (s_1 + s_3) = 0 \tag{2.27}$$

but with the following definitions:

$$s_1 = \frac{\epsilon_2}{\epsilon_1}\frac{k_{x1}}{k_{x2}}\,,\; s_3 = \frac{\epsilon_2}{\epsilon_3}\frac{k_{x3}}{k_{x2}} \tag{2.28}$$

As a quick check, we notice that in the limiting case of lossless materials s_1 and s_3 are negative real numbers. Therefore, the first term of (2.27) is positive while the second term is negative suggesting that there may be solutions to (2.27). In fact, the equation can have one or two solutions depending on the structure parameters. Before considering the general case, we take a look at two special cases,

Case 1) Very thick film ($h \to \infty$)

In this case, the argument of the hyperbolic tangent function in (2.27) is very large and the function is replaced with unity. As a result, the equation reduces to

$$(1 + s_1)(1 + s_3) = 0$$

with the solution $s_1 = -1$ or $s_3 = -1$. Using (2.25) and (2.28) we obtain

$$\beta = k_0\left(\frac{\epsilon_1\epsilon_2}{\epsilon_1 + \epsilon_2}\right)^{\frac{1}{2}}$$

or

$$\beta = k_0\left(\frac{\epsilon_3\epsilon_2}{\epsilon_3 + \epsilon_2}\right)^{\frac{1}{2}}$$

which are the dispersion relations for a single metal-dielectric interface given in (2.16). This means that for a very thick metal film there are two independent SP modes one at each interface. Each mode fades exponentially into the film, therefore, for very thick films the two modes do not sense one another. When the film becomes thinner the two modes interact and give rise to two 'super modes' (see Fig. 2.2).

Case 2) Symmetric structure, ($\epsilon_1 = \epsilon_3$)

The dispersion equation (2.27) becomes

$$\tanh(k_{x2}h) = -\frac{2s_1}{1+s_1^2}$$

which after some algebraic manipulation changes to

$$\left(\tanh(\frac{k_{x2}h}{2}) + s_1\right)\left(s_1\tanh(\frac{k_{x2}h}{2}) + 1\right) = 0$$

giving two equations

$$\tanh\left(\frac{k_{x2}h}{2}\right) = -s_1 \tag{2.29}$$

$$\tanh\left(\frac{k_{x2}h}{2}\right) = -\frac{1}{s_1} \tag{2.30}$$

Equation (2.29) can also be obtained by setting $A_3 = 0$ in the equation set (2.26) meaning that (2.29) is the dispersion equation of a mode for which $A_3 = 0$. This mode has a symmetric profile about the yz plane which is a plane of symmetry for the structure of Fig. 2.3. Therefore, the mode is named the 'symmetric' mode. Similarly, (2.30) is the dispersion relation of the 'antisymmetric' mode for which $A_2 = 0$. Fig. 2.4 shows H_y component of the symmetric and antisymmetric modes.

Fig. 2.5 depicts real and imaginary parts of the propagation constants of symmetric

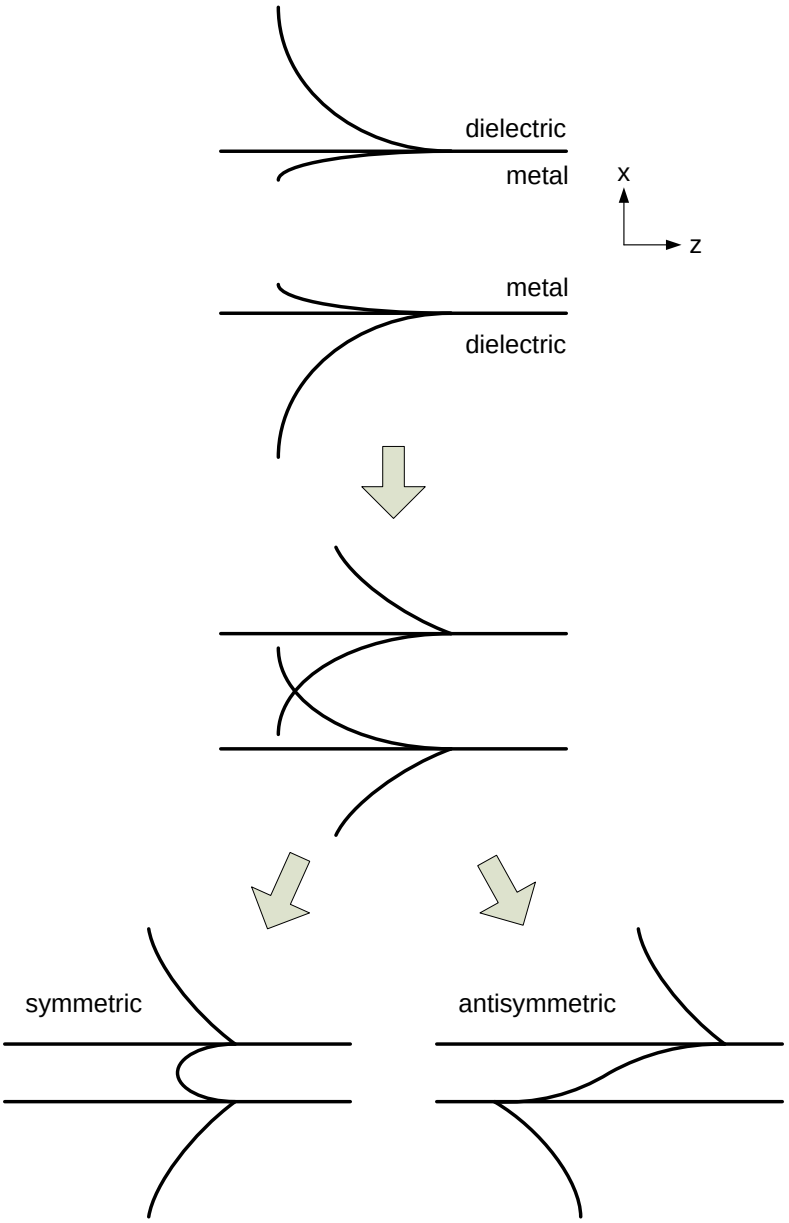

Figure 2.4: Coupling of SPP modes forming symmetric/asymmetric modes in thin-film SPWG (z is the propagation direction).

and antisymmetric modes as functions of the film thickness. Since the quantities plotted are the propagation constants normalized to the free space wavenumber, they are in fact the effective indices of guided modes. In the simulation we assumed, $\epsilon_1 = \epsilon_3 = 11.2$ and $\epsilon_2 = -116.38 - j11.1$ (dielectric constant of silver at λ=1550 nm). At small film thicknesses the real part of effective index of the symmetric mode is close to the refractive index of dielectric claddings. This can be understood from the mode profile of the symmetric mode in Fig. 2.2; as the film thickness approaches zero the symmetric mode becomes more and more like a plane wave propagating in the dielectric medium surrounding the film. Accordingly, the loss for the symmetric mode which is directly related to the imaginary part of the effective index approaches zero. For the antisymmetric mode, however, the real effective index increases unboundedly as film thickness reduces to zero. As a result, the mode becomes more and more confined inside the film because the real part of the propagation constant has a direct effect on the lateral decay of the exponential mode profile in claddings. In the limit when film thickness is zero the antisymmetric mode cannot be supported by the dielectric region as the H_y component should change sign abruptly. Therefore, the antisymmetric mode is squeezed inside the film. This explains why antisymmetric mode loss is larger than that of the symmetric mode. Due to the relative modal losses the symmetric and antisymmetric modes are named long-range and short-range surface plasmon modes (abbreviated as LRSP and SRSP), respectively.

When the film thickness increases, propagation constants of the modes get closer and in the limit of thick film they become degenerate, as explained before.

Fig. 2.6 shows the frequency dispersion of the LRSP and SRSP modes for a 20 nm thick film in dielectric materials of $\epsilon_1 = \epsilon_3 = 1$. For simplicity, a free electron gas

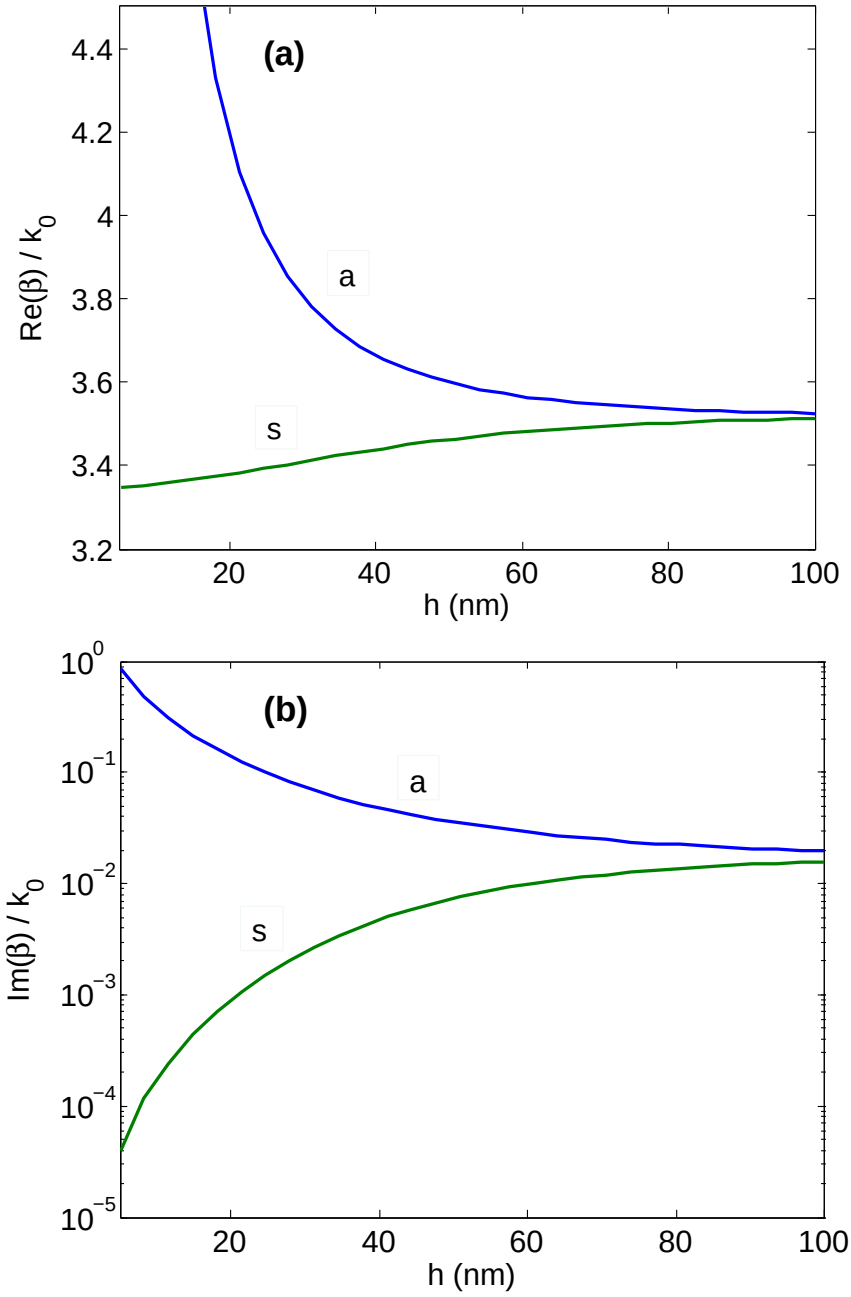

Figure 2.5: (a) Real and (b) imaginary parts of symmetric (denoted by s) and anti-symmetric (denoted by a) modes of thin-film SPWG versus metal film thickness.

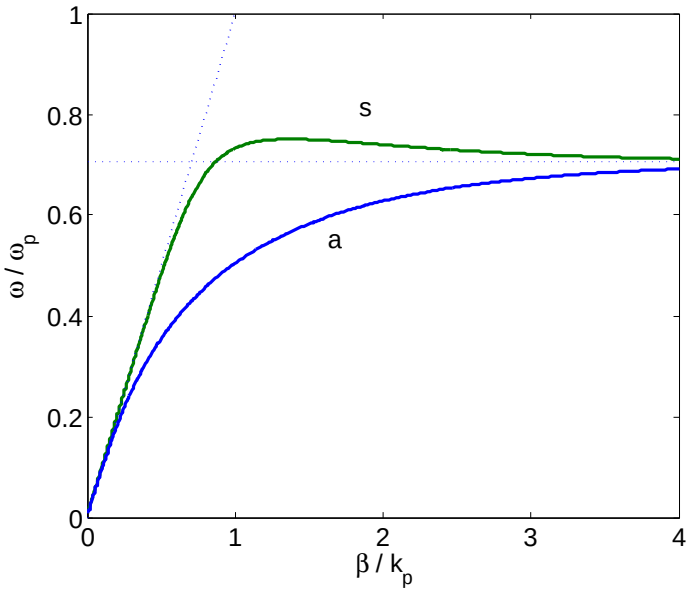

Figure 2.6: Thin-film SPWG dispersion curves.

(Drude) model is assumed for the dielectric constant of metal with a plasma frequency $\omega_p = 2\pi \times 2.18 \times 10^{15}$ rad/s. Frequencies are normalized to the plasma frequency and propagation constants to the free space wavenumber at the plasma frequency (k_p). The inclined asymptote is the light line, i.e., the dispersion curve in dielectric regions. Since both modes are to the right of the light line, they cannot propagate in the dielectric regions and are bound to the film. At large values of propagation constants the two modes become degenerate and approach a frequency called the 'surface plasmon frequency' as opposed to the bulk plasma frequency. This can be seen from the dispersion equations (2.29) and (2.30). When $\beta \to \infty$, $\tanh(\frac{k_{x2}h}{2}) \to 1$ and $s_1 \to \epsilon_2/\epsilon_1$ and both dispersion equations give $\omega_\infty = \frac{\omega_p}{\sqrt{1+\epsilon_1}}$ which is the surface plasmon frequency of single interface SPWG. This is because at very large propagation constants the guided wavelength is very small and the film looks very thick to the modes.

In the general case of $\epsilon_1 \neq \epsilon_3$ the two modes are not, strictly speaking, symmetric and antisymmetric anymore, but rather quasi symmetric and quasi antisymmetric. They are still called symmetric and asymmetric modes with no ambiguity. Fig. 2.7 shows the mode profiles for an asymmetric structure with $\epsilon_1 < \epsilon_3$.

The most important difference between symmetric and asymmetric thin film SPWGs is the existence of a cutoff film thickness for the symmetric mode in an asymmetric structure [25]. For metal films thinner than the cutoff value, the symmetric mode stops propagating. Equivalently, there is a cutoff wavelength above which the symmetric mode stops propagating. Fig. 2.8 shows the real and imaginary parts of the propagation constant of an asymmetric SPWG. The parameters of the SPWG are similar to those used for Fig. 2.5 except that $\epsilon_1 = 11$. At cutoff, assuming $\epsilon_1 < \epsilon_3$, the lateral wavenumber (k_x) in region 3 is zero which using (2.25) gives

$$\beta = k_0\sqrt{\epsilon_3}$$

that is, for lossless claddings the propagation constant at cutoff is real. This is confirmed by Fig. 2.8, as waveguide loss drops dramatically near cutoff. Other lateral wavenumbers are obtained as following

$$k_{x1} = k_0(\epsilon_3 - \epsilon_1)^{1/2}$$
$$k_{x2} = k_0(\epsilon_3 - \epsilon_2)^{1/2}$$

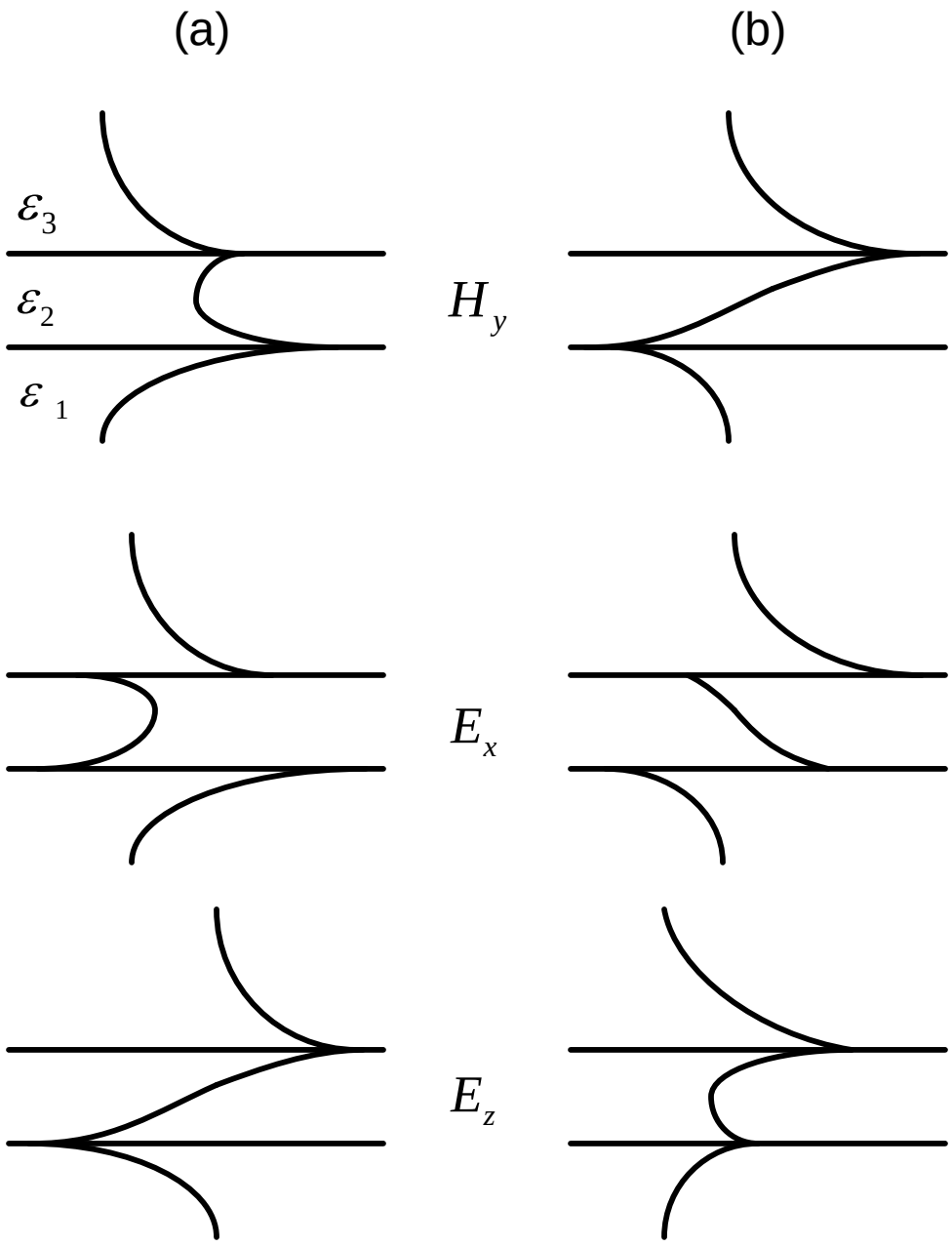

Figure 2.7: Mode profiles of asymmetric thin-film SPWG, (a) symmetric mode and (b) asymmetric mode.

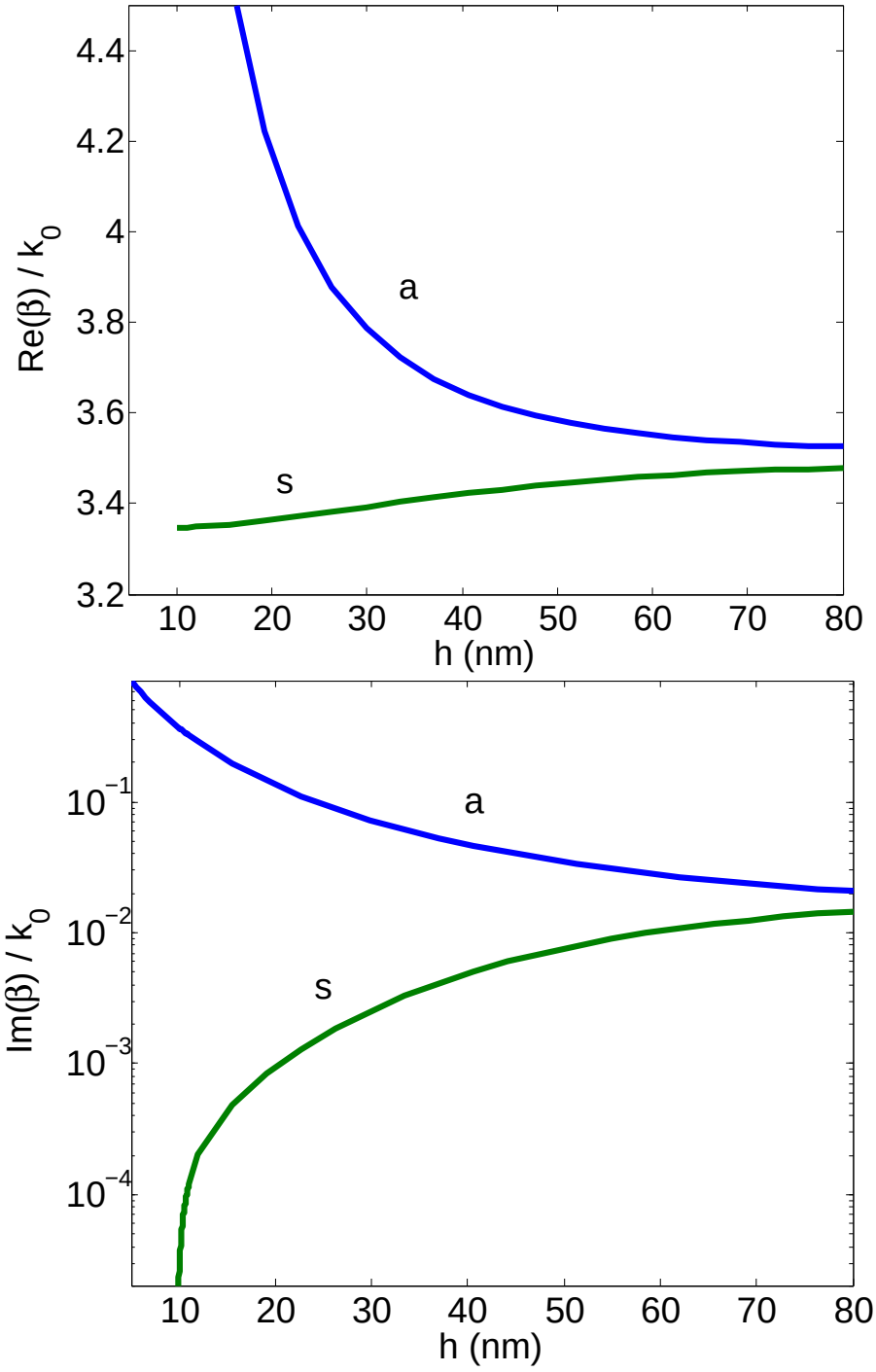

Figure 2.8: Propagation constant vs thickness for an asymmetric thin film structure.

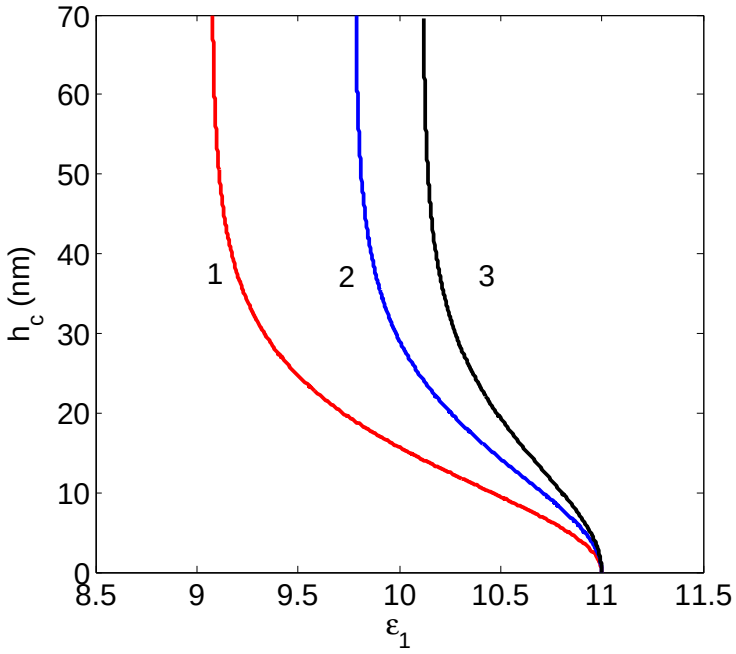

Figure 2.9: Cutoff thickness of an asymmetric thinfilm SPWG.

Using these relations in the dispersion equation (2.27) an analytical formula is obtained for the cutoff film thickness provided metal loss is neglected [25]

$$h_c = \frac{1}{2k_0(\epsilon_3-\epsilon_2)^{1/2}} \ln\left(\frac{\epsilon_1(\epsilon_3-\epsilon_2)^{1/2}-\epsilon_2(\epsilon_3-\epsilon_1)^{1/2}}{\epsilon_1(\epsilon_3-\epsilon_2)^{1/2}+\epsilon_2(\epsilon_3-\epsilon_1)^{1/2}}\right)$$

which is valid when

$$\frac{|\epsilon_2|}{\epsilon_1}\left(\frac{\epsilon_3-\epsilon_1}{\epsilon_3-\epsilon_2}\right)^{1/2} < 1$$

Symmetric modes of thin film SPWGs tolerate only a small amount of structural asymmetry, especially, at longer wavelengths. For an SPWG with $\epsilon_3 = 11$ and a Drude metal with plasma frequency of $\omega_p = 1.37 \times 10^{16}$, Fig. 2.9 shows the cutoff film thickness as a function of ϵ_1. Traces 1, 2 and 3 are corresponding to wavelengths 1 μm, 1.3 μm and 1.55 μm, respectively.

2.4 Metal-Insulator-Metal (MIM) SPWG

Following the previous analysis for the MIM structure one finds that similar to the IMI-SPWG there exists no TE, but two TM SP modes; one symmetric and one asymmetric. In addition to the surface modes there are ordinary TE/TM modes of the conventional type considered in the introductory waveguide theory (where the structure is usually called the parallel plates waveguide). Unlike surface modes, the ordinary modes do not decay away from metal interfaces into the dielectric region and metal claddings act merely as reflectors. The energy carried by them is concentrated in the dielectric region rather than metal surfaces and as a result the dielectric layer should be reasonably thick. Here, we are only concerned with the surface modes. For a symmetric structure with $\epsilon_1 = \epsilon_3 = -116.38 - j11.1$ and $\epsilon_2 = 11.2$ at $\lambda = 1.55\,\mu m$, Fig. 2.10 shows the geometric dispersion (propagation constant versus dielectric film thickness). Comparing Figs. (2.10) and (2.5), we notice a number of differences between MIM and IMI surface plasmon waveguides. First, there is a lower cutoff thickness for the asymmetric mode of MIM configuration even for a symmetric structure. Second, the symmetric mode loss is huge and increases as the dielectric layer thickness decreases. This makes the structure impractical for many applications. In the limit of very thick dielectric layer the propagation constants and losses of the two modes approach their corresponding values of a single-interface structure. Therefore, the propagation losses of both modes are always larger than the loss of a single-interface surface waveguide. With this disadvantage there is, however, an important benefit. Since the electromagnetic field decays much faster in metal than it does in dielectric, the spatial extent of the surface plasmon modes in the MIM configuration can be dramatically less compared to mode sizes in the IMI counterpart. This makes the

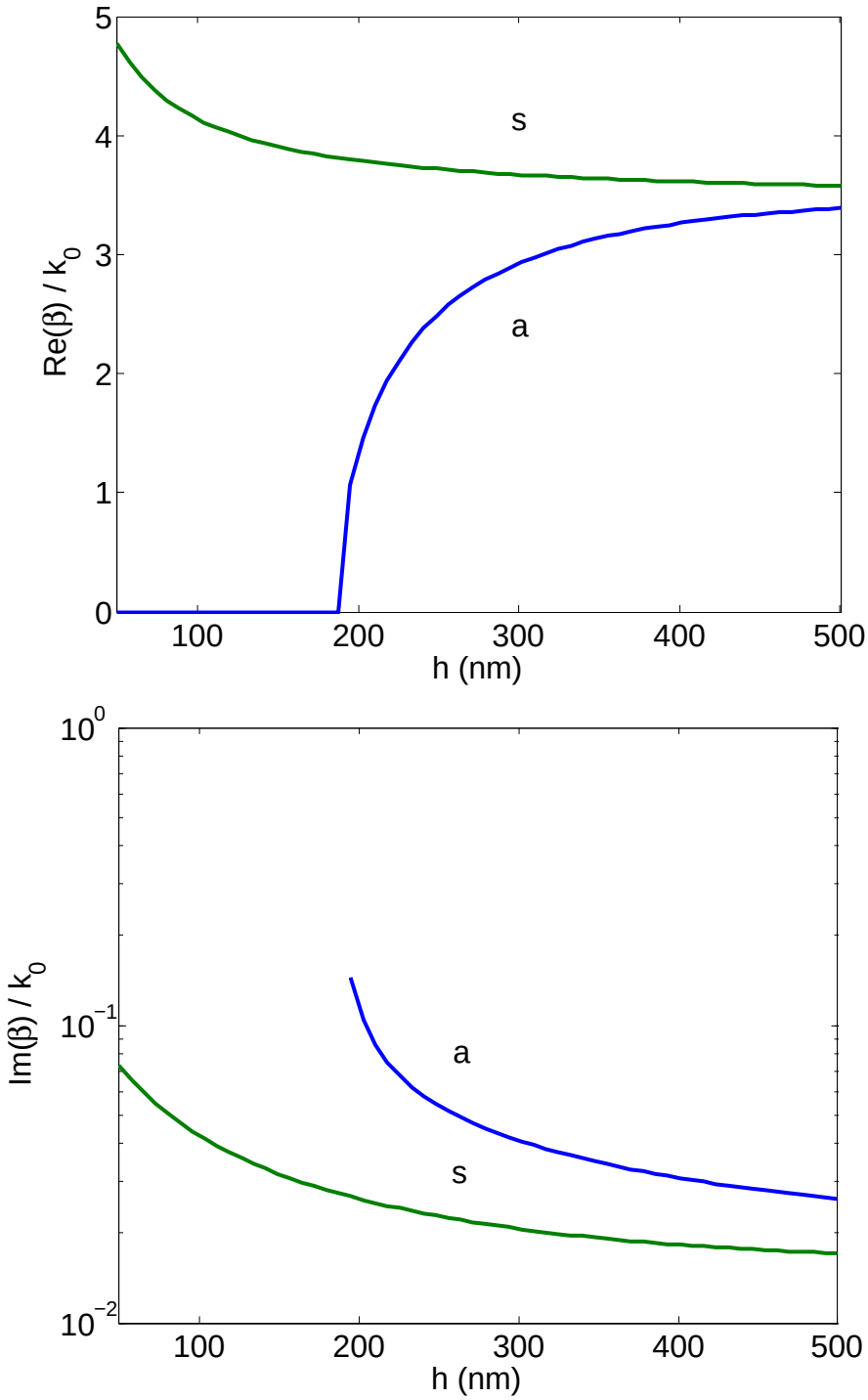

Figure 2.10: Real and imaginary parts of propagation constant of MIM structure modes.

MIM structure attractive for subwavelength and nanophotonic applications. But as a waveguide, its use is restricted to very short distances.

2.5 Other types of SPWG

Other than the three simple geometries considered in the previous sections numerous types of SPWGs with more complex geometries have been proposed, characterized and measured. Fig. 2.11 depicts schematically a number of them. The motive behind the development of these configurations is to achieve structures with low loss yet well confined LRSP modes. Such structures are key to realization of the future high density optical and optoelectronic integrated systems. Ease of in- and out- coupling of SPP modes to free space, optical fibres or other waveguides is another important design consideration.

Referring to Fig. 2.11 the first three SPWGs are usually called nanowires. The cylindrical shell nanowire (b) compared to the solid cylinder in (a) has the advantage of low loss when the radius is large [26, 27]. The waveguide has one LRSP mode and when the radius is large it becomes similar to the LRSP mode of an IMI strucure. The square cross section SPWG in (c) not only supports low loss LRSP modes, but also couples favourably to fibre and its planar feature makes its fabrication easier compared to (a) and (b). This waveguide is a limiting case of (g) with the metal width and thickness being equal. Therefore, the modes of (c) are the evolved versions of those of (g). Because of its symmetry the square cross section waveguide has two degenerate TE and TM modes polarized perpendicularly. Modal power loss as low as 0.14 dB/mm with a coupling loss of 3 dB to single mode fibre is expected computationally [28]. Waveguides in (d)-(f) are 1D geometries, all shown to support

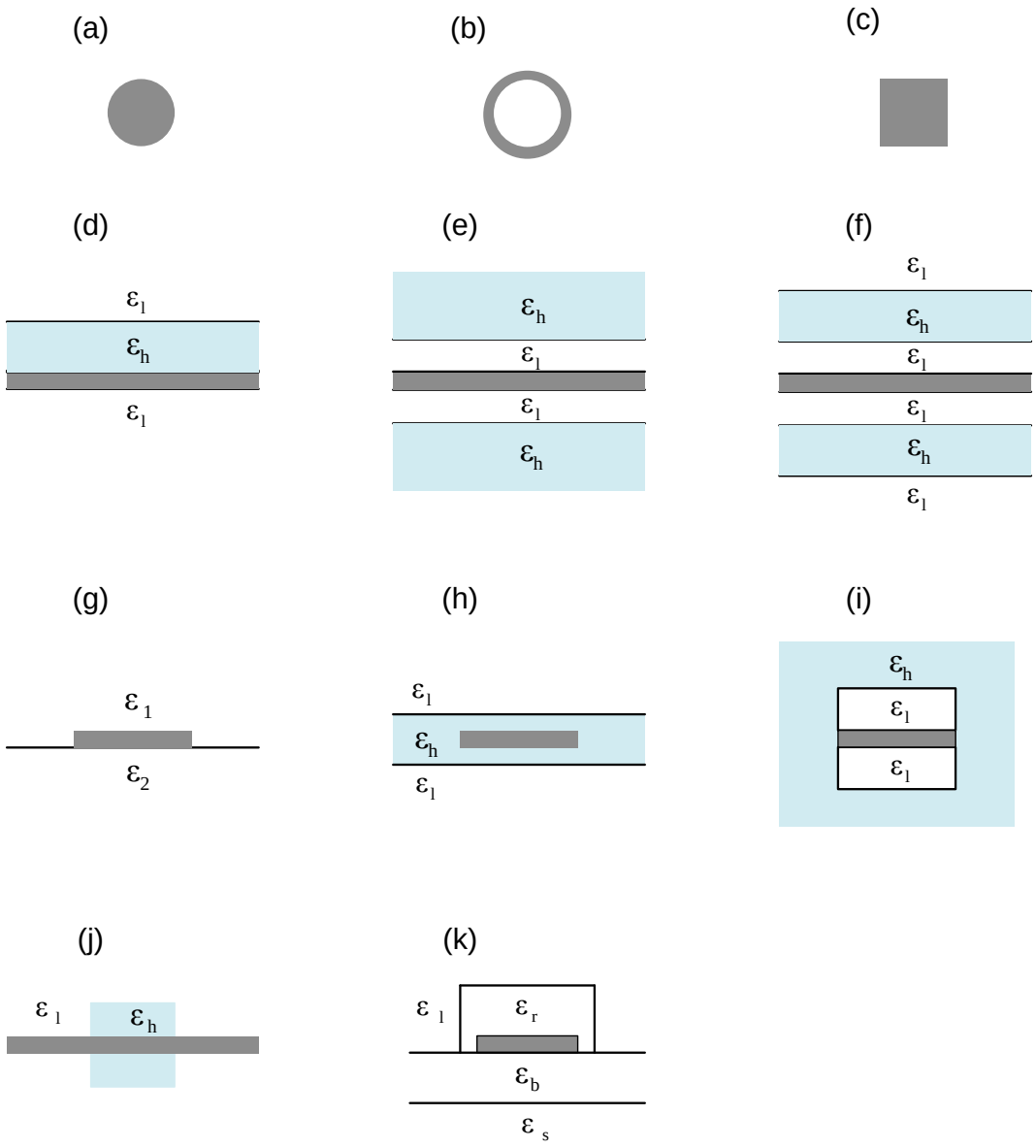

Figure 2.11: Several 1D and 2D SPWG geometries.

LRSP modes [29–35]. (d) and (f) contain high index dielectric slabs close to the metal slab. Individually, these dielectric slabs have their well-known conventional modes and therefore, when they get closer to the metal slab their conventional modes couple to SPP modes of metal slab to form hybrid modes. Since part of the field is guided outside the metal slab, their LRSP modal loss is lower than the loss of metal slab LRSP mode provided the structural parameters are selected properly.

The low index gaps adjacent to the metal slab in (e) and (f) push the LRSP of those structures toward cutoff. Near cutoff, the loss decreases dramatically. The structural parameters, therefore, should be selected in the way that the waveguide is operating near cutoff. The problem, however, is the sensitivity to layer thicknesses as a slight offset leaves the LRSP mode in cutoff. In (e), when the low index slabs are filled with a high index material and the high index claddings are replaced with a low index material, loss increases compared to the IMI system, but modal confinement improves, again indicating the loss-confinement tradeoff.

For confinement in both transverse directions structures (g)-(k) have been introduced. SPWG in (j) comprises a metal slab passing through a buried rectangular dielectric waveguide. The modes are similar to the modes of IMI waveguide, except they are laterally confined due to the higher index of the buried channel. If the slab is thin enough the waveguide supports an LRSP mode [36].

The thin metal stripe SPWG in Fig. 2.11(g) is the most extensively studied one among the two dimensional SPWGs. Reducing the width of a metal slab to a finite value makes the modal loss smaller, but also changes the mode spectrum, dramatically. Unlike its metal slab counterpart, the propagation characteristics of metal stripe SPWG cannot be calculated analytically and the computational effort involved

is considerably greater. The structure supports four fundamental bounded modes [37, 38] as opposed to only two bounded modes of the IMI structure. There can also exist higher order modes depending on the structural parameters. One of the fundamental modes referred to as ss_b^0 aquires a large propagation length provided the structure is symmetric ($\epsilon_1 = \epsilon_2$) and the film thickness is reasonably small. The mode is, accordingly, named LRSP mode. Similar to the metal slab structure there is a loss-confinement tradeoff as the film thickness varies. However, the loss in the finite width stripe can be orders of magnitude lower than the loss of metal slab waveguide. Another advantage is that its LRSP mode can be excited efficiently using end-fire coupling to dielectric waveguides including the optical fibre [39, 40]. Reference [41] demonstrated propagation of the LRSP in an SPWG comprising an 8 μm wide, 20 nm thick gold stripe embedded in SiO_2 at the communications wavelength of 1550 nm with a modal loss of 0.9 dB/mm. Modal losses of smaller than 0.1 dB/mm at the same wavelength has been predicted, theoretically.

The structure of Fig. 2.11(h) is obtained by embedding a metal stripe in a dielectric slab waveguide. The modes are hybrid SPP-dielectric modes. The structure is shown to alleviate the attenuation-confinement tradeoff compared to Fig. 2.11(g) [42]. The propagation length of a 6 μm wide and 10 nm thick gold stripe in BCB material was measured to be several millimeters at the 1550 nm wavelength [42].

The waveguide of Fig. 2.11(i) can be seen as the 2D generalization of waveguide (e) and is meant to add the lateral confinement to the benefits of the former [43, 44]. Reference [43] reports the simulation results of a structure with a gold stripe of 1 $\mu m \times$ 20 nm cross section, $\epsilon_l = (1.45)^2$, $\epsilon_h = (1.6)^2$ operating at $\lambda_0 = 850$ nm. Without the low index nanolayers the LRSP mode size was 1.76 μm and the $1/e$ propagation

length was 935 μm. With 25 nm thick nanolayers the mode swelled to a size of 7.18 μm while the propagation range reached 2.65 cm. Further increasing the nanolayers thickness pushes the mode toward cutoff. At a critical thickness the mode stops being bounded to the film and the mode size is infinitely large much the same way as the waveguide (e).

Finally, the asymmetric structure shown in (k) can be designed in such a way to support a tightly confined long range SPP mode. Reference [45] calculated at $\lambda_0 = 1.55\ \mu m$ a propagation length of over 3 mm with a mode size of 1.6 μm.

Chapter 3

Spontaneous Emission Coupling

3.1 Introduction

Active devices like LD and SLD use the stimulated emission phenomenon to generate optical gain. However, stimulated emission by itself is not enough to produce output photons. There have to be some photon seeds to trigger the multiplication process. These photon seeds are generated through the spontaneous emission process and are diverse in the propagation direction and spectrum. Only part of the spontaneous photons contribute to the device operation and the rest are wasted. The useful part, in devices with guided waves, is the spontaneous photons which can couple to the device waveguide. The significance of spontaneous photons depends on the device type and regime of operation. For example, in LD spontaneous photons have little effect on the output power once threshold is passed, but their effect on the output before threshold is considerable. SLD, on the other hand, is designed and operated in such a way to avoid lasing threshold. Therefore, the nature of SLD output is more like that of LD output before threshold and the spontaneous photons have an

important role in defining the power and spectrum of the output. The portion of the spontaneous photons coupled to the waveguide is accounted for by a parameter known as the spontaneous emission coupling factor. For LD the definition is restricted to the spontaneous photons that not only couple to the waveguide, but also have a wavelength close to the lasing mode wavelength.

A rough but simple and insightful calculation [46] gives us an idea of the magnitude of the spontaneous emission coupling factor. Consider an index guided typical LD (with a conventional dielectric waveguide) with a far field pattern which spreads 35° vertically and 25° horizontally at the FWHM intensity points as depicted in Fig. 3.1. The solid angle subtended by these angles is Ω_2 [46]

$$\begin{aligned}\Omega_2 &= 2\pi(1-\cos\theta_2)\\ &\simeq \pi\sin^2\theta_2\\ &\simeq 0.21\,(\text{sr})\end{aligned}$$

where, for simplicity, horizontal and vertical angles are replaced with an average value of $2\theta_2 = 30°$ and where the first approximation is reasonable for small angles which is valid for index guided structures with angles of only a few degrees. Inside the active region Ω_2 reduces to Ω_1 due to refraction. If the refractive index of the active region is taken to be $n_{eff} = 3.3$ and outside is air then

$$\Omega_1 = \Omega_2\left(\frac{\sin\theta_1}{\sin\theta_2}\right)^2 = \frac{\Omega_2}{n_{eff}^2}$$

Since the whole space is $4\pi\,(\text{sr})$, the portion of emission that is captured by the

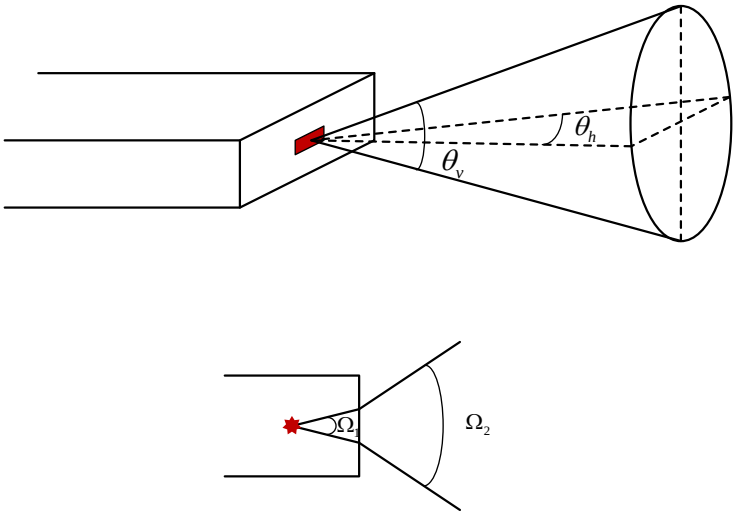

Figure 3.1: Schematic used to roughly calculate the spontaneous emission coupling factor in a dielectric waveguide.

waveguide is

$$\beta \simeq \frac{\Omega_1}{4\pi} \simeq 1.6 \times 10^{-3}$$

In practice, this value can reach up to about 0.01.

3.2 Spontaneous emission coupling to SPWG

In this section we describe a method of calculating the spontaneous emission coupling to SPWGs known as the CPS theory (after its pioneers, Chance, Prock, and Silbey) which was first developed to explain the experimental results of fluorescing molecules near metallic surfaces [47]. The electron-hole pair (exciton) which gives birth to a spontaneous photon is considered to be an electric dipole with a life time and decay rate $b(= 1/\tau)$ radiating near a planar structure with arbitrary layers of dielectric and/or metal. When isolated, the dipole decay rate is b_0, but when placed near an optical structure, the decay rate changes due to the interaction of dipole with its own

field reflected by the structure. The time development of the dipole moment, q, is determined from the differential equation[48, 49]

$$\ddot{q} + b_0\dot{q} + \omega_0^2 q = \frac{e^2}{m}E_R \tag{3.1}$$

in which the decay rate b_0 appears in the damping term and E_R which is the reflected electric field at the dipole position acts as a source. ω_0 is the oscillating frequency in the absence of the reflecting structure, e is the magnitude of the elementary charge and finally m is the effective dipole mass. Since E_R is the reflected version of the dipole field, its time dependence is similar to that of q and we can write [49]

$$q = q_0 e^{j\omega t} e^{-bt/2} \tag{3.2}$$

$$E_R = E_0 e^{j\omega t} e^{-bt/2} \tag{3.3}$$

where q_0 is real and E_0 is a complex number accounting for the amplitude and phase shift of the reflected field. ω is the shifted oscillation frequency. Substituting these relations into (3.1) gives

$$\Omega^2 - jb_0\Omega - \omega_0^2 = -\frac{e^2}{q_0 m}E_0 \tag{3.4}$$

where we defined $\Omega = \omega + jb/2$. This equation can be solved for Ω to get

$$\Omega = \frac{jb_0}{2} + \sqrt{\omega_0^2 - (\frac{b_0^2}{4} + \frac{e^2}{q_0 m} E_0)} \tag{3.5}$$

$$\simeq \frac{jb_0}{2} + \omega_0 \left[1 - \frac{1}{2\omega_0^2}(\frac{b_0^2}{4} + \frac{e^2}{q_0 m} E_0)\right]$$

In the first line of (3.5) the sign of the square root is chosen such that in the absence of damping and reflection $\Omega = \omega_0$. The approximation in the second line is made with the assumption that b_0^2 and the magnitude of $(e^2/q_0 m)E_0$ are very small compared with ω_0^2. Separating the real and imaginary parts of (3.5) brings us to the final relations for the decay rate and frequency of the dipole

$$b = b_0 + (\frac{e^2}{q_0 m \omega_0}) \operatorname{Im}(E_0) \tag{3.6}$$

$$\omega = \omega_0 - \frac{b^2}{8\omega_0} - (\frac{e^2}{2q_0 m \omega_0}) \operatorname{Re}(E_0) \tag{3.7}$$

If there is no damping other than radiation (or spontaneous emission) b_0 reduces to the classical formula for the damping coefficient of a dipole embedded in a space with refractive index $n_1 = \sqrt{\epsilon_1}$, i.e., [50]

$$b_r = \frac{e^2 \epsilon_1^{1/2} \omega_0^2}{6\pi\epsilon_0 m c^3} \tag{3.8}$$

but if there is an internal irradiative deexcitation then we introduce $\eta \equiv b_r/b_0$ with η being called the quantum yield of emitting state having a maximum value of unity.

Then from (3.6) and (3.8) one finds

$$\hat{b} \equiv \frac{b}{b_0} = 1 + \frac{6\pi\epsilon_0\eta c^3}{q_0\epsilon_1^{1/2}\omega_0^3}\,\mathrm{Im}(E_0)$$
$$= 1 + \frac{6\pi\epsilon_0\epsilon_1\eta}{q_0 k_1^3}\,\mathrm{Im}(E_0) \tag{3.9}$$

where $k_1 = n_1\omega/c$ is the wavenumber of the medium surrounding the dipole. The problem of finding the decay rate for any structure, therefore, comes down to solving for the electric field of a dipole near the structure. In the following subsections, the above problem is addressed for a single-interface SPWG and then is generalized to an arbitrary layered structure.

3.2.1 Single-interface SPWG

Fig. 3.2 shows the schematic of a dipole located in region 1 at a distance d above the surface of a half-space linear isotropic region 2. Region 1 is filled with a lossless material $\epsilon_1 > 1$, but there is no restriction on the dielectric function of region 2 other than those mentioned before. Two cases will be distinguished in which the dipole polarization is vertical or horizontal relative to the interface.

The simplest way of solving this problem is probably using the Hertz vector potentials. Since the magnetic field $\mathbf{H}$ is divergenceless, it can be assumed as the curl of a vector $\mathbf{\Pi}$ which is called the electric Hertz vector potential [51]

$$\mathbf{H} = j\omega\epsilon\nabla \times \mathbf{\Pi} \tag{3.10}$$

Using this relation in the Maxwell's equation

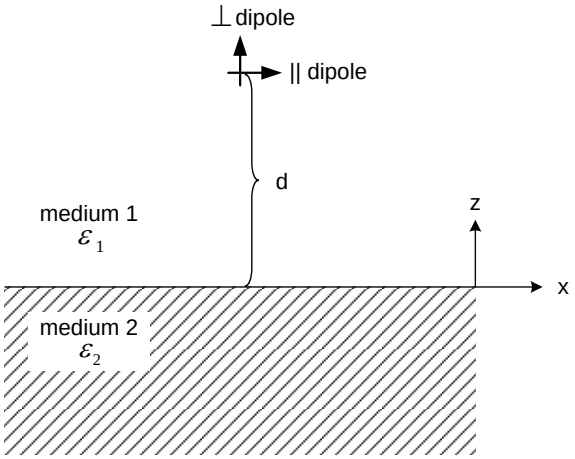

Figure 3.2: Dipole near a metal-delectric interface.

$$\nabla \times \mathbf{H} = \mathbf{J} + j\omega\epsilon\mathbf{E} \tag{3.11}$$

results in

$$\mathbf{E} = \nabla \times \nabla \times \mathbf{\Pi} - \frac{1}{j\omega\epsilon}\mathbf{J} \tag{3.12}$$

Another relation between the electric field and the Hertz potential can be obtained using Faraday's law

$$\nabla \times \mathbf{E} = -j\omega\mu\mathbf{H} \tag{3.13}$$

and (3.10)

$$\nabla \times \mathbf{E} = k^2 \nabla \times \mathbf{\Pi} \tag{3.14}$$

This allows us to write

$$\mathbf{E} = k^2\mathbf{\Pi} + \nabla\phi \tag{3.15}$$

where ϕ is an arbitrary scalar field. Equating (3.12) and (3.15) and remembering

from the vector analysis that

$$\nabla \times \nabla \times \mathbf{\Pi} = \nabla\nabla \cdot \mathbf{\Pi} - \nabla^2\mathbf{\Pi} \tag{3.16}$$

yields

$$\nabla\nabla \cdot \mathbf{\Pi} - \nabla^2\mathbf{\Pi} = \frac{1}{j\omega\epsilon}\mathbf{J} + k^2\mathbf{\Pi} + \nabla\phi \tag{3.17}$$

Vector potential $\mathbf{\Pi}$ has been defined by its curl. Therefore, according to the Hemholtz theorem its divergence can be defined at our discretion. To make things simpler we pick

$$\nabla \cdot \mathbf{\Pi} = \phi \tag{3.18}$$

and the final equation for the Hertz potential is

$$\nabla^2\mathbf{\Pi} + k^2\mathbf{\Pi} = -\frac{1}{j\omega\epsilon}\mathbf{J} \tag{3.19}$$

Therefore, the Hertz potential satisfies the inhomogeneous wave equation. Once the Hertz potential is found the electric field from (3.15) and (3.18) is given by

$$\mathbf{E} = k^2\mathbf{\Pi} + \nabla\nabla \cdot \mathbf{\Pi} \tag{3.20}$$

and the magnetic field is obtained from (3.10). Now, we consider a perpendicular dipole as in Fig. 3.2 and find its decay rate. According to (3.19)

$$\nabla^2\mathbf{\Pi} + k^2\mathbf{\Pi} = -\frac{1}{j\omega\epsilon_0\epsilon_1} Il\delta(\vec{r} - \vec{r'})\hat{z}$$

where $\vec{r}$ and $\vec{r'}$ are the position vectors of the observation point and dipole in spherical

coordinates, respectively. From Fig. 3.2, $\vec{r'} = d\hat{z}$. I is the dipole current and l is the dipole infinitesimal length. The product Il can be related to the dipole moment by $Il = j\omega q_0$. Because of the cylindrical symmetry of the problem we assume that the Hertz potential has only a z-component, i.e., $\mathbf{\Pi} = \Pi_z \hat{z}$ with Π_z satisfying

$$\nabla^2 \Pi_z + k^2 \Pi_z = -\frac{q_0}{\epsilon_0 \epsilon_1} \delta(\vec{r} - \vec{r'}) \tag{3.21}$$

In an infinite space in the absence of region 2 (3.21) has the well-known solution [52]

$$\Pi_{p1} = \frac{q_0}{4\pi\epsilon_0\epsilon_1} \frac{e^{-jk_1|\vec{r}-\vec{r'}|}}{|\vec{r}-\vec{r'}|} \tag{3.22}$$

in spherical coordinates. We call this solution the primary wave. It can be, in general, expanded in terms of the cylindrical harmonics according to the Fourier-Bessel transform as [52]

$$\Pi_{p1}(\rho, \phi, z) = \frac{q_0}{4\pi\epsilon_0\epsilon_1} \sum_{m=-\infty}^{\infty} e^{-jm(\phi-\phi')} \int_0^{\infty} J_m(k_\rho \rho) J_m(k_\rho \rho') e^{-jk_{1z}|z-z'|} \frac{k_\rho}{jk_{1z}} dk_\rho \tag{3.23}$$

with primed coordinates referring to the source and $k_\rho^2 + k_{1z}^2 = k_1^2$. In our case, however, $\rho' = 0$, $\phi' = 0$, $z' = 0$ and the solution is independent of ϕ. Therefore, only the term $m = 0$ is kept and (3.23) reduces to

$$\Pi_{p1}(\rho, z) = \frac{q_0}{4\pi\epsilon_0\epsilon_1} \int_0^{\infty} J_0(k_\rho \rho) e^{-jk_{1z}|z-d|} \frac{k_\rho}{jk_{1z}} dk_\rho \tag{3.24}$$

In the presence of region 2 fields will be modified; in region 1 the Hertz potential is written as

$$\Pi_{z1} = \Pi_{p1} + \Pi_{s1} \tag{3.25}$$

Π_{s1} is due to the secondary field which is the scattered field of the primary field by region 2 and satisfies the homogeneous wave equation

$$\nabla^2 \Pi_{s1} + k^2 \Pi_{s1} = 0$$

The solution is [52]

$$\Pi_{s1}(\rho, z) = \frac{q_0}{4\pi\epsilon_0\epsilon_1} \int_0^\infty R(k_\rho) J_0(k_\rho \rho) e^{-jk_{1z}(z+d)} \frac{k_\rho}{jk_{1z}} dk_\rho \tag{3.26}$$

In region 2 there is no primary field and the secondary field is given by

$$\Pi_{s2}(\rho, z) = \frac{q_0}{4\pi\epsilon_0\epsilon_1} \int_0^\infty T(k_\rho) J_0(k_\rho \rho) e^{j(k_{2z}z - k_{1z}d)} \frac{k_\rho}{jk_{1z}} dk_\rho \tag{3.27}$$

with $k_\rho^2 + k_{2z}^2 = k_2^2$. $R(k_\rho)$ and $T(k_\rho)$ are two unknown functions to be determined from the boundary conditions. The boundary conditions are the continuity of the tangential electric and magnetic fields which are only E_ρ and H_ϕ at the $z = 0$ plane. From (3.10) and (3.20)

$$E_\rho = \frac{\partial^2 \Pi_z}{\partial \rho \partial z}$$

$$H_\phi = -j\omega\epsilon \frac{\partial \Pi_z}{\partial \rho}$$

Therefore, the boundary conditions for the Hertz potentials are

$$\left.\frac{\partial^2 \Pi_{z1}}{\partial \rho \partial z}\right|_{z=0} = \left.\frac{\partial^2 \Pi_{z2}}{\partial \rho \partial z}\right|_{z=0}$$

$$\epsilon_1 \left.\frac{\partial \Pi_{z1}}{\partial \rho}\right|_{z=0} = \epsilon_2 \left.\frac{\partial \Pi_{z2}}{\partial \rho}\right|_{z=0}$$

These equations must hold for all values of ρ, therefore, they can be integrated to eliminate ρ. The integration constant is zero as the Hertz potentials vanish at infinity. As a result at $z = 0$

$$\frac{\partial \Pi_{z1}}{\partial z} = \frac{\partial \Pi_{z2}}{\partial z}$$

$$\epsilon_1 \Pi_{z1} = \epsilon_2 \Pi_{z2}$$

On solving, we find

$$R(k_\rho) = -R^{||}$$

$$T(k_\rho) = \frac{\epsilon_1}{\epsilon_2}(1 - R^{||})$$

where $R^{||}$ is the Fresnel reflection coefficient for an incident plane wave polarized parallel to the plane of incident (p-polarized or TM) given by [47]

$$R^{||} = \frac{\epsilon_1 k_{z2} - \epsilon_2 k_{z1}}{\epsilon_1 k_{z2} + \epsilon_2 k_{z1}} \tag{3.28}$$

In the case of a perfect conductor ($\epsilon_2 \to -\infty$), $R^{||} \to -1$, $R(k_\rho) \to 1$ and $T(k_\rho) \to 0$ as expected. The reflected field in region 1 from (3.26) is then due to an image charge at $z = -d$ and the field in region 2 vanishes. To find the reflected field at the dipole position, we substitute Π_{s1} into (3.20) and set $\rho = 0$ and $z = d$

$$E_0 = -\frac{q_0}{4\pi\epsilon_0\epsilon_1} \int_0^\infty R^{||} e^{-2jk_{1z}d} \frac{k_\rho^3}{jk_{1z}} dk_\rho \tag{3.29}$$

Since $k_{1z} = \pm\sqrt{k_1^2 - k_\rho^2}$, both k_{1z} and $-k_{1z}$ can be used in (3.29). We have to take the

negative sign in order for the integrand to remain finite when k_ρ increases. Therefore

$$E_0 = \frac{q_0}{4\pi\epsilon_0\epsilon_1}\int_0^\infty R^{||}e^{2jk_{1z}d}\frac{k_\rho^3}{jk_{1z}}dk_\rho$$

with $k_{1z} = \sqrt{k_1^2 - k_\rho^2}$. For numerical calculations we set $l_1 = -j\sqrt{1-u^2}$ where $u = k_\rho/k_1$ and come to the final relation for the reflected field

$$E_0 = -\frac{q_0 k_1^3}{4\pi\epsilon_0\epsilon_1}\int_0^\infty R^{||}e^{-2k_1 l_1 d}\frac{u^3}{l_1}du \tag{3.30}$$

Also, (3.28) can be rewritten as

$$R^{||} = \frac{\epsilon_1 l_2 - \epsilon_2 l_1}{\epsilon_1 l_2 + \epsilon_2 l_1} \tag{3.31}$$

where $l_2 = -j\sqrt{\epsilon_2/\epsilon_1 - u^2}$. Finally, substituting into (3.9), we find [47]

$$\hat{b}_\perp = 1 - \frac{3}{2}\eta\,\mathrm{Im}\left\{\int_0^\infty R^{||}e^{-2k_1 l_1 d}\frac{u^3}{l_1}du\right\} \tag{3.32}$$

The $\perp$ sign emphasizes that the obtained relation is for a perpendicular dipole.

Next, we consider the parallel polarized dipole which is oriented in the x direction. The procedure of finding the fields goes along the same lines as for a perpendicular dipole. Comparing to the previous discussion the primary field due to radiation in the space filled with ϵ_1 is

$$\Pi_{xp1} = \frac{q_0}{4\pi\epsilon_0\epsilon_1}\int_0^\infty J_0(k_\rho\rho)e^{-jk_{1z}|z-d|}\frac{k_\rho}{jk_{1z}}dk_\rho \tag{3.33}$$

and is in the x direction. The secondary fields due to reflection and refraction in the

presence of region 2 are as before

$$\Pi_{xs1} = \frac{q_0}{4\pi\epsilon_0\epsilon_1}\int_0^\infty R_x(k_\rho)J_0(k_\rho\rho)e^{-jk_{1z}(z+d)}\frac{k_\rho}{jk_{1z}}dk_\rho \tag{3.34}$$

$$\Pi_{xs2} = \frac{q_0}{4\pi\epsilon_0\epsilon_1}\int_0^\infty T_x(k_\rho)J_0(k_\rho\rho)e^{j(k_{2z}z-k_{1z}d)}\frac{k_\rho}{jk_{1z}}dk_\rho \tag{3.35}$$

However, in this case symmetry in ϕ is lost and Hertz potentials with only x components cannot satisfy the boundary conditions. Therefore, we add a z component to them [53]

$$\Pi_{zs1} = \frac{q_0}{4\pi\epsilon_0\epsilon_1}\cos\phi\int_0^\infty R_z(k_\rho)J_1(k_\rho\rho)e^{-jk_{1z}(z+d)}k_\rho^2 dk_\rho \tag{3.36}$$

$$\Pi_{zs2} = \frac{q_0}{4\pi\epsilon_0\epsilon_1}\cos\phi\int_0^\infty T_z(k_\rho)J_1(k_\rho\rho)e^{j(k_{2z}z-k_{1z}d)}k_\rho^2 dk_\rho \tag{3.37}$$

so that

$$\mathbf{\Pi}_1 = (\Pi_{xp1} + \Pi_{xs1})\hat{x} + \Pi_{zs1}\hat{z}$$

$$\mathbf{\Pi}_2 = \Pi_{xs2}\hat{x} + \Pi_{zs2}\hat{z}$$

Functions R_x, R_z, T_x and T_z are to be found from the boundary conditions, which are the continuity of tangential electric and magnetic fields E_x ,E_y ,H_x and H_y at the $z = 0$ plane, as given below, respectively:

$$\epsilon_1\Pi_{x1} = \epsilon_2\Pi_{x2}$$

$$\frac{\partial\Pi_{x1}}{\partial x} + \frac{\partial\Pi_{z1}}{\partial z} = \frac{\partial\Pi_{x2}}{\partial x} + \frac{\partial\Pi_{z2}}{\partial z}$$

$$\epsilon_1\Pi_{z1} = \epsilon_2\Pi_{z2}$$

$$\epsilon_1 \frac{\partial \Pi_{x1}}{\partial z} = \epsilon_2 \frac{\partial \Pi_{x2}}{\partial z}$$

Imposing these conditions on (3.33) to (3.37) gives the unknown functions

$$\begin{aligned} R_x(k_\rho) = R^\perp &= \frac{k_{1z} - k_{2z}}{k_{1z} + k_{2z}} \\ &= \frac{l_1 - l_2}{l_1 + l_2} \end{aligned}$$

$$\begin{aligned} T_x(k_\rho) &= \frac{\epsilon_1}{\epsilon_2}(1 + R^\perp) \\ &= \frac{2\epsilon_1}{\epsilon_2} \frac{k_{1z}}{k_{1z} + k_{2z}} \end{aligned}$$

$$R_z(k_\rho) = \frac{2(\epsilon_2 - \epsilon_1)}{(k_{1z} + k_{2z})(\epsilon_2 k_{1z} + \epsilon_1 k_{2z})}$$

$$T_z(k_\rho) = \frac{\epsilon_1}{\epsilon_2} R_z$$

Note that R_x is the same as $R^\perp$ which is the Fresnel reflection coefficient for an incident plane wave with TE polarization (or s-polarized) relative to the incident plane. With the Hertz potentials being at hand from (3.20) the electric field at the dipole position is found to be

$$E_0 = \frac{q_0 k_1^3}{8\pi\epsilon_0\epsilon_1} \operatorname{Im}\left\{ \int_0^\infty \left[(1-u^2) R^{||} + R^\perp \right] e^{-2jk_1 l_1 d} \frac{u}{l_1} du \right\}$$

Inserting in (3.9) gives us the final relation for the decay rate [47]

$$\hat{b}_{||} = 1 + \frac{3\eta}{4} \operatorname{Im}\left\{ \int_0^\infty \left[(1-u^2) R^{||} + R^\perp \right] e^{-2jk_1 l_1 d} \frac{u}{l_1} du \right\}$$

3.2.2 Spectrum of power dissipation

Considering the power radiated by a dipole in different directions with the presence of a planar structure enables us to find the channels into which power dissipates. For a dipole in a medium with dielectric constant ϵ_1 radiated power is given by the well-known Larmor dipole formula [54]

$$P_0 = \frac{q_0^2 \omega^4 \epsilon_1^{1/2}}{12\pi\epsilon_0 c^3}$$

and the time averaged power radiated by the dipole in the structure of Fig. 3.2 is found by integration of the Poynting's vector over the whole space [50]

$$P_\perp = -\frac{q_0^2 k_1^3 \omega}{8\pi\epsilon_0\epsilon_1} \operatorname{Im}\left\{\int_0^\infty \left[1 + R^{||} e^{-2k_1 l_1 d}\right] \frac{u^3}{l_1} du\right\} \tag{3.38}$$

for the perpendicular dipole and

$$P_{||} = -\frac{q_0^2 k_1^3 \omega}{16\pi\epsilon_0\epsilon_1} \operatorname{Im}\left\{\int_0^\infty \left[2 - u^2 + \left((1-u^2)R^{||} + R^\perp\right) e^{-2k_1 l_1 d}\right] \frac{u}{l_1} du\right\} \tag{3.39}$$

for the parallel dipole. The parameters used in these formulas were defined before. By selectively integrating the Poynting's vector over horizontal planes located above and below the dipole a breakdown of the radiated power is obtained [55]. One part of the radiated power (obtained by integration over a plane above the dipole) is in the form of propagating electromagnetic waves including the wave reflected by the interface of region 2. The other part (obtained by integration over a plane below the dipole) is the electromagnetic wave that transfers energy into region 2. In the terminology of the antenna theory, the first part is called 'radiative' and the second part 'nonradiative'

waves indicating that the electromagnetic wave which carries energy to region 2 cannot propagate in region 1. These power components for the perpendicular and parallel dipoles are

$$P_{\perp,r} = -\frac{q_0^2 k_1^3 \omega}{8\pi\epsilon_0\epsilon_1} \operatorname{Im}\left\{\int_0^1 \left[1 + R^{||} e^{-2k_1 l_1 d}\right] \frac{u^3}{l_1} du\right\}$$

$$P_{\perp,nr} = -\frac{q_0^2 k_1^3 \omega}{8\pi\epsilon_0\epsilon_1} \operatorname{Im}\left\{\int_1^\infty \left[1 + R^{||} e^{-2k_1 l_1 d}\right] \frac{u^3}{l_1} du\right\}$$

$$P_{||,r} = -\frac{q_0^2 k_1^3 \omega}{16\pi\epsilon_0\epsilon_1} \operatorname{Im}\left\{\int_0^1 \left[2 - u^2 + \left((1-u^2)R^{||} + R^{\perp}\right) e^{-2k_1 l_1 d}\right] \frac{u}{l_1} du\right\}$$

$$P_{||,nr} = -\frac{q_0^2 k_1^3 \omega}{16\pi\epsilon_0\epsilon_1} \operatorname{Im}\left\{\int_1^\infty \left[2 - u^2 + \left((1-u^2)R^{||} + R^{\perp}\right) e^{-2k_1 l_1 d}\right] \frac{u}{l_1} du\right\}$$

In the above integrals u represents the normalized parallel component of the wave vector ($u = k_\rho/k_1$). Any wave with $u > 1$ cannot propagate in region 1. Therefore, the integrals show that power transferred to region 2 comes from the near field wave components of the dipoles. Each power component is associated with a decay rate. For the two dipole polarizations, decay rates are [55]

$$\hat{b}_{\perp,r} = \eta - \frac{3}{2}\eta \operatorname{Im}\left\{\int_0^1 R^{||} e^{-2k_1 l_1 d} \frac{u^3}{l_1} du\right\} \tag{3.40}$$

$$\hat{b}_{\perp,nr} = (1-\eta) - \frac{3}{2}\eta \operatorname{Im}\left\{\int_1^\infty R^{||} e^{-2k_1 l_1 d} \frac{u^3}{l_1} du\right\} \tag{3.41}$$

$$\hat{b}_{||,r} = \eta + \frac{3\eta}{4} \operatorname{Im}\left\{\int_0^1 \left[(1-u^2)R^{||} + R^{\perp}\right] e^{-2jk_1 l_1 d} \frac{u}{l_1} du\right\} \tag{3.42}$$

$$\hat{b}_{||,nr} = (1-\eta) + \frac{3\eta}{4} \operatorname{Im}\left\{\int_1^\infty \left[(1-u^2)R^{||} + R^{\perp}\right] e^{-2jk_1 l_1 d} \frac{u}{l_1} du\right\} \tag{3.43}$$

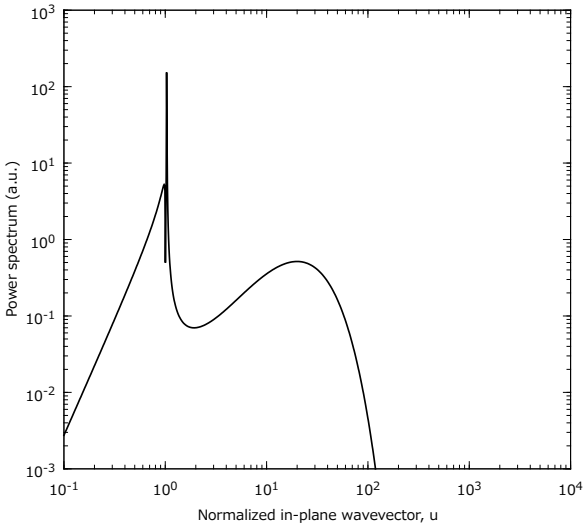

Figure 3.3: 'p-space power spectrum' for a perpendicular dipole near a metal-dielectric interface.

In (3.40)-(3.43) internal deexcitation represented by the parameter η is incorporated into the nonradiative decay rates. Note that

$$\hat{b}_{pol} = \hat{b}_{pol,r} + \hat{b}_{pol,nr}$$

where *pol* is either $\perp$ or $||$. The distribution of dipole power into different channels can be depicted by plotting the integrand of (3.38) and (3.39) versus the integrating dummy variable. Fig. 3.3 shows an example where region 1 is air and region 2 is silver with the dielectric constant $\epsilon_2 = -16 + j0.7$. The wavelength is 633 nm. As mentioned before, the horizontal axis shows the parallel component of the wave vector normalized with k_1. Integration of the $u < 1$ part of curve gives 'radiative' power which propagates away from the dipole in region 1. We call it P_{photon}. Right above $u = 1$ there is a sharp peak which is in fact located at $u = \left(\frac{\epsilon_2}{\epsilon_1 + \epsilon_2}\right)^{1/2}$.

From (2.16) it is understood that this value belongs to the surface plasmon mode bound to the interface. The peak contributes P_{SP} to the whole power radiated by the dipole. There is another peak in the 'nonradiative' range of wave vectors with a corresponding power which does not belong to the surface plasmon mode, but carries energy into the metallic region. It is sometimes called 'lossy surface waves' [50, 56]. As a result the total power is written as

$$P = P_{photon} + P_{SP} + P_{LSW}$$

Correspondingly, the decay rates due to each channel are related as

$$\hat{b} = \hat{b}_{photon} + \hat{b}_{SP} + \hat{b}_{LSW}$$

Fig. 3.4 shows the above three decay rates for perpendicular and parallel polarizations as functions of the dipole-metal distance. For the same parameters, Fig. 3.5 shows the probability of dipole decay into different channels. As seen in the figure, at very small distances all the dipole energy is dissipated inside metal in the form of lossy surface waves. As the distance grows this decay rate quickly diminishes and makes room for the surface plasmon coupling. Since coupling to surface plasmons is still a nonradiative effect, as indicated above, it is expected to eventually decrease as the dipole distance further increases. At very far distances, all the dipole energy goes into radiating photons and metal acts as a simple (lossy) mirror. Curves in Fig. 3.5 related to the surface plasmons show the portion of dipole energy coupled to the surface plasmon mode of the metal-dielectric interface which by definition is the spontaneous emission coupling factor β, the quantity that we are interested in.

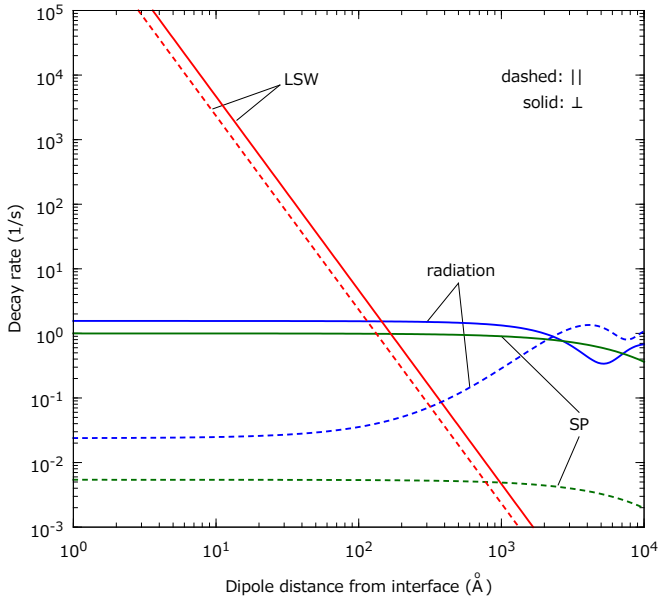

Figure 3.4: Partial decay rates for single interface SPWG, $\lambda = 1300$nm, $\epsilon_1 = 1, \epsilon_2 = -91.7 - j5.8$.

Therefore,

$$\beta \equiv \frac{\hat{b}_{SP}}{\hat{b}}$$

From Fig. 3.5 the coupling factor for the perpendicular dipole reaches to a maximum of about 65% at a dipole distance of 500 nm.

3.2.3 Multiple Interfaces

The structure in Fig. 3.2 can be generalized to one in which a multilayer planar structure is placed below the dipole. This section deals with such a structure (see Fig. 3.6). Different layers of the structure are arbitrary in thickness (d_i's) and dielectric function (ϵ_i's). Therefore, lossy metallic films are included, as well. As before, to find different deexcitation channels and their corresponding decay rates Maxwell's equations need

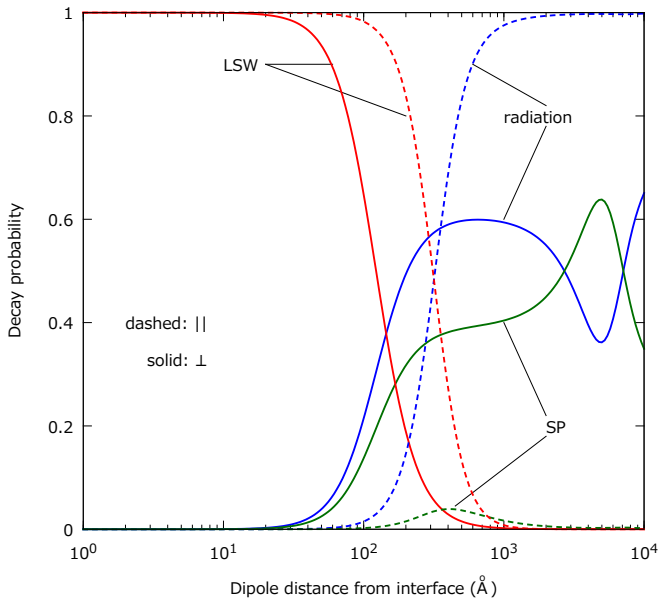

Figure 3.5: Decay probabilities for a metal-dielectric interface, $\lambda = 1300\,\text{nm}, \epsilon_1 = 1, \epsilon_2 = -91.7 - j5.8$.

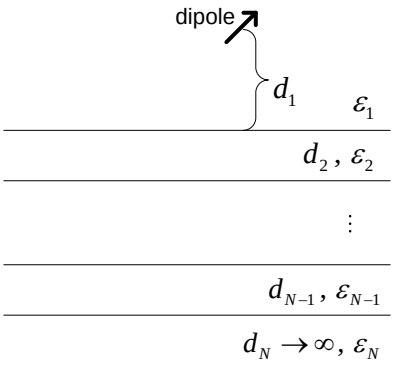

Figure 3.6: Dipole near a multilayer structure.

to be solved subject to the new boundary conditions imposed by the new structure. A straight forward but rather tedious way, is using the dyadic Green's function method [57]. Here, we present the resulting formulas correcting several typos found in [55]

$$\hat{b}_{\perp,r} = \eta + \frac{3}{2}\eta \,\mathrm{Im}\left\{\int_0^1 f e^{-2k_1 l_1 d_1}\frac{u^3}{l_1}du\right\} \tag{3.44}$$

$$\hat{b}_{\perp,nr} = (1-\eta) + \frac{3}{2}\eta \,\mathrm{Im}\left\{\int_1^\infty f e^{-2k_1 l_1 d_1}\frac{u^3}{l_1}du\right\} \tag{3.45}$$

$$\hat{b}_{||,r} = \eta + \frac{3\eta}{4} \,\mathrm{Im}\left\{\int_0^1 \left[(u^2-1)f + c\right] e^{-2jk_1 l_1 d_1}\frac{u}{l_1}du\right\} \tag{3.46}$$

$$\hat{b}_{||,nr} = (1-\eta) + \frac{3\eta}{4} \,\mathrm{Im}\left\{\int_1^\infty \left[(u^2-1)f + c\right] e^{-2jk_1 l_1 d_1}\frac{u}{l_1}du\right\} \tag{3.47}$$

The new parameters c and f are to be defined [58]

$$f = -\frac{R_{12}^{||} + \mathbb{S}_2}{1 + R_{12}^{||}\mathbb{S}_2}$$

where $\mathbb{S}_2$ is found by the recursive formula

$$\mathbb{S}_n = \frac{R_{n,n+1}^{||} + \mathbb{S}_{n+1}}{1 + R_{n,n+1}^{||}\mathbb{S}_{n+1}} e^{-2l_n k_1 d_n}, n = N-1, ..., 2$$

with $\mathbb{S}_N = 0$. Also,

$$c = \frac{R_{12}^{\perp} + \mathbb{R}_2}{1 + R_{12}^{\perp}\mathbb{R}_2}$$

where $\mathbb{R}_2$ is given by the recursive formula

$$\mathbb{R}_n = \frac{R_{n,n+1}^{\perp} + \mathbb{R}_{n+1}}{1 + R_{n,n+1}^{\perp}\mathbb{R}_{n+1}} e^{-2l_n k_1 d_n}, n = N-1, ..., 2$$

with $\mathbb{R}_N = 0$. In the above equations $R^{\perp}_{n,n+1}$ and $R^{||}_{n,n+1}$ are the perpendicular and parallel Fresnel reflection coefficients, respectively,

$$R^{\perp}_{n,n+1} = \frac{l_n - l_{n+1}}{l_n + l_{n+1}}$$

$$R^{||}_{n,n+1} = \frac{\epsilon_n l_{n+1} - \epsilon_{n+1} l_n}{\epsilon_n l_{n+1} + \epsilon_{n+1} l_n}$$

where $l_n = -j\sqrt{\epsilon_n/\epsilon_1 - u^2}$, as before. For the special case of a thin film below a dipole the above equations reduce to the following relations [47]

$$\hat{b}_{\perp,r} = \eta - \frac{3}{2}\eta \,\mathrm{Im}\left\{\int_0^1 (\frac{R^{||}_{12} + R^{||}_{23}e^{-2k_1 l_2 d_2}}{1 + R^{||}_{12}R^{||}_{23}e^{-2k_1 l_2 d_2}})e^{-2k_1 l_1 d_1}\frac{u^3}{l_1}du\right\} \tag{3.48}$$

$$\hat{b}_{\perp,nr} = (1-\eta) - \frac{3}{2}\eta \,\mathrm{Im}\left\{\int_1^\infty (\frac{R^{||}_{12} + R^{||}_{23}e^{-2k_1 l_2 d_2}}{1 + R^{||}_{12}R^{||}_{23}e^{-2k_1 l_2 d_2}})e^{-2k_1 l_1 d_1}\frac{u^3}{l_1}du\right\} \tag{3.49}$$

$$\begin{aligned}\hat{b}_{||,r} = \eta + \frac{3\eta}{4}\,\mathrm{Im}\Bigg\{\int_0^1 \Bigg[&(\frac{R^{||}_{12} + R^{||}_{23}e^{-2k_1 l_2 d_2}}{1 + R^{||}_{12}R^{||}_{23}e^{-2k_1 l_2 d_2}})(1-u^2) \\ &+ \frac{R^{\perp}_{12} + R^{\perp}_{23}e^{-2k_1 l_2 d_2}}{1 + R^{\perp}_{12}R^{\perp}_{23}e^{-2k_1 l_2 d_2}}\Bigg] e^{-2jk_1 l_1 d_1}\frac{u}{l_1}du\Bigg\}\end{aligned} \tag{3.50}$$

$$\begin{aligned}\hat{b}_{||,nr} = (1-\eta) + \frac{3\eta}{4}\,\mathrm{Im}\Bigg\{\int_1^\infty \Bigg[&(\frac{R^{||}_{12} + R^{||}_{23}e^{-2k_1 l_2 d_2}}{1 + R^{||}_{12}R^{||}_{23}e^{-2k_1 l_2 d_2}})(1-u^2) \\ &+ \frac{R^{\perp}_{12} + R^{\perp}_{23}e^{-2k_1 l_2 d_2}}{1 + R^{\perp}_{12}R^{\perp}_{23}e^{-2k_1 l_2 d_2}}\Bigg] e^{-2jk_1 l_1 d_1}\frac{u}{l_1}du\Bigg\}\end{aligned} \tag{3.51}$$

Using the driven formulation we next consider a thin-film SPWG or IMI structure. Fig 3.7 shows a typical p-space power spectrum. $u > 1$ region is shown because the integrand used is valid for that region only. The film thickness used is 5 nm and the

dielectric function of metal and claddings are $-116.38 - j11.1$ and 11.2, respectively. Wavelength is 1.55 μm and dipole-film distance is set to 90 nm. Here, two peaks are recognized. The first one is very sharp and is located at $u = 1.1$. It belongs to the symmetric mode or LRSP. The wide peak at $u = 2.96$ corresponds to the SRSP. Fig. 3.8 shows the coupling of a perpendicular dipole to the SP modes and radiation as a function of dipole-film distance. Coupling to LRSP is maximum when dipole-film distance is about 120 nm. At smaller distances SRSP and at larger distances radiation dominate. Maximum coupling to LRSP is 17%. For a parallel polarized dipole the situation is quite different. As seen from Fig. 3.9 coupling to LRSP is dramatically lower than that for the perpendicular dipole. If the dipole-film distance is set to 120 nm where coupling of perpendicular dipole to LRSP was maximum in the above example and now metal film thickness is sweeped Fig. 3.10 is obtained. As the film thickness increases LRSP and SRSP merge together to form a degenerate mode. Beyond 20 nm film thickness the loss is so high that the film is useless for an active device.

The formulation presented in this chapter is used in chapter 6 to analyze the spontaneous emission coupling to different modes of a five layer SPWG.

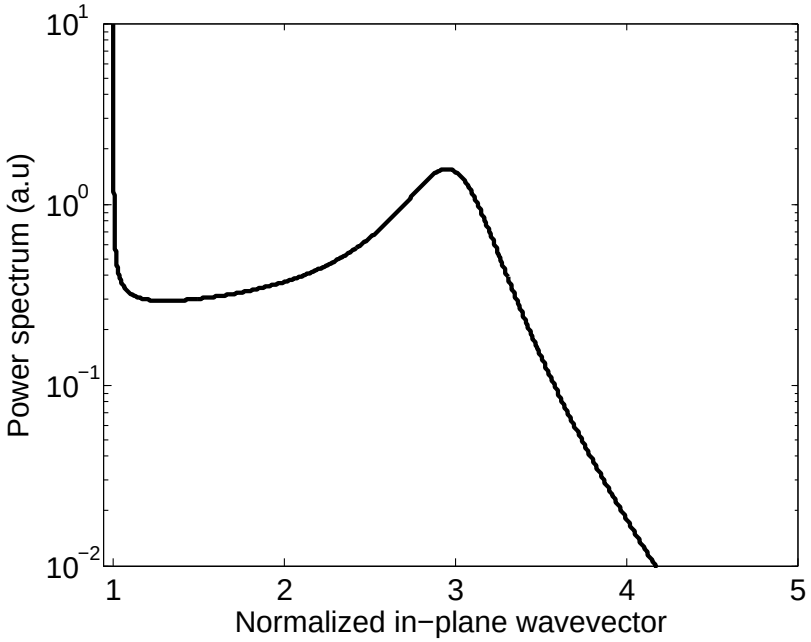

Figure 3.7: Nonradiative portion of power spectrum for a typical thin-film SPWG showing peaks due to symmetric (sharp peak at the left) and asymmetric (wide peak at the right) modes.

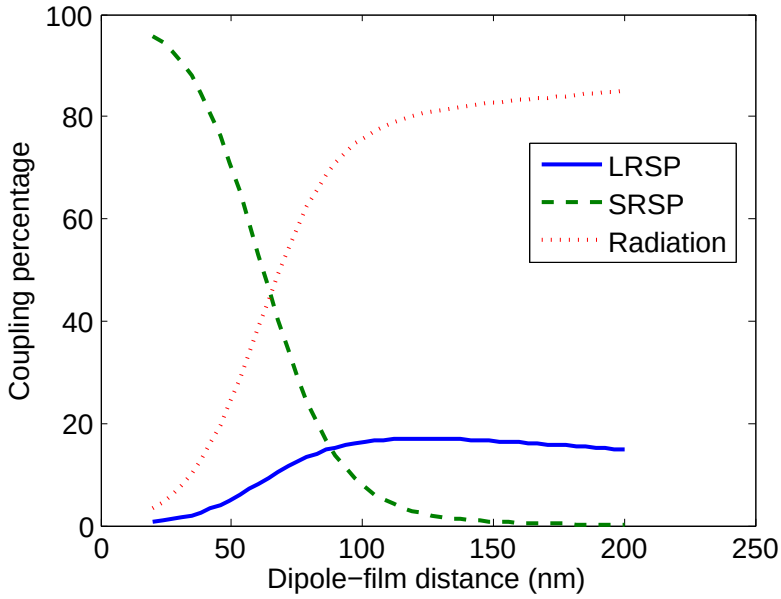

Figure 3.8: Perpendicular dipole coupling to thin-film SPWG modes and radiation.

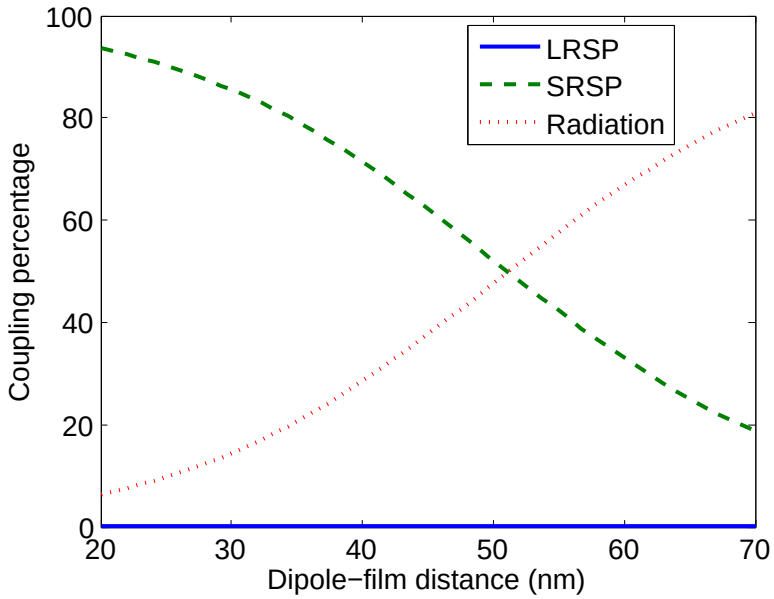

Figure 3.9: Parallel dipole coupling to thin-film SPWG modes and radiation.

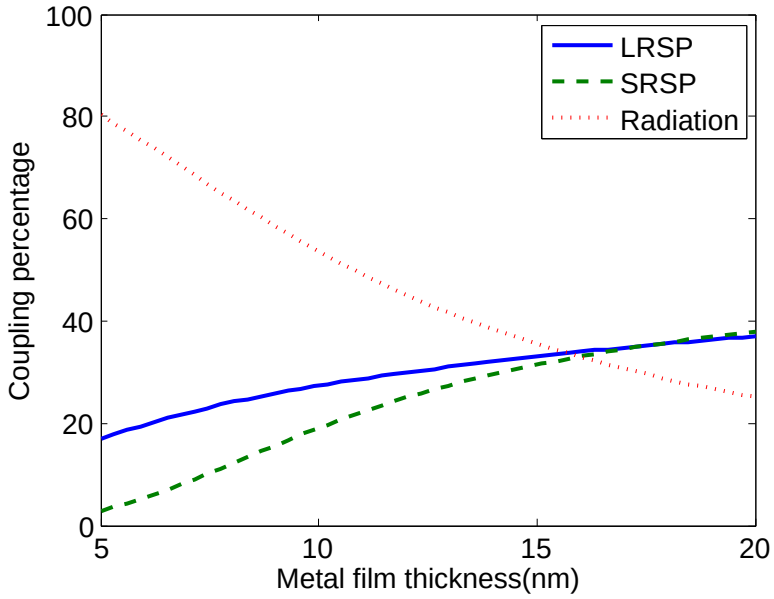

Figure 3.10: Perpendicular dipole coupling to SPP modes and radiation as a function of metal film thickness.

Chapter 4

Facet Reflectivity

4.1 Introduction

Superluminescent diodes are structurally and functionally very similar to the traveling wave type of semiconductor optical amplifiers (SOA's). SOA's have two important types of Fabry-Perot (FP) and traveling wave (TW) structures. The former, like FP laser diodes, has cavity resonances and this is achieved by reflection from facets. The latter, on the other hand, avoids optical facet reflections. In an ideal SLD and TW-SOA there is no residual reflection from facets (or sometimes, in the case of an ideal SLD, no residual reflection from one facet). Residual reflection from facets forms an optical cavity inside the device and causes ripples on the spectral response of the output power. These ripples are due to the periodic variation of device gain. At wavelengths corresponding to the longitudinal modes of the formed cavity the optical gain is slightly higher than the gain between those wavelengths. Ripples (also known as spectral modulation) become larger with increasing the device gain, i.e. with increasing the injection current or the active region length. The spectral modulation

is defined as [59]

$$M = \frac{P_{\max} - P_{\min}}{P_{\max} + P_{\min}}$$

where P_{max} and P_{min} are the values of the peak and valley powers defined by ripple oscillations, respectively. Most applications of broadband sources require a flat or low modulation spectral response and therefore, output ripples are undesirable.

For a plane wave propagating in a medium with refractive index n_a coming across a planar interface with air reflection can in theory be totally eliminated using a coating layer with refractive index $n = \sqrt{n_a}$ and thickness $\lambda/4n$ where λ is the wavelength in vacuum. However, optical modes guided by device waveguides are not plane waves and therefore, the above simplistic approach is not enough to overcome the facet reflection problem. For very low spectral modulation facet reflectivities must be 0.01% or smaller. Achieving such low reflectivities is not trivial and much effort has been devoted to research and development in this area. Most well-known techniques of reducing optical reflection from facets include utilizing antireflection (AR) coating, tilted, bent or tapered waveguides, buried facets and integrated absorption regions. Usually, a combination of these methods is used to achieve very low reflectivities. In SOA devices low reflectivity is also the key to attain low polarization sensitivity.

In the following sections the above methods are briefly discussed with more emphasis on the AR coatings design.

4.2 Tilted waveguide

One way of reducing facet reflections is to tilt the device waveguide relative to the facets such that the propagating waves are not perpendicular to the facets [60]. This

prevents the reflected waves at the tilted facet from coupling back to the waveguide. The effect of tilted waveguides depends on the structure geometry and changes with the tilt angle. The reduction in reflectivity is also different for different waveguide modes.

Although tilting the waveguide has a remarkable influence on the effective facet reflectivity it is not usually sufficient to reduce the reflectivity below 10^{-4} as demanded by some applications and therefore, it is used along with other techniques mentioned above. In addition, the effect of tilt on higher order modes (if there are any) is opposite as compared with the fundamental mode [61], i.e., for higher order modes the reflectivity increases. This may cause some problems (especially in the case of SOA's where single mode operation is desired).

4.3 Buried facet (Window facet)

Here, the idea comes from the fact that reflection at facet is caused by the sharp discontinuity in refractive indices on the two sides of the facet. Therefore, reflection can be reduced by reducing the index contrast at the facet [62, 63]. In the buried facet structure the waveguide end does not face air but, rather faces a region (window region) with no waveguiding and with similar refractive index to the waveguide region. At its other end, the window region interfaces air by a cleaved facet. The window-air interface is usually coated to minimize reflectivity. The guided mode in the active region enters the window region with little reflection. Upon entering, the guided mode is approximated by a Gaussian beam diverges due to diffraction as it propagates towards the facet. After reflecting from the facet it keeps diverging. By the time it reaches the beginning of the window region this flattened field can hardly couple to

the waveguide. The effective reflectivity is approximately given by [64]

$$R_{eff} = \frac{R_0}{1 + \left(\frac{2L_w}{k_w w^2}\right)^2}$$

where R_0 is the facet reflectivity at the end of the window region, L_w and k_w are the length and wavenumber of the window region, respectively and w is the spot size at the facet. The advantage of this technique is that TE and TM modes are treated the same way. If implemented along with antireflection layers, the reflectivity may be less than 10^{-4}.

4.4 Absorbing regions

The idea of dissipating the wave power in order to prevent it from reflecting has long been in use in microwaves. In SLD this is done by preventing current from being injected into an end section of device thus eliminating gain and making the region resistive for example by implanting certain ions and particles [65]. This technique is useful for SLD, but cannot be applied to SOA.

Implementation of combinations of different techniques is reported to have been successfully tested [59, 66, 67] with reflectivities below 10^{-5}.

4.5 Antireflection coating (ARC)

Using antireflection (AR) layers in reducing residual reflections is the most common of all the previous methods. In fact, the previous methods are usually used along with AR coating techniques to kill effectively residual reflections. The simplest case is

coating the facet with a single layer of a suitably chosen dielectric material. Therefore, this case is considered first after reviewing some background material. In the following subsections the method of design and analysis of single- and double-layer ARC is essentially taken from reference [68]. Apart from minor discrepencies in the notation, our treatment is different from that given in the above reference in that, our problem is matching light in a high refractive index incident medium to air, rather than from air to a high index medium.

4.5.1 Plane wave reflection from a single interface

Consider an interface between two dielectric media as depicted by Fig. 4.1. An incident plane wave in region 1 illuminates the interface giving rise to a reflected and a transmitted plane wave in regions 1 and 2, respectively. The incident and reflected wave vectors make identical angles with the line normal to the interface [69]. The electric and magnetic fields of all three plane waves follow the notation

$$\mathcal{E} = \hat{E} \exp(j\omega\, t - j\vec{k} \cdot \vec{r})\, \hat{e} + \text{c.c.}$$

$$\mathcal{H} = \hat{H} \exp(j\omega\, t - j\vec{k} \cdot \vec{r})\, \hat{h} + \text{c.c.}$$

where $\vec{k}$ is the wave vector and $\vec{r}$ is the position vector. $\hat{e}$ and $\hat{h}$ are unit vectors. In the case of TM waves, Fig. 4.1(a), continuity of the tangential electric field across the interface requires

$$\hat{E}_i \cos\theta_1 + \hat{E}_r \cos\theta_1 = \hat{E}_t \cos\theta_2 \tag{4.1}$$

Since,

$$\mathcal{H} = y\,(\hat{k} \times \mathcal{E}) \tag{4.2}$$

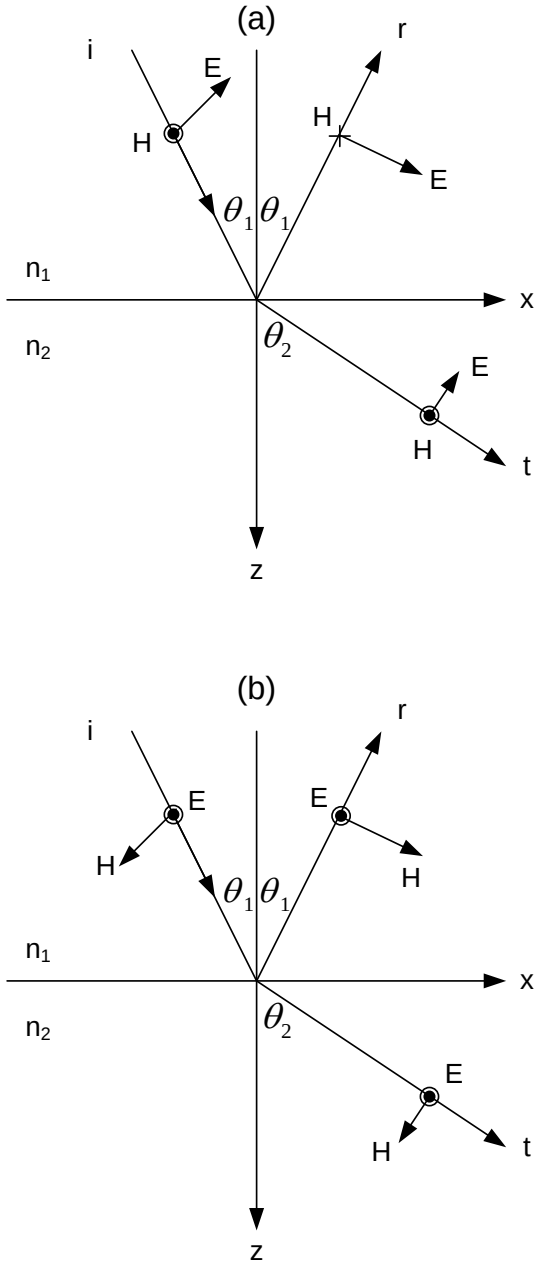

Figure 4.1: Schematic of plane wave reflection and transmission at a dielectric interface, (a) TM or p-polarization (b) TE or s-polarization.

where $\hat{k}$ is the unit vector in the wane propagation direction and y is the wave impedance in each medium defined by

$$\begin{aligned} y &= \sqrt{\frac{\epsilon}{\mu_0}} \\ &= n\sqrt{\frac{\epsilon_0}{\mu_0}} \\ &= n\, y_0 \simeq 2.6544 \times 10^{-3} n \text{ (S)} \end{aligned}$$

Continuity of the magnetic field requires

$$y_1 \hat{E}_i - y_1 \hat{E}_r = y_2 \hat{E}_t \tag{4.3}$$

Now, let us denote the tangential electric fields by $E_i = \hat{E}_i \cos\theta_1$, $E_r = \hat{E}_r \cos\theta_1$ and $E_t = \hat{E}_t \cos\theta_2$. For TM waves, then, the tangential magnetic fields are $H_i = \hat{H}_i$, $H_r = \hat{H}_r$ and $H_t = \hat{H}_t$. From (4.2) and the definitions just made we get

$$H_i = \frac{y_1}{\cos\theta_1} E_i$$

$$H_r = \frac{y_1}{\cos\theta_1} E_r$$

$$H_t = \frac{y_2}{\cos\theta_2} E_t$$

With this notation the boundary conditions (4.1) and (4.3) are rewritten

$$E_i + E_r = E_t$$

$$\frac{y_1}{\cos\theta_1}E_i - \frac{y_1}{\cos\theta_1}E_r = \frac{y_2}{\cos\theta_2}E_t$$

Solving these equations for E_r and E_t, we find the famous Fresnel amplitude reflection and transmission coefficients

$$\begin{aligned} r_{TM} &\equiv \frac{E_r}{E_i} \\ &= \frac{\frac{y_1}{\cos\theta_1} - \frac{y_2}{\cos\theta_2}}{\frac{y_1}{\cos\theta_1} + \frac{y_2}{\cos\theta_2}} \end{aligned}$$

$$\begin{aligned} t_{TM} &\equiv \frac{E_t}{E_i} \\ &= \frac{\frac{2y_1}{\cos\theta_1}}{\frac{y_1}{\cos\theta_1} + \frac{y_2}{\cos\theta_2}} \end{aligned}$$

The reflectivity and transmissivity are defined

$$R_{TM} \equiv |r_{TM}|^2 = \left|\frac{E_r}{E_i}\right|^2$$

$$T_{TM} \equiv |t_{TM}|^2 = \left|\frac{E_t}{E_i}\right|^2$$

Lastly, by defining $\eta_i = \dfrac{n_i}{\cos\theta_i}$ $(i = 1, 2)$, we come to

$$r_{TM} = \frac{\eta_1 - \eta_2}{\eta_1 + \eta_2} \tag{4.4}$$

$$t_{TM} = \frac{2\eta_1}{\eta_1 + \eta_2} \tag{4.5}$$

These relations in the case of normal incidence reduce to the familiar equations

$$r_{TM} = \frac{n_1 - n_2}{n_1 + n_2}$$

$$t_{TM} = \frac{2n_1}{n_1 + n_2}$$

Following a similar approach for TE polarization, Fig. 4.1(b), we obtain similar results

$$r_{TE} = \frac{\eta_1 - \eta_2}{\eta_1 + \eta_2} \tag{4.6}$$

$$t_{TE} = \frac{2\eta_1}{\eta_1 + \eta_2} \tag{4.7}$$

In this case, however, $\eta = n\cos\theta$ should be defined.

If Y_2 denotes the ratio of the total tangential magnetic and electric fields at the interface, then, from above it is noted that [68]

$$Y_2 = \frac{H}{E} = y_0\eta_2 \tag{4.8}$$

and from (4.4), (4.5), (4.6) and (4.7) it results for both polarizations

$$r = \frac{Y_1 - Y_2}{Y_1 + Y_2} \tag{4.9}$$

$$t = \frac{2Y_1}{Y_1 + Y_2} \tag{4.10}$$

where Y_1 is defined in a similar manner to Y_2

$$Y_1 = y_0\eta_1$$

Equations (4.9) and (4.10) can be used in the case of several dielectric layers stacked below region 1 and the problem is just to find Y_2.

4.5.2 Reflection from a thin film

The structure is illustrated in Fig. 4.2. Here, in the film region there are multiple reflections due to the existence of two interfaces. In the following, waves that propagate in the $+z$ direction (positive-going waves) are denoted with the + superscript and those propagating in the z direction (negative-going waves) with the - superscript. As in the previous subsection, the tangential electric and magnetic fields in each region, E and H, are used. At boundary b tangential electric and magnetic fields are written as the sum of positive-going and negative-going waves

$$E_b = E_{2b}^{+} + E_{2b}^{-}$$

$$H_b = y_0\eta_2 E_{2b}^{+} - y_0\eta_2 E_{2b}^{-}$$

In these relations subscript $2b$ denotes medium 2 (with refractive index n_2) at boundary b. Solving for the positive/negative-going components,

$$E_{2b}^{+} = \frac{1}{2}(\frac{H_b}{y_0\eta_2} + E_b)$$

$$E_{2b}^{-} = \frac{1}{2}(-\frac{H_b}{y_0\eta_2} + E_b)$$

$$H_{2b}^{+} = y_0\eta_2 E_{2b}^{+} = \frac{1}{2}(H_b + y_0\eta_2 E_b)$$

$$H_{2b}^{-} = -y_0\eta_2 E_{2b}^{-} = \frac{1}{2}(H_b - y_0\eta_2 E_b)$$

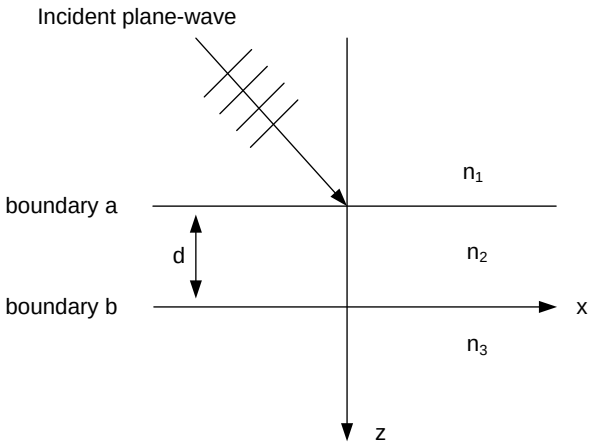

Figure 4.2: Plane wave incident on the first boundary of thin film coating.

The fields at the other interface, boundary a, at the same instant and the same x and y coordinates can be obtained from those at boundary b by incorporating a factor for taking the phase difference of shifting $z = 0$ to $z = -d$ into account. This factor for the positive-going waves is $\exp(j\delta)$ and for the negative-going waves is $\exp(-j\delta)$ where [68]

$$\delta = k_0 n_2 d \cos\theta_2 = (\frac{2\pi}{\lambda_0})\, n_2 d \cos\theta_2 \tag{4.11}$$

The values of E and H at boundary a are now

$$E_{2a}^{+} = E_{2b}^{+}\, e^{j\delta} = \frac{1}{2}(\frac{H_b}{y_0\eta_2} + E_b)\, e^{j\delta}$$

$$E_{2a}^{-} = E_{2b}^{-}\, e^{-j\delta} = \frac{1}{2}(-\frac{H_b}{y_0\eta_2} + E_b)\, e^{-j\delta}$$

$$H_{2a}^{+} = H_{2b}^{+}\, e^{j\delta} = \frac{1}{2}(H_b + y_0\eta_2 E_b)\, e^{j\delta}$$

$$H_{2a}^{-} = H_{2b}^{-}\, e^{-j\delta} = \frac{1}{2}(H_b - y_0\eta_2 E_b)\, e^{-j\delta}$$

Solving the above equations gives us

$$E_a = E_{2a}^{+} + E_{2a}^{-}$$

$$= E_b \cos\delta + H_b \frac{j \sin\delta}{y_0 \eta_2}$$

$$H_a = H_{2a}^{+} + H_{2a}^{-}$$

$$= E_b \, j y_0 \eta_2 \sin\delta + H_b \cos\delta$$

Put in the matrix form

$$\begin{bmatrix} E_a \\ H_a \end{bmatrix} = \begin{bmatrix} \cos\delta & \dfrac{j \sin\delta}{y_0 \eta_2} \\ j y_0 \eta_2 \sin\delta & \cos\delta \end{bmatrix} \begin{bmatrix} E_b \\ H_b \end{bmatrix} \tag{4.12}$$

Since the tangential electric and magnetic fields are continuous across boundaries and in region 3 below boundary b, there are only positive-going waves (4.12) connects the tangential field components at the incident interface with those of the transmitted through the final medium. The 2×2 matrix in (4.12) is known as the characteristic matrix of the thin film [68]. Now, similar to (4.8) define

$$Y = \frac{H_a}{E_a} = y_0 \eta_e$$

which is the optical admittance of the thin film structure as seen from medium 1 at boundary a. η_e is the effective η parameter defined for the space below boundary a.

Substituting into (4.12) we obtain

$$E_a \begin{bmatrix} 1 \\ Y \end{bmatrix} = \begin{bmatrix} \cos\delta & \dfrac{j\sin\delta}{y_0\eta_2} \\ jy_0\eta_2\sin\delta & \cos\delta \end{bmatrix} \begin{bmatrix} 1 \\ y_0\eta_3 \end{bmatrix} E_b \tag{4.13}$$

in which

$$\frac{H_b}{E_b} = y_0\eta_3$$

has been used. From (4.13),

$$Y = y_0 \frac{\eta_3\cos\delta + j\eta_2\sin\delta}{\cos\delta + j(\eta_3/\eta_2)\sin\delta}$$

and

$$\eta_e = \frac{\eta_3\cos\delta + j\eta_2\sin\delta}{\cos\delta + j(\eta_3/\eta_2)\sin\delta}$$

To find the reflection coefficient of the incident wave in medium 1 we write similar to the case of a single interface

$$r_{TE,TM} = \frac{\eta_1 - \eta_e}{\eta_1 + \eta_e}$$

Again, the proper expression should be used in the TE ($\eta = n\cos\theta$) and TM ($\eta = n/\cos\theta$) cases. To find η_e, it is deduced from (4.13),

$$\begin{bmatrix} B \\ C \end{bmatrix} = \begin{bmatrix} \cos\delta & \dfrac{j\sin\delta}{\eta_2} \\ j\eta_2\sin\delta & \cos\delta \end{bmatrix} \begin{bmatrix} 1 \\ \eta_3 \end{bmatrix} \tag{4.14}$$

where

$$\eta_e = \frac{C}{B} \tag{4.15}$$

The advantage of the matrix approach is that it is extendable to the case of several thin film layers. We just need to sandwich the characteristic matrices of the layers between the left and the right vectors in (4.14) starting with the first layer

$$\begin{bmatrix} B \\ C \end{bmatrix} = M_1 M_2 ... M_{m-1} \begin{bmatrix} 1 \\ \eta_m \end{bmatrix} \tag{4.16}$$

where M_i is the characteristic matrix corresponding to the i-th layer and η_m is the η parameter for the last semi-infinite medium. η_e will be obtained from (4.15).

4.5.3 Single-layer AR coating

As is well-known the reflectivity of a thin film structure can be totally eliminated provided that

$$\eta_2 = (\eta_1 \eta_3)^{1/2} \tag{4.17}$$

$$\delta = 2m\pi + \pi/4 \tag{4.18}$$

where m is an integer. In this case $\eta_e = \eta_1$ and $R = |r|^2 = 0$. This condition can be met only at a single wavelength which depends on the polarization and the incidence angle. Fig. 4.3 shows the reflectivity of a thin film between air and a dielectric with $n_3 = 3.5$ for a number of situations. The latter medium is the incidence medium. The thin layer is designed to cancel reflectivity at $\lambda = 1\,\mu m$ for the normal incidence. It is apparent from the figure that as the incidence angle increases the value reflectivity quickly goes far beyond what is needed for a practical SLD. Considering that a waveguide mode is not a plane wave but rather consists of plane waves with a range of angles it is concluded that a single AR layer has a limited capability as facet

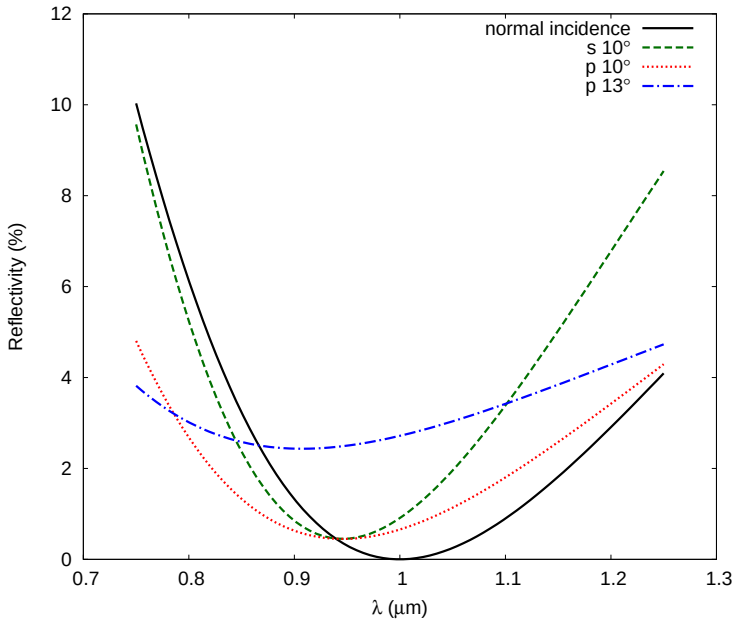

Figure 4.3: Reflectivity of a single-layer ARC for a number of plane waves with different polarizations and incident angles (p:TM, s:TE).

AR coating. Even for a plane wave with normal incidence there is only one wavelength for zero reflectivity and the range of wavelengths about this central wavelength over which reflectivity is low is narrow, usually in the order of a few tens of nanometers. In Fig. 4.3 the range of wavelengths for $R \leq 0.01\%$ is less than 20 nm and for $R \leq 0.1\%$ is 60 nm. Another problem with the single AR coating is that its refractive index is strictly defined by (4.17). This value, can in some cases, be difficult, or even impossible to realize; the structure has just too few adjustable parameters. All the above mentioned limitations can greatly be relaxed if two or more layers are used.

4.5.4 Double-layer AR coating

The structure considered in this case is a stack of two planar thin layers between two semi infinite media. Totally, therefore, there are four media of refractive indices

n_1, n_2, n_3 and n_4, respectively. n_1 is the incidence medium. Following the matrix approach discussed in section 4.5.2 to find η_e for the assembly the matrix equation [68]

$$\begin{bmatrix} B \\ C \end{bmatrix} = \begin{bmatrix} \cos\delta_2 & \frac{j\sin\delta_2}{\eta_2} \\ j\eta_2\sin\delta_2 & \cos\delta_2 \end{bmatrix} \begin{bmatrix} \cos\delta_3 & \frac{j\sin\delta_3}{\eta_3} \\ j\eta_3\sin\delta_3 & \cos\delta_3 \end{bmatrix} \begin{bmatrix} 1 \\ \eta_4 \end{bmatrix}$$

$$= \begin{bmatrix} \cos\delta_2\left[\cos\delta_3 + j(\eta_4/\eta_3)\sin\delta_3\right] + j\sin\delta_2(\eta_4\cos\delta_3 + j\eta_3\sin\delta_3)/\eta_2 \\ j\eta_2\sin\delta_2\left[\cos\delta_3 + j(\eta_4/\eta_3)\sin\delta_3\right] + \cos\delta_2\left(\eta_4\cos\delta_3 + j\eta_3\sin\delta_3\right) \end{bmatrix}$$

is solved for $\eta_e = \dfrac{C}{B}$. As before, $\eta_e = \eta_1$ is the condition for zero reflection. This is an equation involving complex numbers. Separating the real and imaginary parts gives the following two equations

$$-(\eta_2\eta_4/\eta_3)\sin\delta_2\sin\delta_3 + \eta_4\cos\delta_2\cos\delta_3 = \eta_1\cos\delta_2\cos\delta_3 - (\eta_1\eta_3/\eta_2)\sin\delta_2\sin\delta_3$$

$$\eta_2\sin\delta_2\cos\delta_3 + \eta_3\cos\delta_2\sin\delta_3 = (\eta_1\eta_4/\eta_3)\cos\delta_2\sin\delta_3 + (\eta_1\eta_4/\eta_2)\sin\delta_2\cos\delta_3$$

or equivalently,

$$\tan\delta_2\tan\delta_3 = \frac{\eta_2\eta_3(\eta_4 - \eta_1)}{(\eta_2^2\eta_4 - \eta_1\eta_3^2)} \tag{4.19}$$

$$\frac{\tan\delta_3}{\tan\delta_2} = \frac{\eta_3(\eta_1\eta_4 - \eta_2^2)}{\eta_2(\eta_3^2 - \eta_1\eta_4)} \tag{4.20}$$

which can be manipulated to yield [68]

$$\tan^2\delta_2 = \frac{(\eta_4 - \eta_1)(\eta_3^2 - \eta_1\eta_4)\eta_2^2}{(\eta_2^2\eta_4 - \eta_1\eta_3^2)(\eta_1\eta_4 - \eta_2^2)} \tag{4.21}$$

$$\tan^2\delta_3 = \frac{(\eta_4 - \eta_1)(\eta_1\eta_4 - \eta_2^2)\eta_3^2}{(\eta_2^2\eta_4 - \eta_1\eta_3^2)(\eta_3^2 - \eta_1\eta_4)} \tag{4.22}$$

The values of δ_2 and δ_3 obtained from these equations must be correctly paired using the preceding equations.

For solutions to exist the right hand sides of (4.21) and (4.22) must be positive. Two situations are distinguished where $\eta_1 < \eta_4$ or the other way around. The former situation requires that, of the expressions

$$\eta_3^2 - \eta_1\eta_4 \tag{4.23}$$

$$\eta_2^2\eta_4 - \eta_1\eta_3^2 \tag{4.24}$$

$$\eta_1\eta_4 - \eta_3^2 \tag{4.25}$$

either all three be positive, or only one be positive and the other two be negative. This can be shown on a so-called Schuster diagram (Fig. 4.4). The hatched areas are the allowed regions for the refractive indices of the coating layers. The corresponding diagram for the case where $\eta_1 > \eta_4$ is depicted in Fig. 4.5. After a pair of refractive indices are taken from the diagrams, δ_2 and δ_3 are obtained from (4.21) and (4.22). The refractive indices chosen do not guarantee a wide band AR coating. Here, unlike the single-layer AR coating for which the optimum coating index is unique, we have a two-dimensional search at hand. For simplification, therefore, the special case in which the two coating layers have equal optical thicknesses is followed. Let $\delta_2 = \delta_3 =$

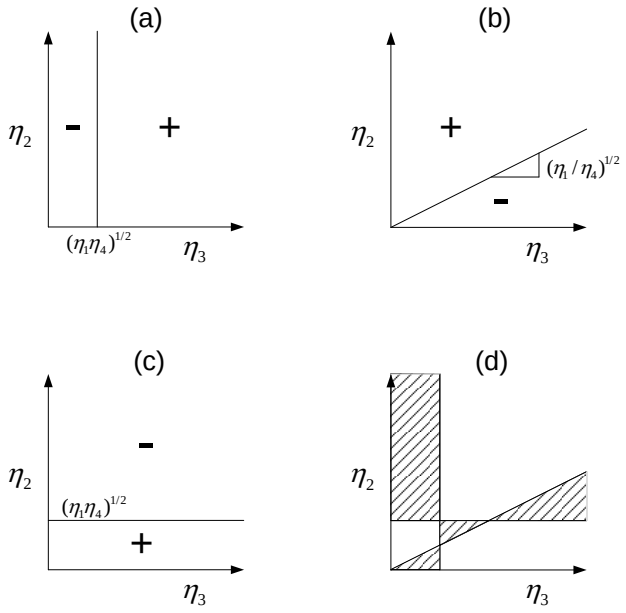

Figure 4.4: Diagram for finding solution region for (4.21) and (4.22) when $\eta_1 < \eta_4$.

δ. If λ_0 is the wavelength at which layers are quarter waves then

$$\delta = \frac{\pi}{2}\left(\frac{\lambda_0}{\lambda}\right)$$

From (4.20) reflectivity is zero when

$$\eta_1\eta_4 = \eta_2\eta_3$$

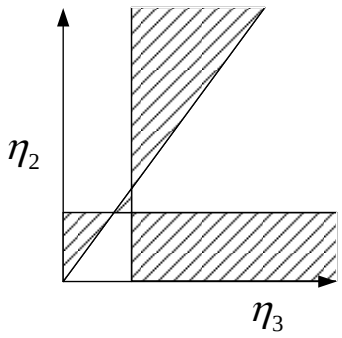

Figure 4.5: Diagram for finding solution region for (4.21) and (4.22) when $\eta_1 > \eta_4$.

The wavelength corresponding to zero reflectivity is found from (4.19)

$$\tan^2\delta = \frac{\eta_1\eta_4(\eta_4 - \eta_1)}{(\eta_2^2\eta_4 - \eta_1\eta_3^2)} \tag{4.26}$$

If $\delta = \delta'$ is a solution in the first quadrant there exists another solution in the second quadrant $\delta = \pi - \delta'$. These solutions have corresponding wavelengths given by

$$\lambda = \left(\frac{\pi/2}{\delta}\right)\lambda_0$$

For each pair of coating layers refractive indices, there are two wavelengths for which reflectivity vanishes and these wavelengths are located at the two sides of the reference wavelength λ_0. This brings about the possibility that by carefully selecting the indices and having the two wavelengths close enough, the response will be wide-band. As before, two cases are distinguished; For $\eta_1 < \eta_4$, to have any solutions $\eta_2^2\eta_4 - \eta_1\eta_3^2$ must be positive or zero. The $\eta_2 - \eta_3$ diagram is shown in Fig. 4.6. When $\eta_1 > \eta_4$, the condition is that $\eta_2^2\eta_4 - \eta_1\eta_3^2$ must be negative or zero (Fig. 4.6). The reflectivity rises to a maximum value at the reference wavelength λ_0. At this wavelength $\delta = \pi/2$

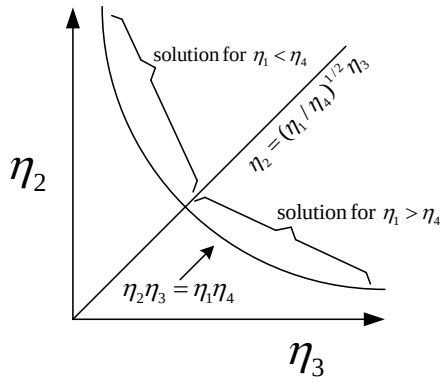

Figure 4.6: Diagram for finding solution region for (4.26).

and the two layers are quarter waves. The optical admittance as seen by the incident wave is $\frac{\eta_2^2}{\eta_3^2}\,\eta_4$ and therefore, the reflectivity is given by

$$R(\lambda_0) = \left(\frac{\eta_1 - (\eta_2^2/\eta_3^2)\eta_4}{\eta_1 + (\eta_2^2/\eta_3^2)\eta_4}\right)^2$$

This value, for both regions in Fig. 4.6 can be shown to become larger as η_2^2/η_3^2 goes away from η_1/η_4. To have a wide band response, therefore, η_2^2/η_3^2 should remain close to η_1/η_4.

Fig. 4.7 shows two examples of double-layer quarter-wave AR coatings designed with the method discussed above. The parameters used are $n_1 = 3.35$, $n_4 = 1$, $\lambda_0 = 1.55\,\mu m$. The incidence in medium 1 is normal. The flat response corresponds to the intersection of the line and the curve in Fig. 4.6, i.e., $n_2 = 2.476$ and $n_3 = 1.353$. For the other response, $n_1 = 2.446$ and n_3 remains unchanged. For the flat curve the bandwidth for $R < 10^{-4}$ is 250 nm. The other curve has a higher reflectivity at λ_0 but has a wider bandwidth. If the reflectivity of $R < 1.5 \times 10^{-4}$ is tolerable a bandwidth of 390 nm is achievable. By trimming the refractive indices of the layers even better

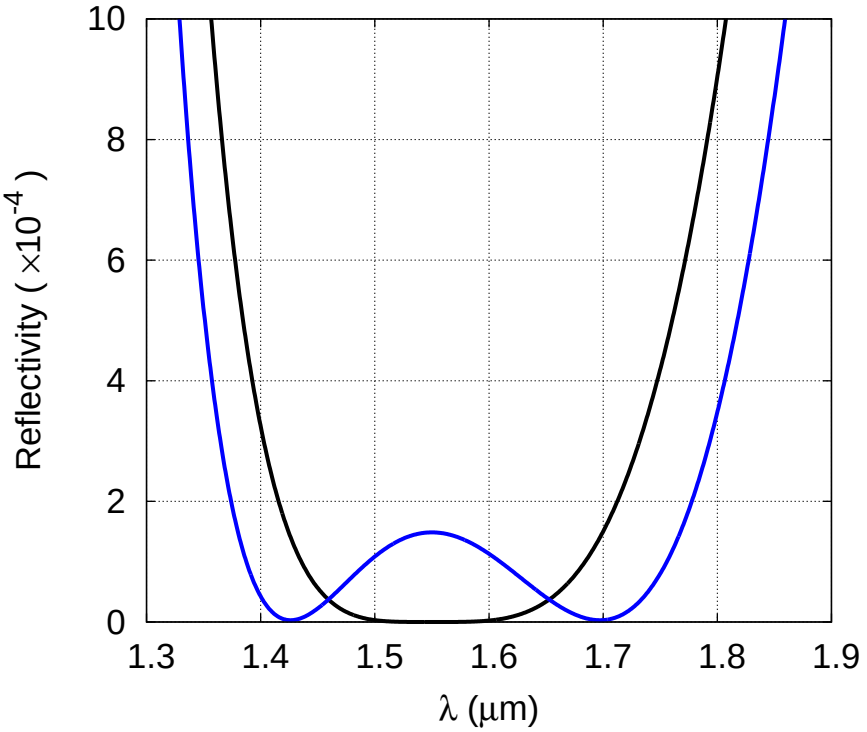

Figure 4.7: Two examples of reflectivity spectrum for normal plane wave incident on two-layer $\lambda/4$ AR coatings as explained in the text.

responses can be found. For example, for $n_2 = 2.435$ and $n_3 = 1.344$ the bandwidth for $R < 10^{-4}$ is 350 nm. In all cases, layers are quarter-wave thick. The disadvantage of multilayer coatings as can be seen from the above numbers is that the response is sensitive to changes in the parameters of coating layers and therefore, fabrication of such structures is challenging.

4.5.5 Waveguide mode reflectivity

The problem of a waveguide facet is different from that of a plane wave incident on a multilayer stack, in the sense that a waveguide mode is not a plane wave and the waveguide medium is not homogeneous. A technique commonly used [70–72] is to replace the waveguide medium with an equivalent homogeneous one and think

of the mode as a spectrum of plane waves superimposed. Each plane wave in the homogeneous medium is then treated as before, i.e., the reflected plane wave from the facet is found using the Fresnel reflection coefficients. The reflected plane waves form the total reflected wave. To find the mode reflection coefficient, one needs to calculate how this reflected wave is coupled to the waveguide mode. This is done by the overlap integral.

Imagine a waveguide along the z direction. The transverse direction is x ($\partial/\partial y = 0$). The waveguide mode is in the form of $e(x)\exp(-j\beta z)$ with $e(x)$ and β being the mode profile and the propagation constant, respectively. At $z = 0$, $e(x)$ can be written as the sum of constituent plane waves using the Fourier transform

$$E_i(s) = \int_{-\infty}^{\infty} e(x)\, e^{j\, k_e\, s\, x}\, dx$$

In this equation $k_e = 2\pi n_e/\lambda_0$ is the wavenumber in the equivalent medium replacing waveguide with refractive index n_e. $E_i(s)$ is the complex amplitude of the constituent plane waves. The relation between s and plane waves' angle θ_1 (see Fig. 4.1) is [71]

$$s = \sin\theta_1$$

The spectrum of the reflected wave is then, simply

$$E_r(s) = r(s)E_i(s)$$

where $r(s)$ is the Fresnel reflection coefficient of a plane wave with angle $\theta_1 = \sin^{-1}s$. Note that s can be any real number; therefore, angles can be imaginary. The reflected

field profile is recovered by taking the inverse Fourier transform of E_r,

$$e_r(x) = \frac{1}{2\pi} \int_{-\infty}^{\infty} E_r(s)\, e^{-jk_e sx} ds$$

Part of the reflected field appears as a backward waveguide mode. The modal reflectivity is given by [71]

$$R = \frac{\left| \int_{-\infty}^{\infty} e(x) e_r(x) dx \right|^2}{\left| \int_{-\infty}^{\infty} e^2(x) dx \right|^2}$$

For the refractive index of the equivalent homogeneous medium, n_e, different values has been used. For a simple dielectric waveguide with core index n_f and cladding index n_c both indices has been reported. A better choice is the effective index of the incident mode $n_e = \beta/k_0$ where β is the propagation index of the mode. For the simulation, the effective index of mode has been used, although for the SP waveguides considered in this thesis, the values of effective mode index and cladding index are very close; because, for the SPWG to be useful at all, metal film thickness cannot exceed a few nanometers. The symmetric mode of such waveguides becomes closer to a plane wave as the film thickness decreases.

Fig. 4.8 shows the mode reflectivity of a thin film SPWG (symmetric mode) versus the film thickness obtained using the above plane wave expansion method. Calculations are made at the wavelength 1550 nm where the 5 nm thick metal film has a dielectric function of $-116 - j11$. The claddings have a dielectric constant of 11.2. The other side of the facet is air. The waveguide has been replaced with a uniform

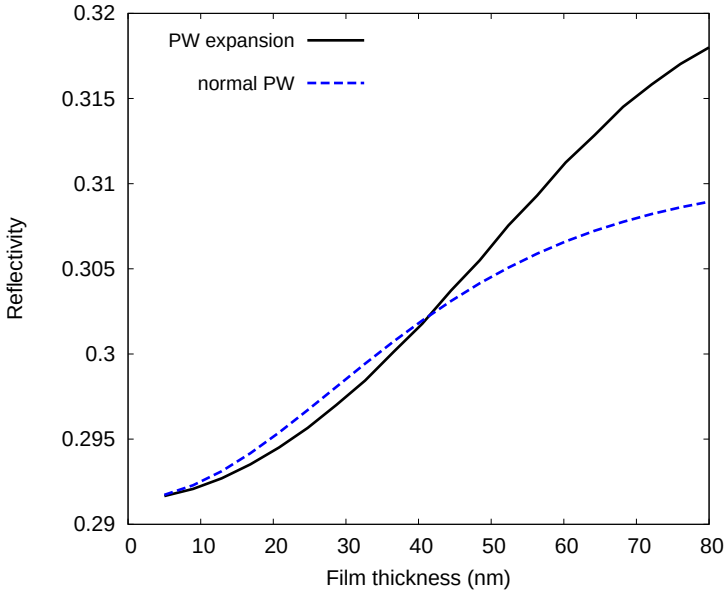

Figure 4.8: Symmetric mode reflectivity of thin-film SPWG with a facet coated by single AR layer.

dielectric of refractive index $n_e = \beta/k_0$. The other curve is obtained when instead of the waveguide mode a normal incident plane wave illuminates the facet. For thin films the symmetric mode becomes more similar to a plane wave and the two curves give close values.

Using a single AR layer the reflectivity can be greatly reduced. For a plane wave a quarter-wave layer of appropriate refractive index will do the job. For a waveguide mode, however, the optimum values of the coating thickness and refractive index are expected to be different. These values for the same SPWG used in the previous figure are shown in Figs. 4.9 and 4.10. The dashed line in Fig. 4.9 corresponds to a normal plane wave in the SPWG's effective index medium for which there is an analytical relation for the optimum refractive index. The coating thickness is normalized by the wavelength in the optimum coating. For a normal plane wave this optimum thickness

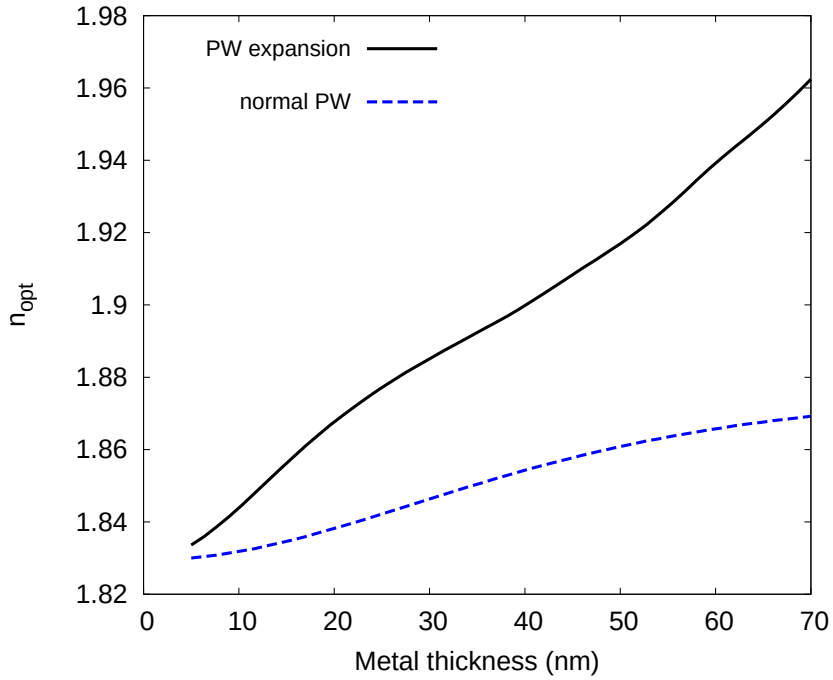

Figure 4.9: Optimum refractive index of single layer ARC for thin film SPWG, difference between normal plane wave and symmetric SPP mode.

is known to be 0.25.

From Figs. 4.9 and (4.10) it seems that the difference in the optimum index and thickness of an AR layer between a normal plane wave and the optical mode is not significant, however, as Fig. 4.11 shows, their related reflectivities are quite different. The bandwidths of low reflectivity ($R < 10^{-4}$) for the plane wave and the SPWG mode are 31 nm and 5 nm, respectively. Therefore, a single layer ARC by itself is not wide band enough for a wide band device. With a two layer ARC, however, as will be shown later on, much wider responses can be achieved.

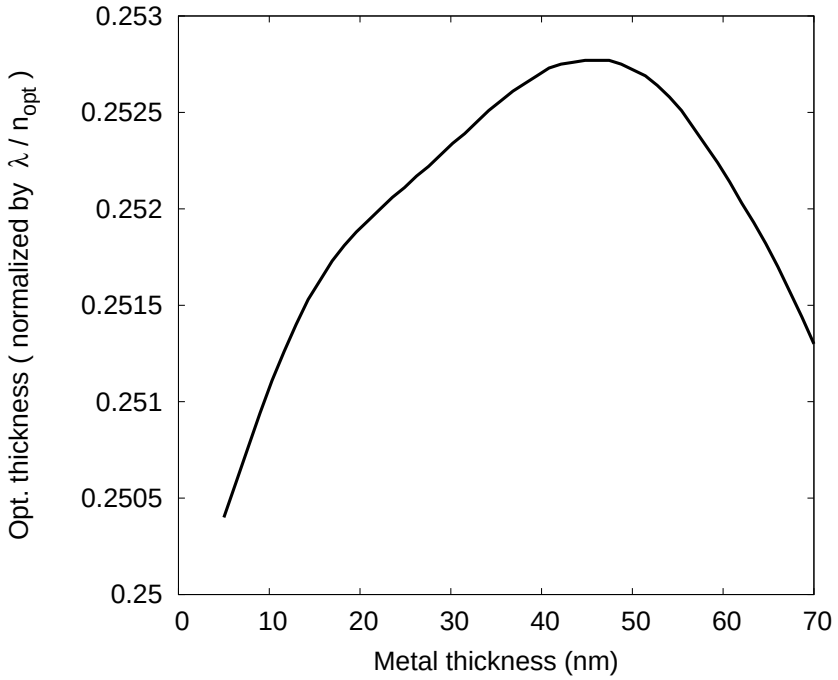

Figure 4.10: Optimum thickness of single layer ARC for thin film SPWG.

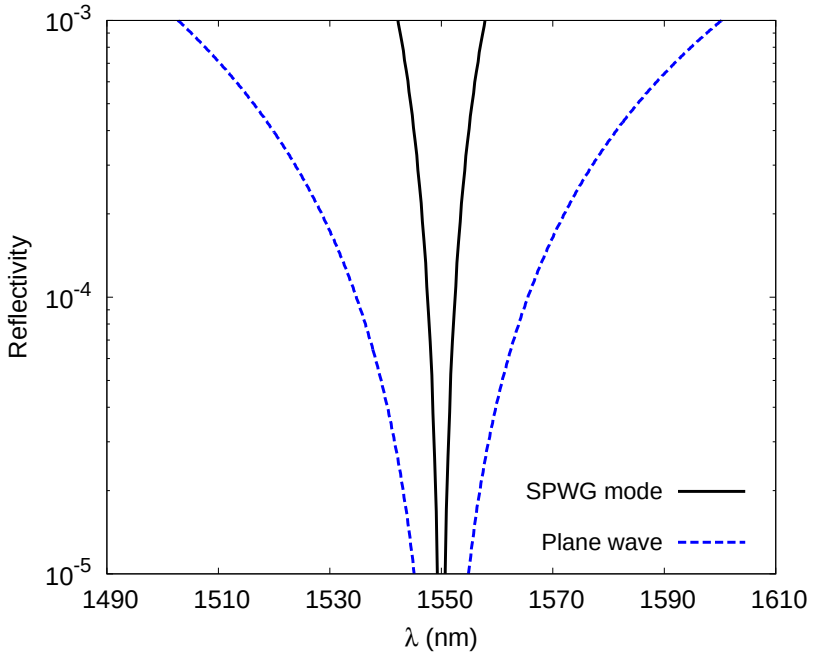

Figure 4.11: Reflectivity spectrum of a single layer ARC for normal incident plane wave and thin film SPWG.

Chapter 5

Numerical Simulation Method

5.1 Introduction

The ever increasing need for accurate numerical simulation of optoelectronic devices cannot be overemphasized. Numerical simulation is cheaper and usually faster than fabrication and characterization of devices during the development and optimization phase. Occasionally, it even uncovers new physical phenomena or inspires new ideas leading to novel devices and applications. For laser diodes, the development of multi-mode rate equations [73, 74] was a milestone in the simulation of dynamic and steady state characteristics. They include one rate equation for the carrier density and one for the photon density of each mode. In this approach the device length and the effects of wave propagation are ignored and therefore, the photon densities are the effective density in the cavity. While this assumption is acceptable for short length Fabry-Perot (FP) devices with a reasonable amount of reflection at the facets, it fails to give accurate results for the cases in which the distributed nature of devices (relative to the wavelength) cannot be neglected. Examples are distributed feedback (DFB)

laser diodes and semiconductor optical amplifiers (SOA) where the device length is hundreds, even thousands of times larger than the wavelength. In DFB laser diodes the phase of forward/backward waves could prove crucial, for instance, in determining the dominant mode. In SOA's the distributions of carrier and photon densities vary considerably along the direction of propagation leading to such effects as gain saturation and spatial hole burning (SHB). The remedy is, naturally, to modify the rate equations so as to include space variable(s) [75–77]. This leads to two wave equations for the fields or power of each mode and a single rate equation for the carrier density which is now a function of time and space. Another shortcoming of the original rate equations is that they are inherently narrow band, that is, the wide band nature of material gain and spontaneous emission is disregarded. This, obviously, does not work for wideband devices like SOA and SLD. To account for both spatial and spectral variations of the parameters we use multi wavelength time domain methods [78–81]. Three versions of such methods are developed for SOA's. The three methods differ in the way they treat spontaneous emission and signal waves. We call them, following [82], full-power, half-wave, and full-wave models. In the full-power model both signal(s) and spontaneous emission are treated as power waves, i.e., all phase information is discarded. The immediate implication is that any signal-spontaneous and spontaneous-spontaneous interaction is ignored. In the half-wave model any signal is represented with a complex amplitude with phase information kept, but, spontaneous emission is treated as power waves neglecting the randomness effects. In this case separate equations for signal and spontaneous emission are solved. It follows that any coupling of the spontaneous emission to signal is lost. Finally, in the full-wave model both signal and spontaneous emission fields are considered as complex amplitudes.

Since in SLD there is no signal, only full-power and full-wave models are relevant, which is explained in the following.

5.2 Full-power method

The multi wavelength time domain models are spectrum slicing methods in which the significant spectral range of the amplified spontaneous emission (ASE) spectrum is divided into many slices or segments. The optical field in each segment is described by two coupled traveling wave equations for the forward/backward waves [10],

$$\frac{1}{v_g}\frac{\partial P_{f,r}(z,t,\lambda_k)}{\partial t} \pm \frac{\partial P_{f,r}(z,t,\lambda_k)}{\partial z} = \left[\Gamma g(z,t,\lambda_k) - \alpha\right] P_{f,r}(z,t,\lambda_k) + P^s_{f,r}(z,t,\lambda_k) \quad (5.1)$$

where P_f and P_r [J/s] are the optical powers of the forward (f) and reverse (r) waves traveling along the device, respectively. In SLD, this power is the amplified spontaneous emission originating from the source term $P^s_{f,r}$. In the above equation the dependence of optical power on position, time and wavelength is explicitly shown. Note that only one space variable is used and therefore, the model is one-dimensional (z is the direction along the wave propagation). λ_k ($k = 1, 2, , N_s$) is the centre frequency of the k-th spectral segment. v_g [cm/s] is the group velocity, Γ is the confinement factor, g [1/cm] is the material gain which other than position, time and wavelength implicitly depends on the carrier density, α [1/cm] is the modal loss along the cavity. $P^s_{f,r}$ [J/(cm.s)] denotes the spontaneous emission power coupled from each wavelength segment into the traveling optical powers and is given by [83]

$$P^s_{f,r} = \beta A h \nu_k R_{sp}$$

Here, β is the spontaneous emission coupling factor, A is the active region cross section, $h\nu_k$ is the average photon energy in the k-th spectral section and $R_{sp}(z,t,\lambda_k)$ [1/(cm^3.s)] is the rate of spontaneous photon generation into a spectral section per unit volume.

5.3 Full-wave model

In this model phase of the optical field inside the cavity is preserved. The governing equations in each wavelength section are [81, 84],

$$\frac{1}{v_g}\frac{\partial E_{f,r}(z,t,\lambda_k)}{\partial t} \pm \frac{\partial E_{f,r}(z,t,\lambda_k)}{\partial z} =$$

$$\left[-j\left(\gamma(\lambda_k)+\frac{1}{2}\Gamma\alpha_m g(z,t,\lambda_k)\right)+\frac{1}{2}\left(\Gamma g(z,t,\lambda_k)-\alpha\right)\right]E_{f,r}(z,t,\lambda_k)+\tilde{s}_{f,r}(z,t,\lambda_k) \tag{5.2}$$

with $E_{f,r}$ [1/cm$^{3/2}$] denoting the forward/backward complex traveling waves, α_m the linewidth enhancement factor, $\gamma(\lambda_k)$ [1/cm] the modal propagation constant and $\tilde{s}_{f,r}$ [1/cm$^{5/2}$] the contribution of the spontaneous emission of the corresponding spectral section. $\tilde{s}_{f,r}$ is a random complex number with Gaussian or Poissonian distribution satisfying [85]

$$\left\langle \tilde{s}_{f,r}\tilde{s}^*_{f,r}\right\rangle = \beta\frac{R_{sp}}{d_z v_g}\delta\left((z-z')(t-t')(\lambda_k-\lambda_{k'})\right)$$

d_z is the length of device or a subsection of it and $\delta(\cdot)$ is the Dirac delta function.

5.4 Boundary conditions

Assuming the device is along the z direction with its left end at $z = 0$, and its right end at $z = L$, the following boundary conditions are satisfied,

$$P_f(0, t, \lambda_k) = R_l P_r(0, t, \lambda_k) \tag{5.3}$$

$$P_r(L, t, \lambda_k) = R_r P_f(L, t, \lambda_k) \tag{5.4}$$

for the optical powers (introduced in the full-power model) and

$$E_f(0, t, \lambda_k) = \sqrt{R_l} E_r(0, t, \lambda_k) \tag{5.5}$$

$$E_r(L, t, \lambda_k) = \sqrt{R_r} E_f(L, t, \lambda_k) \tag{5.6}$$

for the optical fields in the full-wave model. R_r and R_l are the respective power reflectivities of the right and left facets and L is the device length. The output power of, say, the right facet in the two models are obtained by

$$P_{out}(t) = (1 - R_r) \sum_{k=1}^{N_s} P_f(L, t, \lambda_k)$$

$$P_{out}(t) = (1 - R_r) \sum_{k=1}^{N_s} h\nu_k v_g A_{eff} |E_f(L, t, \lambda_k)|^2$$

where summation is performed on the contributions from all spectral sections and A_{eff} is the effective active area which is related to the device cross section by

$$A_{eff} = \frac{A}{\Gamma}$$

It should be noted that, since in the full-wave model equations random numbers are used, $E_{f,r}$ fluctuates with time and therefore, time averaging is necessary to obtain a smooth $P_{out}(t)$.

5.5 Carrier rate equation

Optical fields and powers of all spectral sections are coupled by a common pool of carriers. The carrier density is obtained by the following rate equation [83]

$$\frac{\partial N(z,t)}{\partial t} = \eta \frac{J}{ed} - \left[A + BN(z,t) + CN^2(z,t)\right] N(z,t) - R_{stim}(z,t) \tag{5.7}$$

with η the carrier injection efficiency; A [1/s] the nonradiative (Shockley-Reed-Hall) recombination coefficient; B [cm^3/s] the bimolecular recombination coefficient which is related to the rate of spontaneous photon generation; C [cm^6/s] the Auger recombination coefficient; and, d the active region thickness. $R_{stim}(z,t)$ [1/cm$^3 \cdot$ s] is the stimulated recombination rate which is given by [10]

$$R_{stim}(z,t) = \sum_{k=1}^{N_s} \frac{\Gamma g(z,t,\lambda_k)\left[P_f(z,t,\lambda_k) + P_r(z,t,\lambda_k)\right]}{h\nu_k A}$$

for the full-power model and by [84]

$$R_{stim}(z,t) = \sum_{k=1}^{N_s} \Gamma v_g g(z,t,\lambda_k) \left| E_f(z,t,\lambda_k) + E_r(z,t,\lambda_k) \right|^2$$

for the full-wave model.

5.6 Material gain

Under sufficient current injection the semiconductor material becomes optically active and exhibits optical gain (also called material gain). Gain is, therefore, a function of density of carriers inside the active region. The dependence is different for bulk and quantum well active regions and different gain models should be used in each case. We adopt formulas developed in [86]. For bulk material, the gain spectrum is found by

$$g(E) = \frac{\pi\hbar e^2}{n_r c\epsilon_0 m_0^2 E}|M_{if}|^2 \int_0^\infty \rho_r(E') \frac{\Gamma/2\pi}{(E_g + E' - E)^2 + (\Gamma/2)^2} \left[f_c(E') - f_v(E')\right] dE'$$

which expresses g at any frequency or wavelength through $E = \hbar\omega = \dfrac{hc}{\lambda}$. Parameters used in this equation are: e the elementary charge; c the speed of light; $\hbar$ the reduced Planck constant; m_0 the free electron mass; n_r the refractive index of the active region; $|M_{if}|^2$ the momentum matrix element, which links the transition between initial and final states; ρ_r the reduced density of states which is given by

$$\rho_r = \frac{1}{2\pi^2}\left(\frac{2m_r}{\hbar^2}\right)^{3/2} E^{1/2}$$

and in which m_r is the reduced mass defined by

$$m_r = \left(\frac{1}{m_e} + \frac{1}{m_h}\right)^{-1}$$

with m_e and m_h being, respectively, the effective electron mass in the conduction band and effective hole mass in the valence band; E_g the semiconductor band gap

energy; Γ the linewidth factor; and, f_c and f_v, Fermi-Dirac distribution functions for the electrons in the conduction and valence bands, respectively, described by,

$$f_c(E) = \frac{1}{1 + \exp\left\{\dfrac{E_g + (m_r/m_e)E - F_c}{k_B T}\right\}}$$

$$f_v(E) = \frac{1}{1 + \exp\left\{\dfrac{-(m_r/m_h)E - F_v}{k_B T}\right\}}$$

Energy values, E, used in these equations are measured from the top of the valence band upward toward the conduction band (so that energy in the valence band is negative).

Also, k_B is the Boltzmann constant, T is the absolute temperature, and F_c and F_v are the quasi-Fermi energy levels.

In this case the momentum matrix element is given by

$$|M_{ij}|^2 = \frac{1}{6} m_0 E_p$$

The energy constant E_p can be found in tables of semiconductor properties. The spectrum of the spontaneous emission rate per unit volume per unit energy [1/(s.cm^3.J)] is calculated through,

$$R_{spon}(E) = \frac{n_r e^2 E}{\pi \hbar^2 c^3 \epsilon_0 m_0^2} |M_{if}|^2 \int_0^\infty \rho_r(E') \frac{\Gamma/2\pi}{\left(E_g + E' - E\right)^2 + \left(\Gamma/2\right)^2} \times f_c(E') \left[1 - f_v(E')\right] dE'$$

This is related to the spontaneous rate R_{sp} defined earlier by,

$$R_{sp} = h\Delta\nu_k R_{spon}$$

where $\Delta\nu_k$ measured in frequency is the width of the k-th spectral section. In quantum well active regions the electron-hole transitions occur between a number of conduction and valence sub bands as a result of energy discretization due to quantum confinement of carriers. For gain calculations, transitions between these bands must be taken into account. For quantum well active regions we have used the following formula for the gain,

$$g(E) = \frac{\pi\hbar e^2}{n_r c\epsilon_0 m_0^2 E} \sum_n \sum_m |I_{hm}^{en}|^2 \int_0^\infty \rho_r^{2D}(E_t)|M_{if}|^2 \times \frac{\Gamma/2\pi}{\left(E_{hm}^{en} + E_t - E\right)^2 + (\Gamma/2)^2} \left[f_c^n(E_t) - f_v^m(E_t)\right] dE_t \tag{5.8}$$

Double summation in this relation ensures contributions of transitions between all sub bands are considered. n counts the conduction sub bands. Similarly, m is used to count the valence sub bands. Note that, the summation includes heavy-hole, light-hole and split-off valence bands. New parameters included are: I_{hm}^{en} the overlap integral of the conduction and valence band envelope functions given by

$$I_{hm}^{en} = \int_{-\infty}^{\infty} \phi_n(x) g_m(x) dx$$

For the limiting case of an infinite quantum well I_{hm}^{en} reduces to δ_{mn} as the envelope functions in this case are orthogonal.

ρ_r^{2D} the two-dimensional reduced density of states function is given as

$$\rho_r^{2D} = \frac{m_r}{\pi\hbar^2 L_x}$$

with L_x the width of quantum well. E_{hm}^{en} the energy difference between the edge of the n-th conduction sub band and the m-th valence sub band, is defined as

$$E_{hm}^{en} = E_g + E_{en} - E_{hm}$$

where E_{en} is the energy difference between the bottom of the n-th parabolic conduction sub band and the bottom of the conduction band. Similarly, E_{hm} is the energy difference between the top of the m-th valence sub band and the top of the valence band. Due to the chosen direction of energy values, $E_{hm} < 0$. f_c^n and f_v^m, Fermi-Dirac distribution functions of conduction and valence sub bands are calculated as,

$$f_c^n(E_t) = \frac{1}{1 + \exp\left\{\dfrac{E_g + E_{en} + (m_r/m_e)E_t - F_c}{k_B T}\right\}} \tag{5.9}$$

$$f_v^m(E_t) = \frac{1}{1 + \exp\left\{\dfrac{E_{hm} - (m_r/m_h)E_t - F_v}{k_B T}\right\}} \tag{5.10}$$

$|M_{if}|^2$ the momentum matrix element depends on polarization. For transitions between the conduction and heavy-hole bands we use the following relations

$$|M_{if}|^2 = \frac{3}{4}\left(1 + \cos^2\theta_{nm}\right) M_b^2 \qquad \text{TE polarization}$$

$$|M_{if}|^2 = \frac{3}{2}\sin^2\theta_{nm} M_b^2 \qquad \text{TM polarization}$$

For transitions between the conduction and light-hole bands the corresponding relations are,

$$|M_{if}|^2 = \left(\frac{5}{4} - \frac{3}{4}\cos^2\theta_{nm}\right) M_b^2 \qquad \text{TE polarization}$$

$$|M_{if}|^2 = \frac{1}{2}\left(1 + 3\cos^2\theta_{nm}\right) M_b^2 \qquad \text{TM polarization}$$

In the above relations M_b^2 is the momentum matrix element for bulk material which was given before and

$$\cos^2\theta_{nm} = \frac{E_{en} - E_{hm}}{E_{en} - E_{hm} + (\hbar k_t^2/2m_r)}$$

where $\hbar k_t^2/2m_r = E_t$ is the integration variable of (5.8). In order to calculate Fermi distributions in equations (5.9) and (5.10) quasi-Fermi energy levels must be obtained first. These quantities are functions of the density of carriers (either injected or due to background doping), which in general occupy several conduction and valence sub bands. The numbers of electrons occupying the n-th conduction sub band and holes occupying the m-th valence sub band as functions of quasi-Fermi levels, F_c and F_v are

$$N_n = \frac{m_e k_B T}{\pi\hbar^2 L_x} \ln\left(1 + e^{(F_c - E_{en})/k_B T}\right) \tag{5.11}$$

$$P_m = \frac{m_h k_B T}{\pi\hbar^2 L_x} \ln\left(1 + e^{(E_{hm} - F_v)/k_B T}\right) \tag{5.12}$$

The total number of electrons and holes in the conduction and valence bands is of course

$$N = \sum_n N_n \tag{5.13}$$

and

$$P = \sum_m P_m \tag{5.14}$$

In numerical calculations for a given N, we start with a guess for F_c and calculate N_n for all significantly occupied sub bands from (5.11) (e.g., sub bands for which the guessed F_c is bigger than E_{en}). The sum of these electrons is then compared with N and a new guess for F_c is determined, accordingly. These steps are repeated until (5.13) is satisfied to a preset precision. A similar procedure is carried out to find F_v.

The spontaneous emission spectrum for a QW active region is given by

$$R_{sp}(E) = \frac{n_r e^2 E}{\pi \hbar^2 c^3 \epsilon_0 m_0^2} \sum_n \sum_m |I_{hm}^{en}|^2 \int_0^\infty \rho_r^{2D}(E_t) |M_{if}|^2 \times \frac{\Gamma/2\pi}{\left(E_{hm}^{en} + E_t - E\right)^2 + (\Gamma/2)^2} f_c^n(E_t) \left[1 - f_v^m(E_t)\right] dE_t$$

Its numerical calculation is similar to the material gain.

5.7 Numerical implementation

A computer program has been developed to implement numerically the aforementioned models described by the partial differential equations (5.1), (5.2) and (5.7) subject to the boundary conditions (5.3), (5.4), (5.5) and (5.6). We have used the forward finite difference method [87] and discretize time (t), space (z) and wavelength (λ) variables. The device length is divided into M small sections each with length Δz. A value for carrier density is assigned to every section. The discrete values of power or field wave are defined at interfaces between sections as shown in Fig. 5.1. The relevant part of the spontaneous emission spectrum is also divided into several regions of

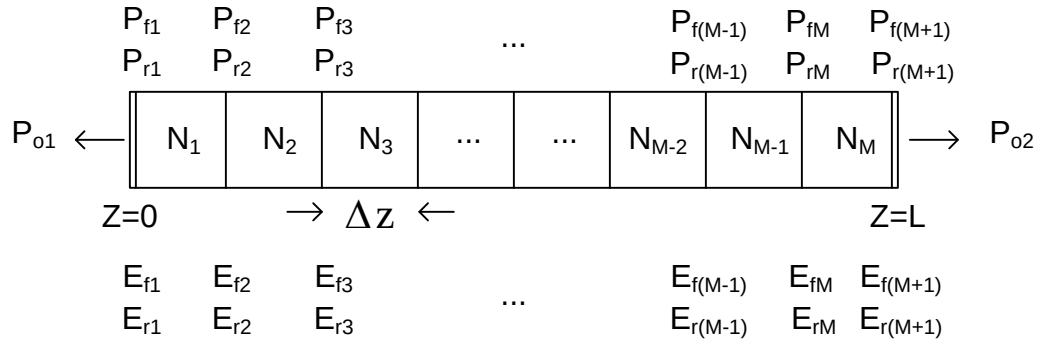

Figure 5.1: Spatial discretization of device.

equal length (in frequency). Governing equations of the full-power technique, (5.1), are now discretized

$$P_f(z+\Delta z, t+\Delta t, \lambda_k) = \exp\left[(\Gamma g(z,t,\lambda_k) - \alpha)\Delta z\right] P_f(z,t,\lambda_k) + \Delta z A \beta h \nu_k R_{sp}(z,t,\lambda_k) \tag{5.15}$$

$$P_r(z-\Delta z, t+\Delta t, \lambda_k) = \exp\left[(\Gamma g(z,t,\lambda_k) - \alpha)\Delta z\right] P_r(z,t,\lambda_k) + \Delta z A \beta h \nu_k R_{sp}(z,t,\lambda_k) \tag{5.16}$$

and (5.2) for the full-wave technique

$$\begin{aligned} &E_f(z+\Delta z, t+\Delta t, \lambda_k) = \\ &\exp\left\{-j\left[\gamma(\lambda_k) + \frac{1}{2}\Gamma\alpha_m g(z,t,\lambda_k)\right]\Delta z + \left[\frac{1}{2}(\Gamma g(z,t,\lambda_k) - \alpha)\right]\Delta z\right\} E_f(z,t,\lambda_k) \\ &+ \Delta z\sqrt{\beta\frac{R_{sp}(z,t,\lambda_k)}{\Delta z v_g}}\exp(j\phi) \end{aligned} \tag{5.17}$$

$$E_r(z-\Delta z, t+\Delta t, \lambda_k) =$$

$$\exp\left\{-j\left[\gamma(\lambda_k)+\frac{1}{2}\Gamma\alpha_m g(z,t,\lambda_k)\right]\Delta z+\left[\frac{1}{2}(\Gamma g(z,t,\lambda_k)-\alpha)\right]\Delta z\right\}E_r(z,t,\lambda_k)$$

$$+\Delta z\sqrt{\beta\frac{R_{sp}(z,t,\lambda_k)}{\Delta z v_g}}\exp(j\phi) \tag{5.18}$$

ϕ is a random phase. In the above wave equations it is assumed that

$$\Delta t=\frac{\Delta z}{v_g} \tag{5.19}$$

Carrier rate equation, (5.7), is now discretized as

$$N(z,t+\Delta t)=\left\{1+\Delta t\left[\eta\frac{J}{ed}-\left(A+BN(z,t)+CN^2(z,t)\right)\right]\right\}N(z,t)-R_{stim}(z,t)\Delta t$$

The above discretized optical power/field equations are repeated for every spectral subsection. Therefore, if there are K spectral subsections, a total of $(2K+1)$ equations, including the carrier rate equation must be numerically solved. Clearly, the number of spatial and spectral subsections directly affect the simulation run time. The greater those numbers, the longer the simulation time and the less the efficiency. In our implementation, we have increased the number of spatial/spectral subsections until the accuracy of the output results would not change more than a few percent (e.g. 2%). This ensures the best efficiency and accuracy possible. For a device that only operates based on the amplified spontaneous emission and there is no signal wave, the full-wave model gives no information beyond what obtained from the full-power model. In this case the two models are equivalent as we show here. Equation

(5.17) can be written as (see Appendix A),

$$|E_f(z+\Delta z, t+\Delta t, \lambda_k)|^2 =$$

$$\exp\left\{(\Gamma g(z,t,\lambda_k)-\alpha)\Delta z\right\}|E_f(z,t,\lambda_k)|^2 + \Delta z\beta\frac{R_{sp}(z,t,\lambda_k)}{v_g} +$$

$$2\exp\left\{\left[\frac{1}{2}(\Gamma g(z,t,\lambda_k)-\alpha)\right]\Delta z\right\}|E_f(z,t,\lambda_k)|\cdot\Delta z\sqrt{\beta\frac{R_{sp}(z,t,\lambda_k)}{\Delta z v_g}}\cos(\theta-\phi) \tag{5.20}$$

where θ is a deterministic phase. Since ϕ is a random phase with uniform distribution over [0, 2π], the last term vanishes upon taking the average. Using [84]

$$P_f(z,t,\,\lambda_k) = h\nu_k v_g A\left\langle|E_f(z,t,\,\lambda_k)|^2\right\rangle$$

(5.20) reduces to

$$\begin{aligned}P_f(z+\Delta z, t+\Delta t,\,\lambda_k) = \exp\left\{(\Gamma g(z,t,\lambda_k)-\alpha)\Delta z\right\}P_f(z,t,\lambda_k)\\ + \Delta z\,A\,\beta\,h\nu_k\,R_{sp}(z,t,\,\lambda_k)\end{aligned}$$

which is identical to (5.15). Similar treatment applies to the backward waves. For SOA devices the two models are not equivalent because, clearly, the full-power model neglects the phase of the optical channel signal and its interaction with the spontaneous emission.

A flow chart of the numerical algorithm implemented to simulate SLD operation is shown in Fig. 5.2. Time steps, according to (5.19) are very small, typically a fraction of one picosecond, and the simulator continues to about a few nanoseconds before the steady state is reached. This shows that usually thousands or tens of thousands

of time steps are required. Calculating material gain and spontaneous emission spectrum for every time step is a considerable numerical burden. To increase efficiency, gain and spontaneous emission spectrum are first calculated for several values of the carrier density over a reasonable range. The curves are then fitted with suitable approximating functions. The coefficients of these approximating functions, in turn, are functions of carrier density and are fitted with other approximating functions. Using the coefficients obtained in this way, gain and spontaneous emission spectra are interpolated during the simulation leading to efficient spectrum calculations.

As an example we show the simulation results of a bulk InGaAs/InP SLD operating at wavelength of 1.5 μm. Structural and material parameters used are listed in Table (5.1). First, device length is fixed at 500 μm and is divided into 21 sections. The injection current is changed as a parameter. The output power is shown in Fig. 5.3. As expected, unlike the L-I curve of a laser diode there is no sharp turn, which is the onset of threshold, seen. Rather, the curve increases smoothly. If the injection current is fixed at 100 mA and the device length is changed the graph shown in Fig. 5.4 is obtained for the output power.

As device length increases power first increases and at about $L = 430\,\mu m$ reaches its maximum, then decreases. The reason for this behaviour can be explained from the device gain expression, (1.3)

$$G(N) = L\Gamma g_0(N)$$

For very short devices, device gain is small and the output power is low. For very long devices, the injected carriers distribute in a larger volume and therefore the carrier density is low. This directly affects material gain and, as a result, device gain is again

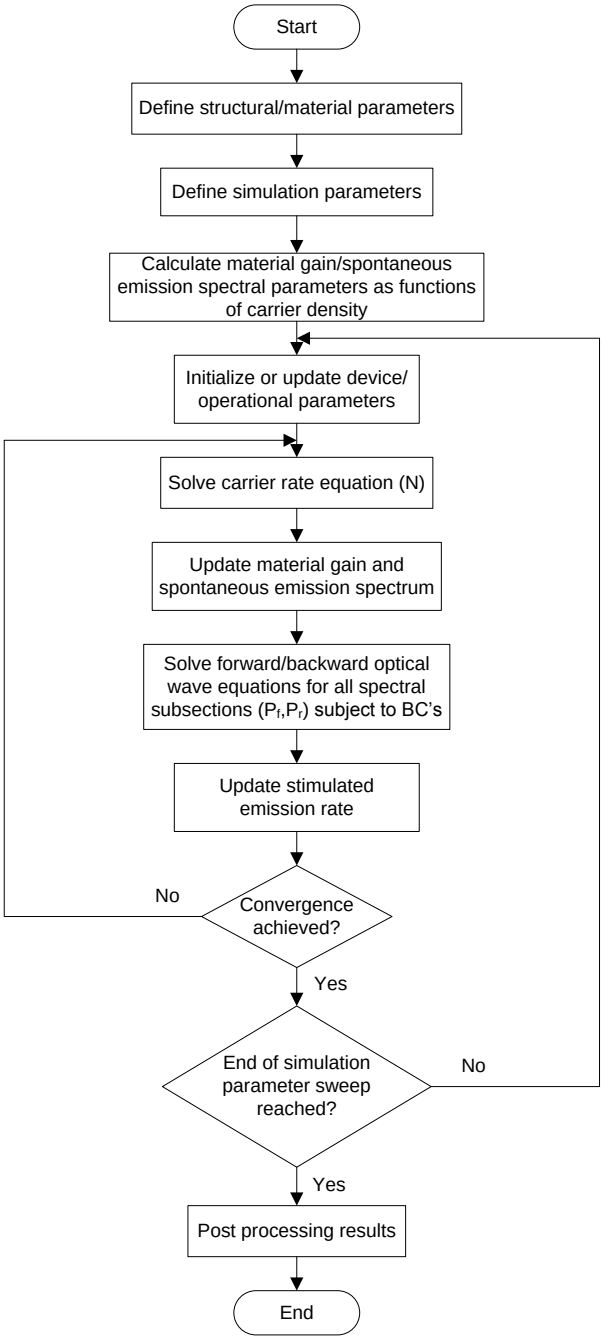

Figure 5.2: Flow chart of the algorithm for numerical simulation of SLD.

Table 5.1: Device structural and material parameters

Symbol	Description	Value
L, w, d	Active region dimensions	$500, 2, 0.2\ \mu m$
R_r, R_l	right, left facet reflectivities	5×10^{-5}
Γ	confinement factor	0.3
η	current injection efficiency	1
α	optical power absorption coefficient	50 cm^{-1}
β	spontaneous emission coupling factor	0.01
N_t	transparency carrier density	10^{24} cm^{-3}
n_g	group refractive index	4.1798
v_g	group velocity	c/n_g
n_r	refractive index of InGaAsP active region	3.5705
T	device temperature	297 K
y	mole fraction of Arsenide	0.892
x	mole fraction of Gallium	0.419
m_e	effective mass of conduction band electron	$0.0452\ m_0$
m_{hh}	effective mass of heavy hole	$0.46\ m_0$
m_{lh}	effective mass of light hole	$0.0556\ m_0$
A	nonradiative recombination coefficient	2.8×10^8 s^{-1}
B	bimolecular radiative recombination coefficient	10^{-10} cm^3s^{-1}
C	Auger recombination coefficient	$3.5 \times 10^{-29}\text{cm}^6\text{s}^{-1}$

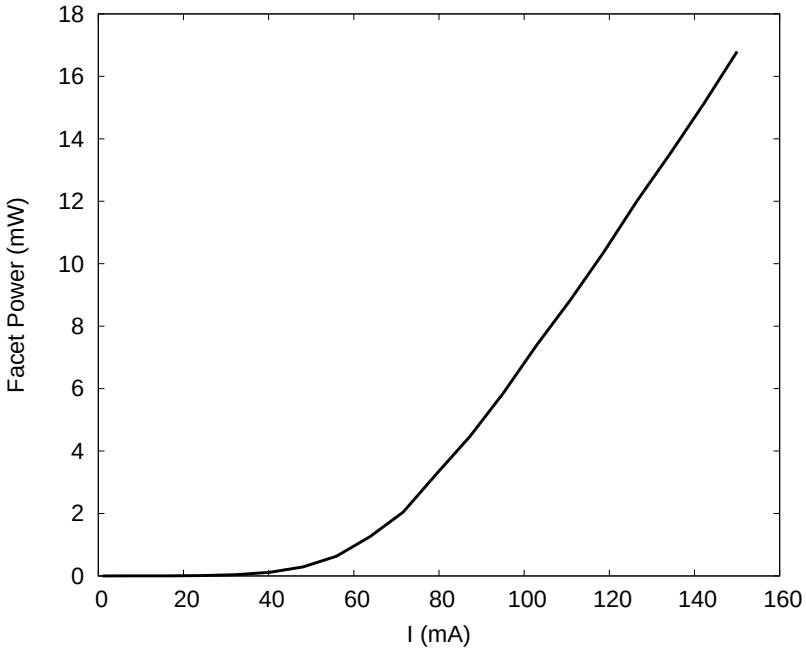

Figure 5.3: Variation of output power with device current for the sample SLD.

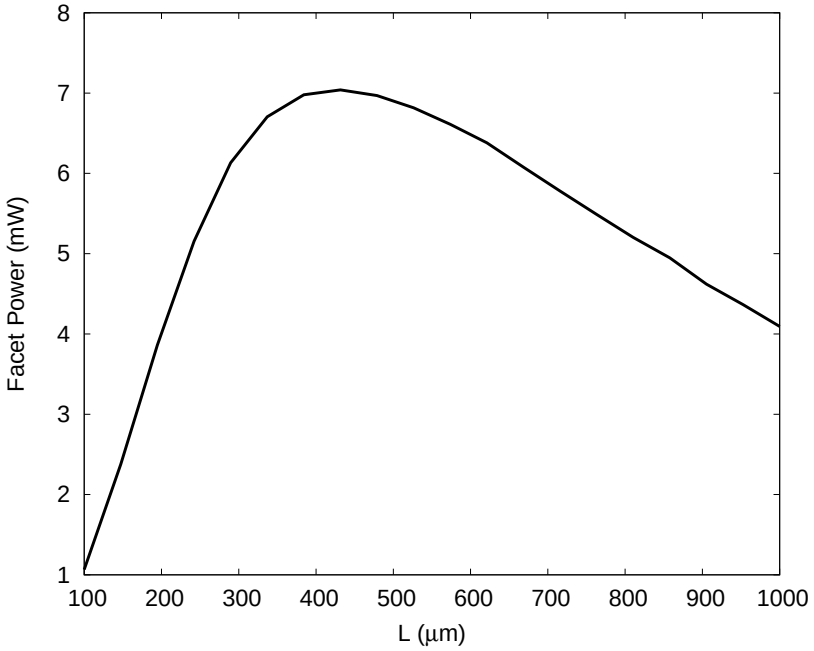

Figure 5.4: Variation of output power with device length for the sample SLD.

decreased. Hence, the output power curve has a peak at $L \approx 300\,\mu m$. Fig. 5.5 shows the forward/backward travelling power waves along the device length ($L = 1000\,\mu m$). The sum of the two curves is the total optical power at any position along the device. As apparent from the figure, the total power inside the device is nonuniform; for the given simulation parameters it is maximum at the two device ends and minimum at the middle. Consequently, the rate of stimulated emission is higher at the two ends. It is, therefore, expected that the carrier density distribution along the device length is maximum at the middle of the device (see Fig. 5.5 for $L = 1000\,\mu m$). The spectrum of the amplified spontaneous emission for two devices of lengths 100 μm and 1000 μm is depicted in Fig. 5.7. As explained in chapter 1 the ASE spectrum of the shorter device is broader. The dotted curve near that of the longest device is an approximation where material gain is assumed to be constant throughout the device length and equal to its average value. Further, the spontaneous power generated in every longitudinal section has been set equal to the spontaneous power generated in the first section. Using those values, the output power can be obtained analytically. The difference between the two curves shows the effects of the longitudinal spatial hole burning (LSHB). Fig. 5.8 shows the linewidth of the output power versus device length.

Accordingly, for applications where higher linewidth is required shorter devices should be sought. Many applications do not like the trade off between the output power and linewidth as they need both high power and high linewidth. Fig. 5.9 shows the power-linewidth product of the simulated device as the device length changes. Again, at $L \approx 300\,\mu m$ the product takes a maximum value, but this optimal length is different from the length at which the output power is the highest ($\approx 400\,\mu m$).

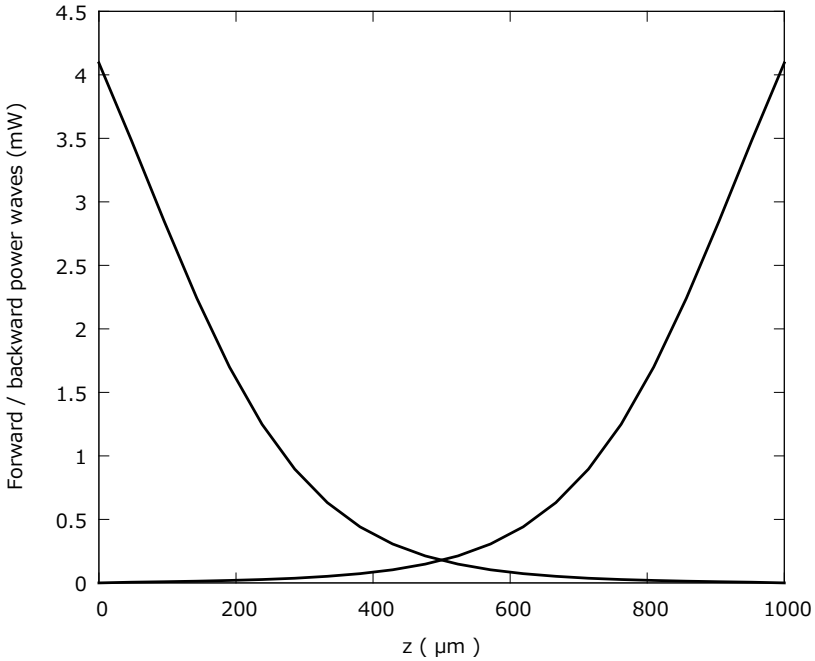

Figure 5.5: Forward and backward traveling optical power waves in the sample SLD.

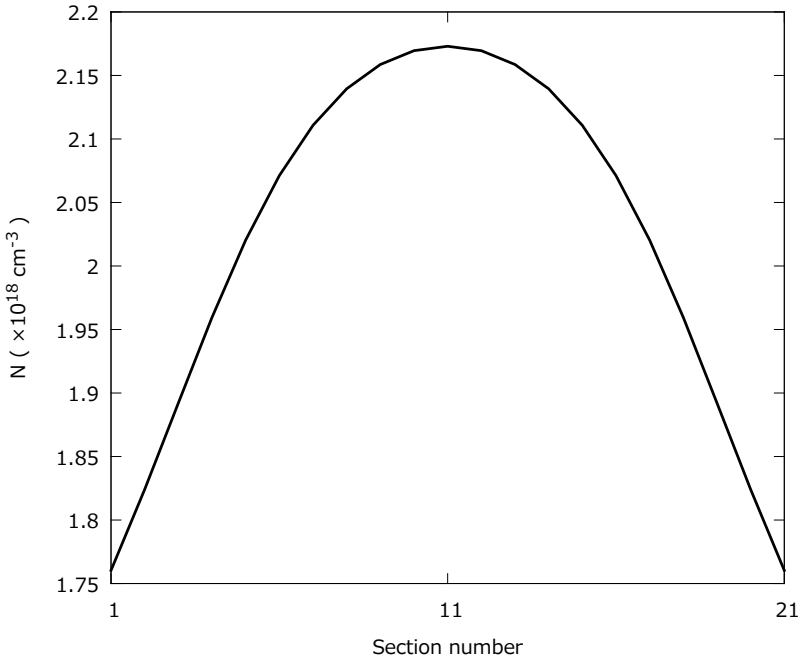

Figure 5.6: Variation of carrier density along the sample SLD showing its nonuniformity.

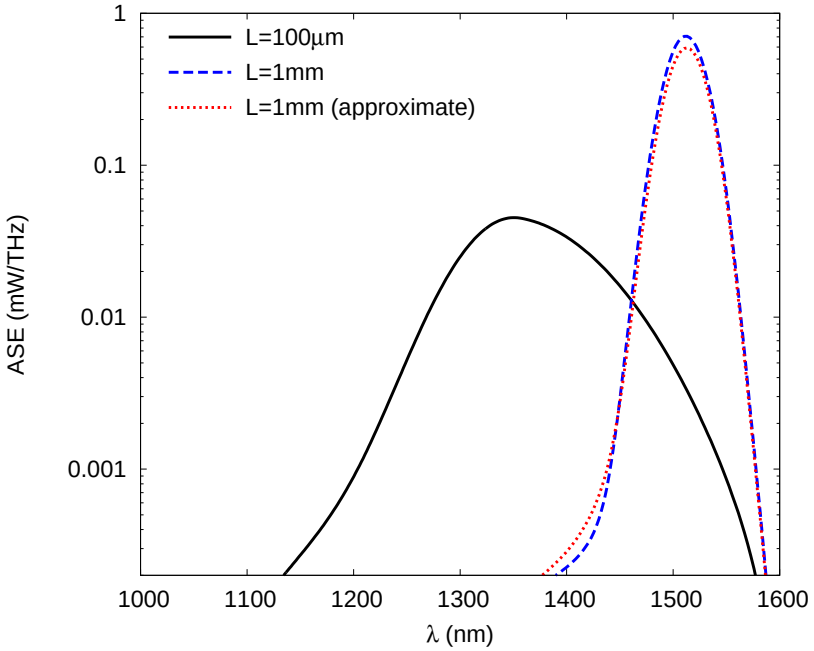

Figure 5.7: Facet ASE spectrum for different device lengths.

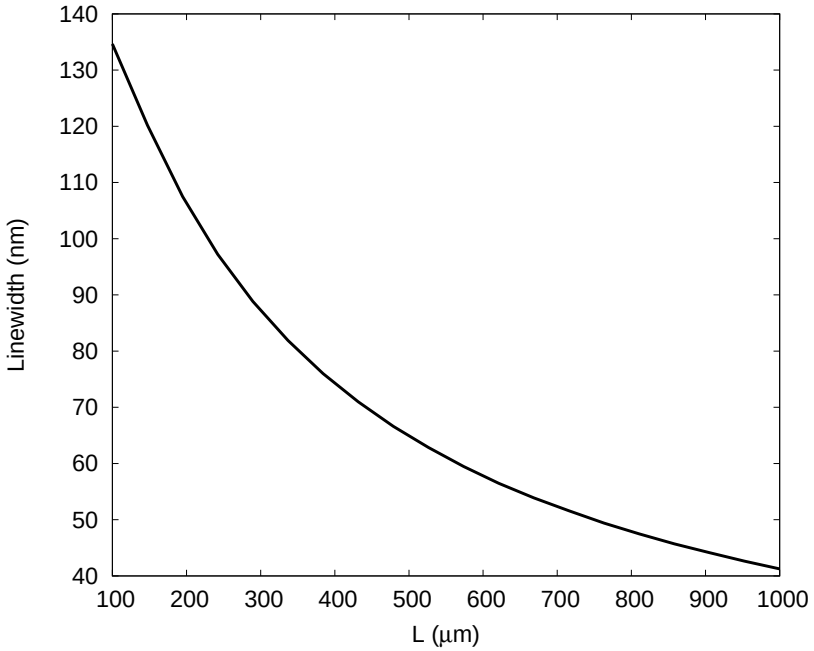

Figure 5.8: Linewidth of output light as a function of device length for the sample SLD.

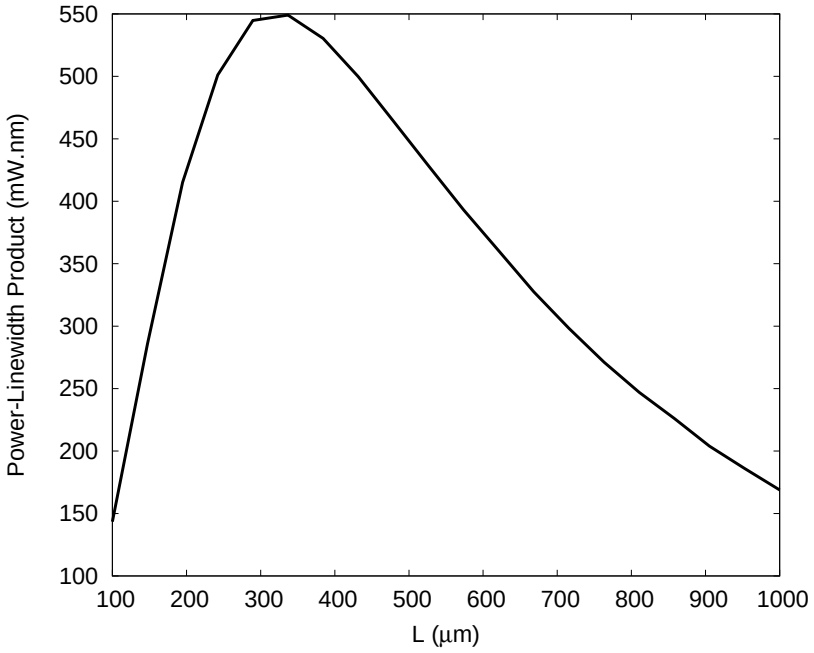

Figure 5.9: Power-linewidth product of output light versus device length for the sample SLD.

This shows that the device length should be chosen according to the demands of the application at hand.

Next we compare results of the discussed simulation method with the experimental results reported in [59] where three devices with the active region length $L = 250\,\mu m$ and thicknesses of $d = 0.15, 0.2$ and $0.25\,\mu m$ are fabricated and measured. Simulation parameters given in [59] are listed in Table (5.2). In the actual devices the right facets are cleaved ones, whereas, at the left end of the devices unpumped loss regions (referred to as window regions in [59]) are embedded. As a result, the right and left facet reflectivities are different. In our simulations instead of window regions the effective facet reflectivities presented by the window regions are considered for the left facet. Fig. 5.10 shows the output facet power of the three devices versus the injection current. Asterisks show the measured values. The spontaneous emission coupling

Table 5.2: Device parameters

L (μm)	0.15	0.2	0.25
α (cm^{-1})	28.7	49.3	68.8
R_r	10^{-4}	10^{-4}	10^{-4}
R_l	0.02	0.02	0.02
Γ	0.36	0.49	0.60
β	0.005	0.005	0.005

factor (β) and the confinement factor (Γ) are used as fitting parameters. At relatively low currents the agreement between simulation and experiment is reasonable, whereas, as the injection current increases the actual output power values drop due to the thermal effects of junction heating. Since the heating effects are not considered in our simulation model, simulation results start to depart from the measured values at these currents.

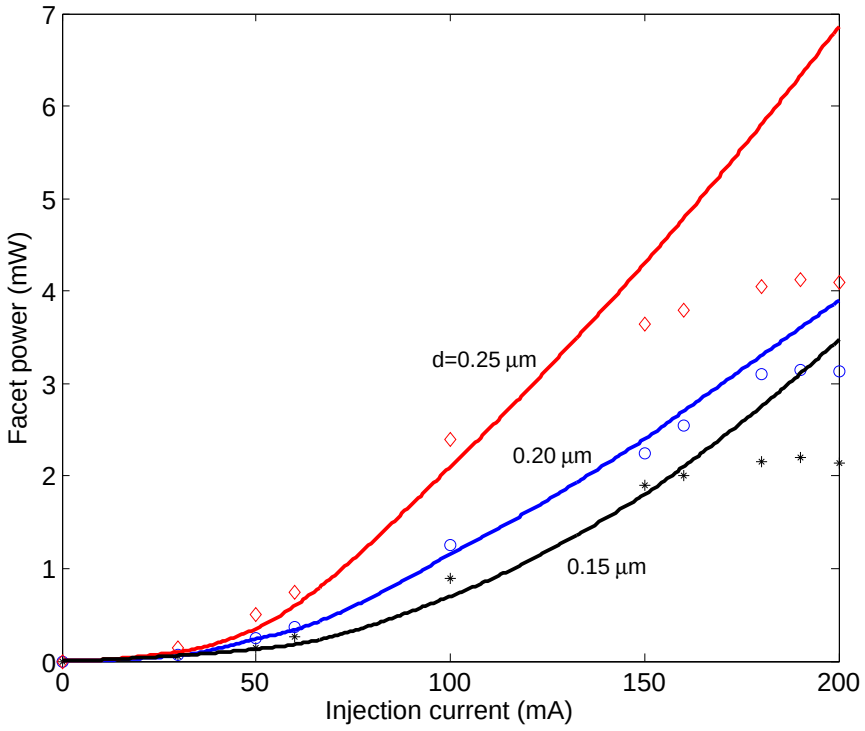

Figure 5.10: Power-linewidth product of output light versus device length for the sample SLD.

Chapter 6

The Proposed Device

In this chapter the proposed structure is presented and parameters important in device operation are investigated. Using the frequency-time-domain model introduced in the previous chapter the output characteristics of the proposed device ares discussed, comparison is made with conventional devices and the effect of structural parameters on the performance are investigated.

6.1 Proposed structure and the propagation loss

The schematic diagram of the cross section of the proposed structure is shown in Fig. 6.1, where a five layer SPWG is placed next to a QW active region. At each side of a metal film (M), there is a dielectric buffer layer (B). Considering the dielectric claddings (C), the structure is designated as CBMBC. The refractive index of buffer is higher than that of the claddings. Because the waveguide contains a metal film, charge carriers cannot be injected vertically. Instead, the p and n regions are proposed to be placed laterally giving rise to a horizontal current. This is known as the lateral

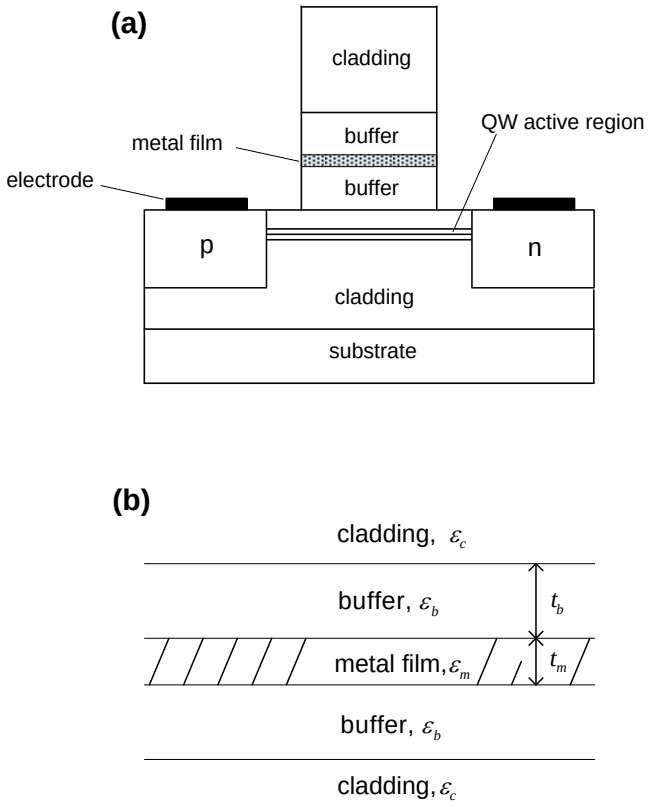

Figure 6.1: (a) Schematic cross section of the proposed SLD structure with SPWG incorporating lateral carrier injection (b) schematic structure of the SPWG stack.

injection scheme and has been used previously, e.g., by Ahn and Chuang [88] for a gain switched laser. In their device, a metal film was deposited as an electrode to apply electric field pulses across the active region. In our case, however, metal film is part of the SPWG. Similar to the three layer CMC (i.e., no buffer layers) waveguide, the five layer structure has two bounded TM surface plasmon modes, one symmetric (LRSP), and the other antisymmetric (SRSP).

Fig. 6.2 shows the mode index and loss coefficient of a CBMBC structure, in which refractive indices of claddings and buffers are 3.35 and 3.5, respectively. The dielectric function of the metal at 1.55 μm is taken to be $-116.38 - j11.1$. The

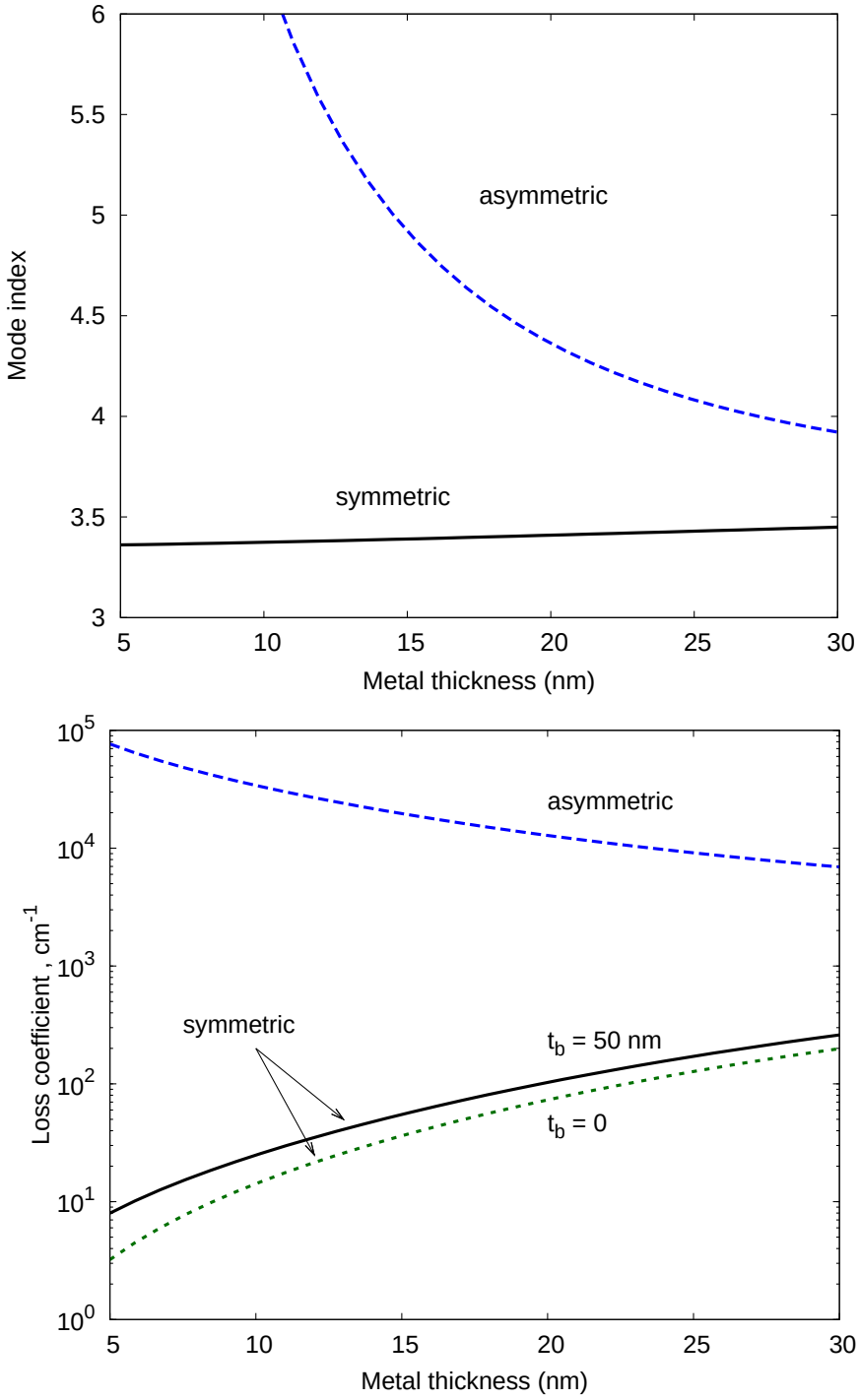

Figure 6.2: Mode index and loss coefficient of the proposed structure.

buffer layers are 50 nm thick. As expected, the asymmetric mode loss is huge ($> 10^4$ cm^{-1}), while for thin films the symmetric mode loss is tolerable (can be brought down to ~ 10 cm^{-1}). For reference, the symmetric mode loss of the corresponding CMC structure ($t_b = 0$) is also drawn in the figure. With the given refractive index of the buffer layers, the loss of the symmetric mode is higher than that of the CMC structure. Fig. 6.3 schematically shows the H field distribution of the two modes. It is very similar to the modal distribution of the CMC waveguide.

To see the effect of the thickness and refractive index of the buffer layers, in Fig. 6.4 the loss coefficient of the symmetric mode of the CBMBC waveguide is drawn as a function of buffer thickness with its refractive index as parameter. All the curves in the figure merge to the same value at zero buffer thickness, as they should, giving the loss coefficient of the CMC configuration. The curve corresponding to the buffer refractive index of 3.35 is flat, because the waveguide structure in this case is, again, CMC. For other buffer thicknesses, two different behaviours are seen with loss coefficients higher/lower than the loss of CMC waveguide depending on whether buffer index is higher/lower than the claddings refractive index. An interesting situation happens for any buffer refractive index smaller than the index of claddings: there is a cutoff buffer thickness above which, the symmetric mode cannot propagate. Near the cutoff thickness, the loss is arbitrarily small, as the electromagnetic field energy is taken away from the metal film and is concentrated more and more in the buffer.

This is fascinating for applications requiring low propagation loss, but there is also a high sensitivity to the film thickness around the cutoff point due to the large slope of the curve.

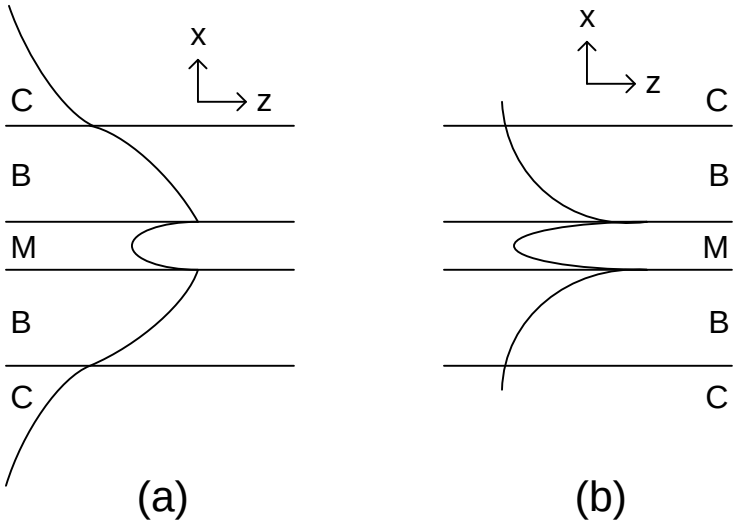

Figure 6.3: Symmetric and antisymmetric mode profiles of the proposed structure.

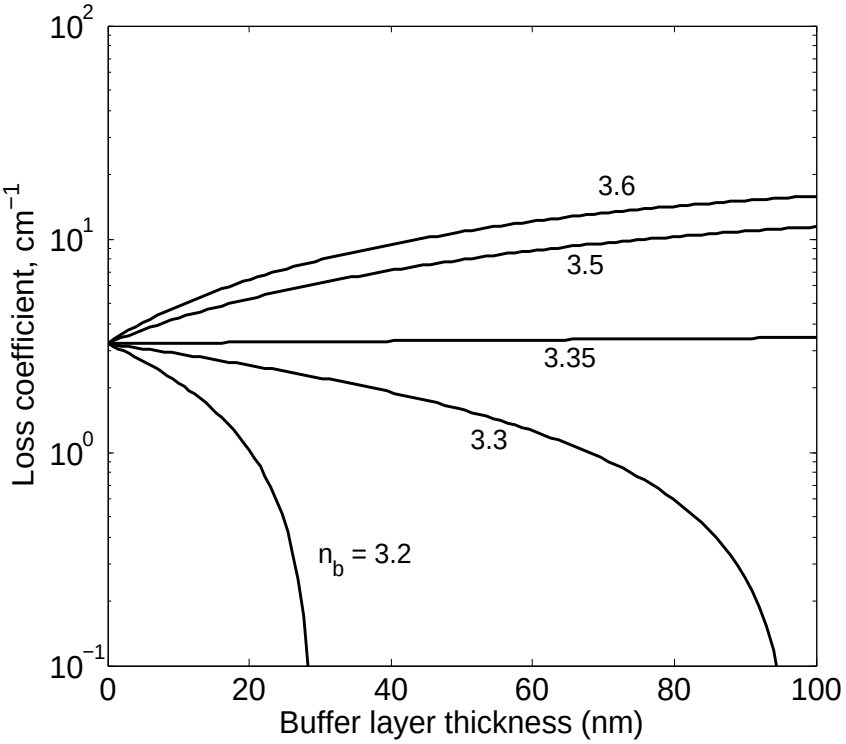

Figure 6.4: Loss coefficient vs buffer layers thickness for different values of buffer refractive index, $\epsilon_c = 11.2,\ t_m = 5\,\text{nm}$.

6.2 Confinement factor

In the proposed device, the active region is embedded in the cladding region at one side of the metal slab where modal fields decay exponentially away from the slab. The overlap of the active region with the tail of the modal field, which determines the confinement factor depends on the active region thickness and its separation from the metal slab, the metal slab thickness, and the depth of field penetration into the dielectric region. Here, the confinement factor is calculated from the overlap integral which gives the portion of the modal power density in the active region [89]

$$\Gamma = \frac{\mathrm{Re}\left\{\int_{A.R.} (E \times H^*) \cdot \hat{z}\, dx\right\}}{\mathrm{Re}\left\{\int_{C.S.} (E \times H^*) \cdot \hat{z}\, dx\right\}}$$

where z is assumed the direction of propagation and x the direction perpendicular to the waveguide layers. The integral in the numerator is calculated over the active region thickness and the integral in the denominator is calculated over the whole waveguide cross section. Figs. 6.5 and 6.6 show the confinement factor for the waveguide of Fig. 6.1. In Fig. 6.5, the abscissa is the thickness of the buffer layers and the refractive indicies of buffers are taken as parameters, whereas in Fig. 6.6 the buffer layers thickness and refractive index have changed roles. Metal film thickness is 5 nm. Active region is 10 nm thick and is placed 115 nm away from the metal film. Other parameters have remained unchanged. To see the effect of metal slab thickness on the confinement factor, the above two figures are reproduced for a metal

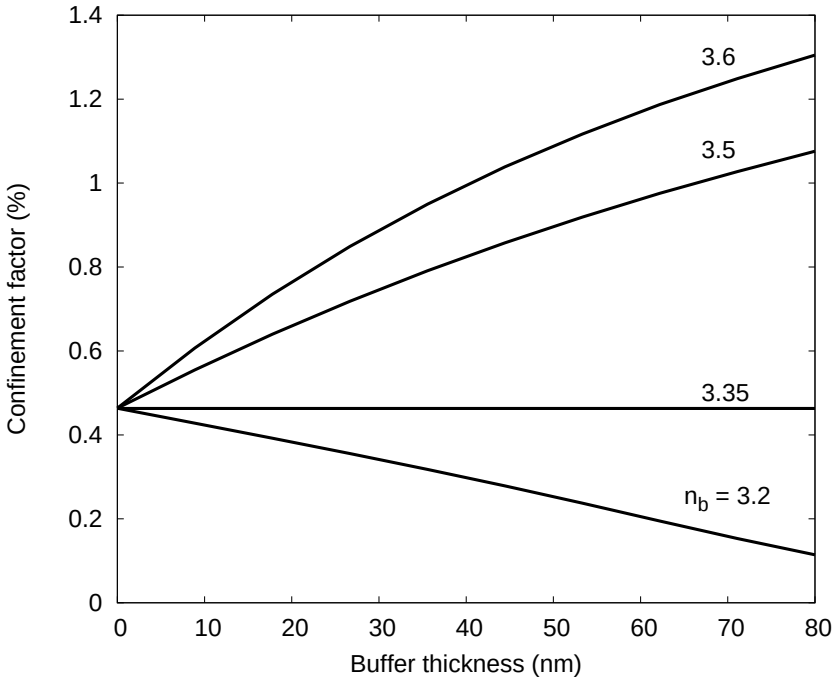

Figure 6.5: Confinement factor vs buffer layers thickness for different values of buffer refractive indices, $t_m = 5\,\text{nm},\ \epsilon_c = 11.2$.

thickness of 10 nm (Figs. 6.7 and 6.8). From the figures, the confinement factor increases with increasing the refractive indicies of buffers and with increasing the metal slab thickness. Also, the confinement factor increases as the buffer thickness increases only when the refractive index of buffer layers is larger than that of the claddings. Comparing with Fig. 6.4, the general behaviour of the confinement factor and the waveguide loss as functions of buffer layers refractive index and thickness are similar. This feature is desirable because it tries to balance the negative effect of loss on the device output power. These figures also show that the confinement factor for the proposed waveguide has typical values of the confinement factor in the conventional single quantum well devices with dielectric waveguide [90–92].

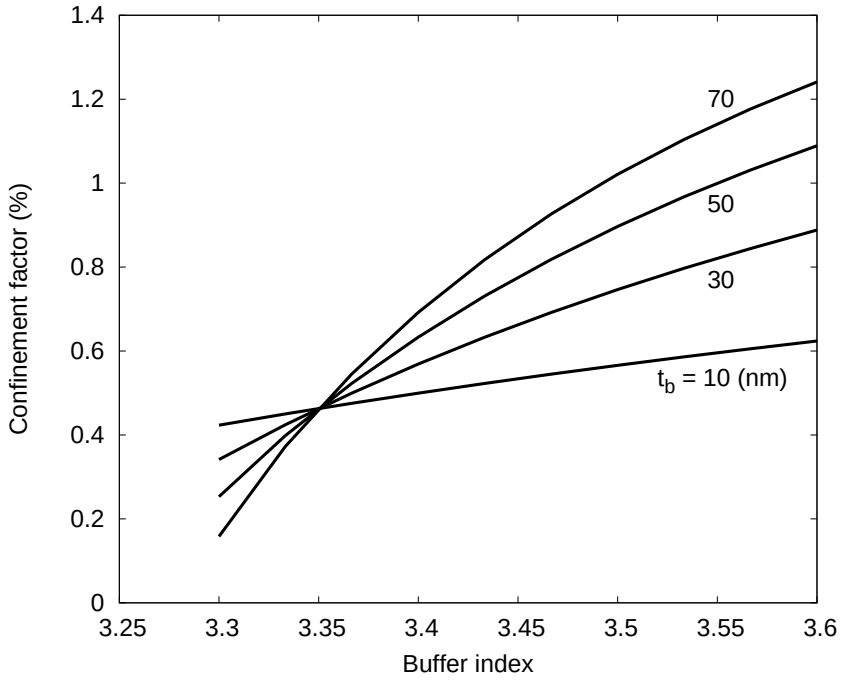

Figure 6.6: Confinement factor vs buffer layers refractive index for different values of buffer thicknesses, $t_m = 5\,\mathrm{nm},\ \epsilon_c = 11.2$.

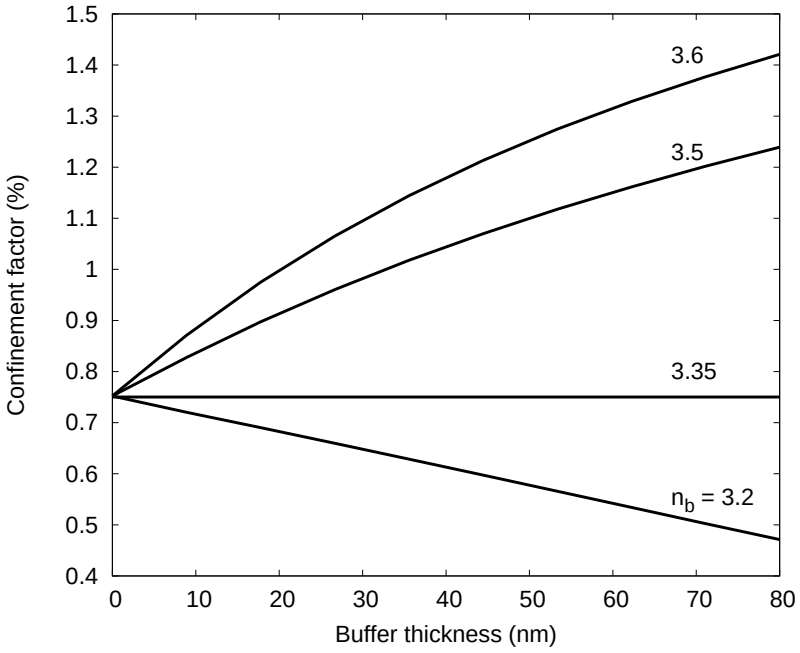

Figure 6.7: Confinement factor vs buffer layers thickness for different values of buffer refractive indices, $t_m = 10\,\text{nm}$, $\epsilon_c = 11.2$.

6.3 Spontaneous emission coupling factor

Spontaneous emission coupling factor (β) is calculated using the theory developed in Chapter 3 for an arbitrary layered structure near a dipole (Fig. 3.6). Dipole radiation contains plane wave components of all wave vectors. Large wave vector components (bigger than the wavevector in the dipole medium) do not propagate, but rather, decay away from the dipole. These evanescent components do not carry away average power, but if the layered structure nearby supports optical modes the evanescent components can excite the modes. In addition, there are radiation modes (here simply called radiation). For the waveguide structure of Fig. 6.1, it is expected to have different degrees of coupling to the 'drain channels', i.e., to the two SPP modes, as well as to the radiation modes. The percentage of dipole energy coupled to

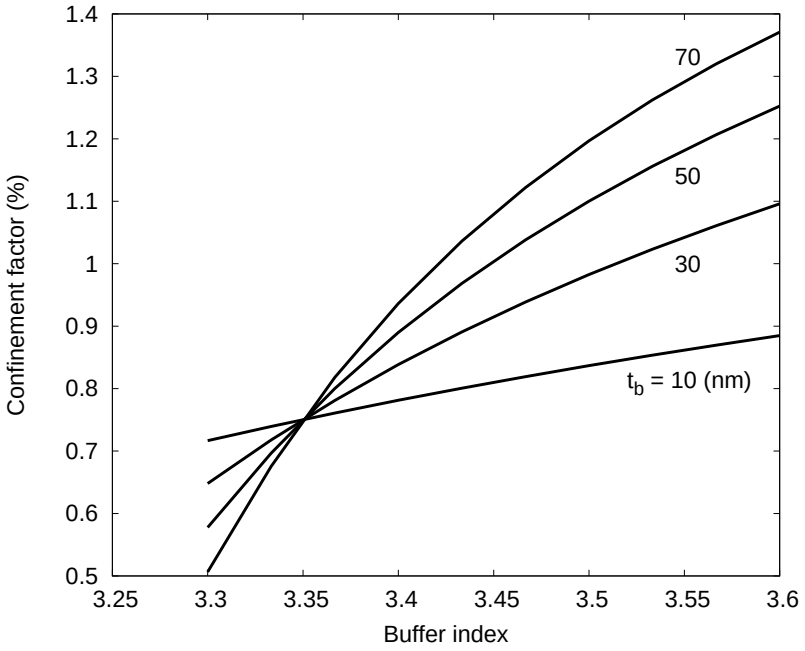

Figure 6.8: Confinement factor vs buffer layers refractive index for different values of buffer thicknesses, $t_m = 10\,\text{nm},\ \epsilon_\text{c} = 11.2$.

each drain channel depends on the structural parameters and the dipole orientation, and is obtained by using (3.44)-(3.47). The percentage of coupling to the guided modes is calculated by taking the pole contribution of the appropriate integrands of these equations.

Fig. 6.9 shows the coupling percentage of a perpendicularly oriented dipole near to the five layer SP waveguide as a function of dipole distance from the nearest interface. Coupling to radiation, symmetric (LRSP), and asymmetric (SRSP) are indicated. Metal film thickness is 5 nm. Buffer layers have a refractive index of 3.5 and thickness of 30 nm. For coupling to the symmetric mode two more curves corresponding to buffer thicknesses of 50 and 70 nm are also inserted. The coupling factor for the symmetric mode in the proposed SPWG structure can reach 40%, much higher than that in the conventional SLD structures (roughly 1%) and that is

the advantage of our surface plasmon waveguide over dielectric waveguides. However, the performances of the two devices are yet to be compared considering the higher loss of metallic waveguides. Similarly, coupling percentages for a parallel dipole are shown in Fig. 6.10. There is an utter difference in the coupling percentage to the symmetric mode between perpendicular and parallel dipoles, as seen from the figures. Therefore, it is needed to have excitons in the active region with fields resembling the perpendicular dipole. Coupling to the radiation modes increases monotonically as dipole distance increases, eventually claiming all the dipole energy. On the other hand, coupling to the asymmetric mode is significant only at short distances. Therefore, there is a peak for coupling to the symmetric mode which depends on the structure parameters. At a thickness of 30 nm for the buffer layers, the peak coupling is at a dipole distance of about 115 nm.

To see the effect of the thickness and refractive index of buffer layers on the coupling factor, Fig. 6.11 depicts the maximum coupling factor (of a symmetric mode) as a function of buffer layer index for several values of buffer thickness.

6.4 Facet reflection

For the waveguide structure of Fig. 6.1, a two-layer broadband AR facet coating was designed. The method described in Chapter 4 was used first to find a coating system with minimum reflectivity for plane waves. Then, the coating parameters were trimmed in the way to minimize the SPWG mode reflection (employing the Fourier decomposition of the waveguide mode). Fig. 6.12 shows the schematic and parameters of coating layers (thickness and refractive index). In Fig. 6.12 facet reflectivity versus wavelength of the designed coating system is drawn. The response is centred about a

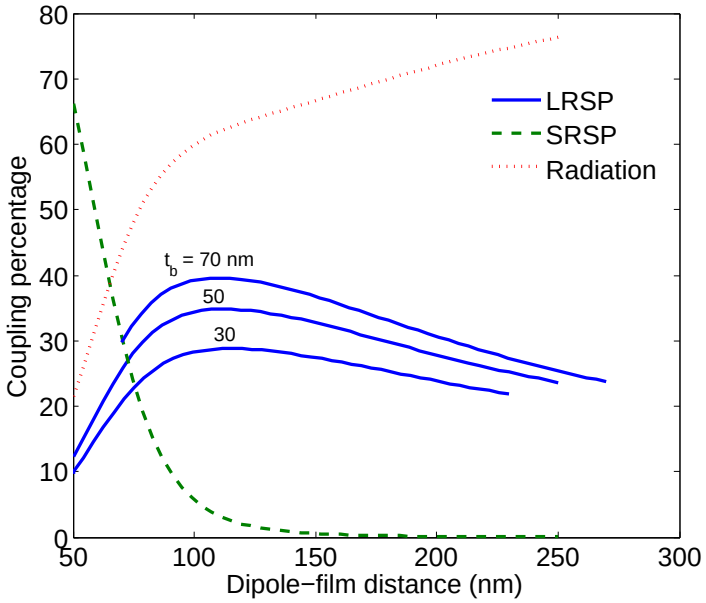

Figure 6.9: Spontaneous emission coupling percentage of perpendicular dipole to different optical channels, $\epsilon_b = 12.25$, $\epsilon_c = 11.2$, $t_m = 5\,\text{nm}$.

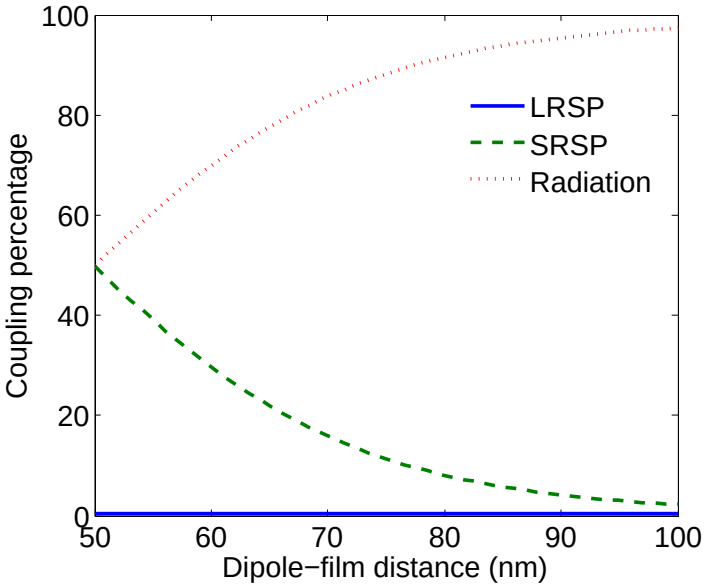

Figure 6.10: Spontaneous emission coupling percentage of parallel dipole to different optical channels, $\epsilon_b = 12.25$, $\epsilon_c = 11.2$, $t_m = 5\,\text{nm}$.

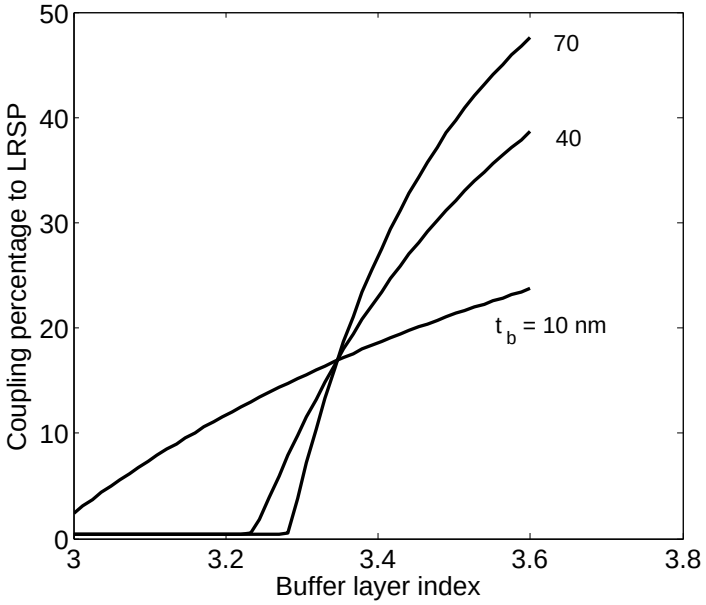

Figure 6.11: Spontaneous emission coupling factor (β) as a function of buffer layers refractive index for different values of buffer thicknesses, $\epsilon_b = 12.25$, $\epsilon_c = 11.2$, $t_m = 5\,\text{nm}$.

wavelength of 1550 nm and presents a reflectivity of less than 10^{-4} over a wavelength range of 135 nm. If reflectivities of less than 2×10^{-4} can be tolerated, the bandwidth is 145 nm. Utilizing a combination of reflection suppression techniques overviewed in Chapter 4 including AR coatings, ensures an acceptable broadband facet reflection needed for the operation of a wide band device such as ours.

6.5 Device performance

In this section the performances of SLDs with dielectric waveguide and SPWG are compared. Substituting different device parameters discussed so far in this chapter into the multi wavelength time domain method of the previous chapter, the output power and linewidth (or, spectral width) for each device is obtained. Of all the device

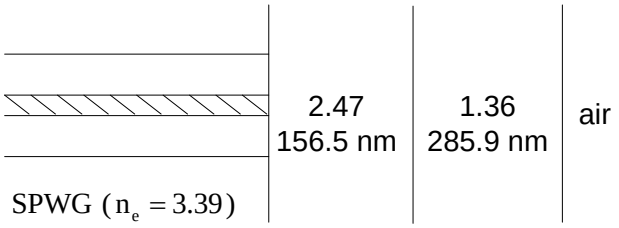

Figure 6.12: Schematic of the waveguide facet and the designed two-layer AR coating.

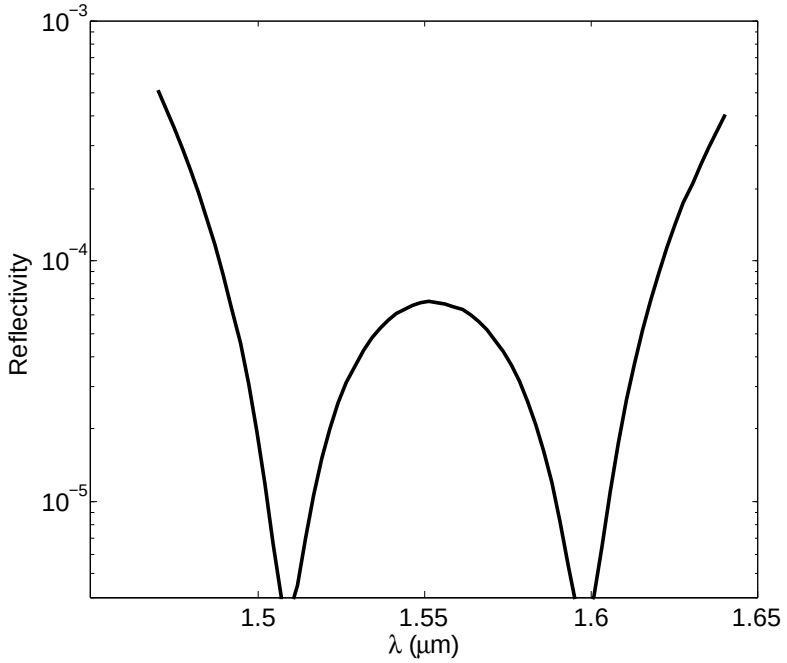

Figure 6.13: Reflectivity of facet with the designed AR coating.

parameters discussed so far the spontaneous coupling factor, β, has the largest difference between the dielectric waveguide and SPWG SLDs. Therefore, it is expected that β is responsible for most of the output light characteristic difference between the two types of SLDs.

Four SLD devices are considered, all with single quantum well (SQW) active regions. The first one (denoted as device 1) has a dielectric waveguide, whereas the other three (denoted as device 2, 3 and 4) are embedded with SPWGs. Metal film thickness of these devices is 5 nm and dielectric constant is $-116.38-j11.1$, as was for the previous simulations. The important parameters of the four devices are listed in table 6.1. The SPWG in device 2 does not include buffer layers; therefore, it models a simple thin film SPWG (CMC structure). The refractive index of buffer layers was chosen to be 3.5, close to the highest available index from InGaAsP material system. With higher index buffer layers, the spontaneous coupling factor will be even larger. A typical value of 5 cm^{-1} as the waveguide loss of quantum well devices was used for device 1. For the other three devices, the loss of device 1 was added to the loss value of the corresponding SPWG obtained from the analysis of section 6.1.

The spontaneous emission factor for device 1 is set to 1%, typically used in the literature [10, 78]. For the SPWG devices the high values given in section 6.3 are reached only if the excitons (dipoles) producing spontaneous emission in the active region are perpendicularly polarized. This is facilitated when the quantum well active region is made with a tensile strain. In that situation, up to 75% of the dipoles are assumed to acquire perpendicular polarization. As a result, the values of spontaneous coupling calculated in section 6.3 are multiplied by a factor of 75% to obtain the values given in table 6.1.

Table 6.1: Device parameters

	Device 1	Device 2	Device 3	Device 4
waveguide type	dielectric	SPWG		
buffer layers refractive index	-	3.5		
buffer layers thickness (nm)	-	0	50	100
cladding refractive index	-	3.35		
QW distance from metal film (nm)	-	$105 \sim 120$		
optical loss (cm^{-1})	5	8.2	13	16.3
spontaneous coupling factor (%)	1	12.75	26.25	34.5
confinement factor (%)	1			
wavelength (μm)	1.55			
injection current (mA)	100			

The four devices are compared at a constant injection current of 100 mA. Fig. 6.14 shows the output powers as functions of device length (i.e., active region length). As expected, all the curves reach a maximum at an optimal device length. Despite their considerably higher waveguide losses, SPWG devices have higher maximum powers than device 1, a direct consequence of their higher spontaneous coupling factor. But, their maximum powers are reached at shorter device lengths where the waveguide loss is smaller. For SPWG devices, loss quickly suppresses the output power as they become longer than their optimal lengths. Among the SPWG devices, device 2 has the highest maximum power because of its smallest loss as discussed in section 6.1.

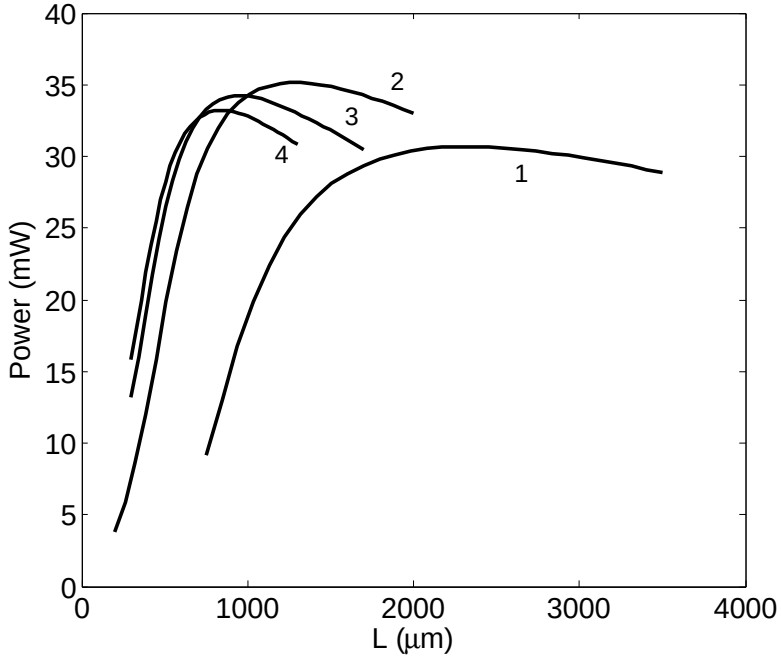

Figure 6.14: Output power versus device length for the four SLDs compared.

Fig. 6.15 compares the linewidth of the output light of the four devices. The linewidth values, especially, those of the SPWG devices are very close. They all decrease monotonically as device length increases. Therefore, as far as the linewidth is considered there is no advantage between the SPWG devices, and device 1 performs better than the rest do at equal device lengths. However, to obtain a higher output linewidth one needs to use shorter devices where the SPWG devices are in their peak power region while the output power of the dielectric waveguide device is much lower. This clearly indicates the superiority of devices 2 to 4 in applications where both power and linewidth of the output matter. They achieve higher power and broader spectral width at a shorter device length.

Another comparison of our devices is shown in Fig. 6.16 which is useful for applications in which maximizing the product of the output power and linewidth (PL

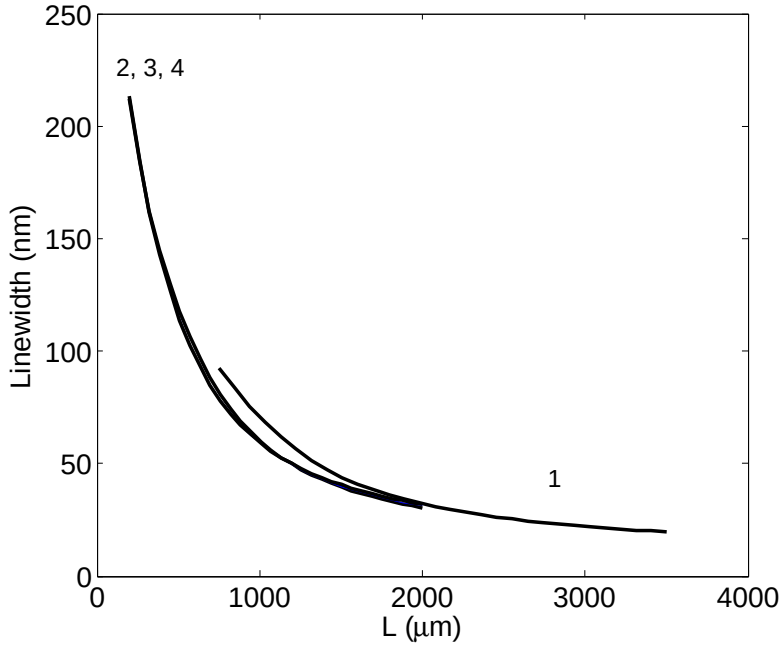

Figure 6.15: Output light linewidth versus device length for the four devices of Table.6.1.

product) is desired. In this comparison device 4 outperforms the others showing the advantage of utilizing the SPWG structure with buffer layers. At its peak of the PL product curve, device 4 offers higher power and at the same time broader linewidth but with a shorter device length among all the four devices investigated here. For a closer look consider Table 6.2, which compares device 1 and device 4 under two specific operating conditions: maximum output power and maximum PL product by values extracted from Figs. 6.14 to 6.16. The advantage of the SPWG device is inferred in both operating conditions. The difference is more pronounced for the linewidth and PL product. The key to achieving the highest PL product by device 4 is that it claims its maximum power at a shorter device length where the output light is broader. In other words, it takes advantage of the monotonically increasing feature of the linewidth characteristic as device becomes shorter.

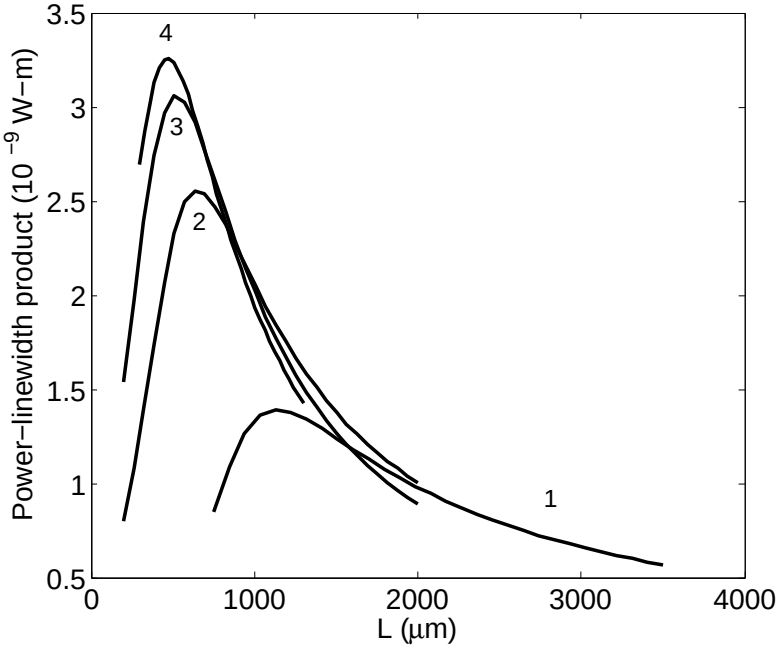

Figure 6.16: Power-linewidth product versus device length for the four devices of Table.6.1.

Table 6.2: device performance comparison

	Maximum power		Maximum power-linewidth product	
	Device 1	Device 4	Device 1	Device 4
Device length (μm)	2360	845	1130	470
Facet Power (mW)	30	33	22.5	27.5
Linewidth (nm)	27	71	62	120
PL product (mW-μm)	0.81	2.34	1.39	3.3

6.6 Effects of waveguide parameters

First, to find the effect of the refractive index and thickness of buffer layers on device performance the maximum output power and maximum power-linewidth product are calculated for different values of those parameters (see Fig. 6.17 and Fig. 6.18). The SPWG is symmetric in terms of geometry and refractive indices. It is clear that in order to have both higher power and PL product it is necessary to have high index buffer layers of several tens of nanometers. With high index buffer layers waveguide loss increases but spontaneous emission coupling factor and confinement factor also increase. As a result, a low-index-buffer waveguide is not suitable for the application at hand, although for only low propagation loss purposes it should be the choice. For the same reason, a similar SPWG structure in which high index dielectric slabs are placed along the metal film but separated from it by low index buffer layers on both sides of metal film is not suitable for the active device.

Now, the effect of the dielectric constant of claddings on waveguide parameters is discussed. Fig. 6.19 shows waveguide loss for a five layer SPWG as the refractive index of claddings varies for a number of buffer thickness values. The refractive index of buffers is set to 3.5. Parameters not mentioned remain as before. A number of points are revealed by Fig. 6.19. First, as expected, all curves meet at the cladding refractive index equal to that of buffer layers, because at this refractive index there is no distinction between buffer and cladding and the waveguide is actually a CMC structure. Over most of the index range below 3.5 the three traces show a similar trend, loss increases with the increase of cladding index. For structures with buffer layers when the index of claddings exceeds 3.5 the LRSP mode is vulnerable to being cutoff. This situation is similar to the one already shown in Fig. 6.4 where buffers have lower index

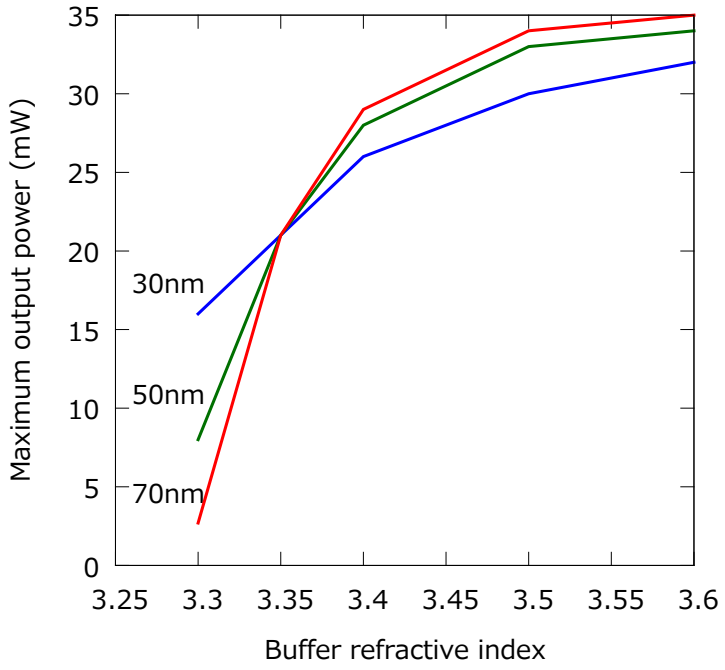

Figure 6.17: Maximum output power vs buffer layers refractive index of SPWG-SLD for different values of buffer thickness, $\epsilon_c = 11.2$.

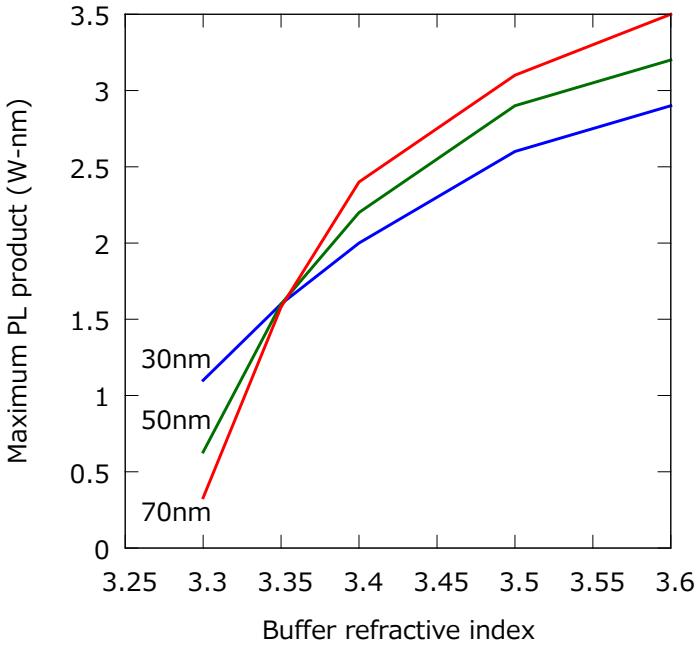

Figure 6.18: Maximum power-linewidth product of SPWG-SLD vs buffer layers refractive index for different values of buffer thickness, $\epsilon_c = 11.2$.

than claddings do. Near cutoff loss drops sharply. Hence, considering only waveguide loss, the cladding refractive index is preferred to either stay as small as possible or be carefully picked near its cutoff value. In practice, the smallest value is determined by the QW/barrier system and semiconductor lattice matching arguments. For the same SPWG considered, Fig. 6.20 shows the maximum value (over all dipole-metal film distances) of spontaneous coupling factor as a function of cladding refractive index. The general trend of traces is similar to that in previous figures, meaning that there is a tradeoff between dissipation and coupling factor. These figures predict a low device performance for CMC structures because of their low coupling factor or their high loss. In devices made of high index semiconductors (with the refractive index around 3), low index claddings and relatively thick buffers are preferred. The

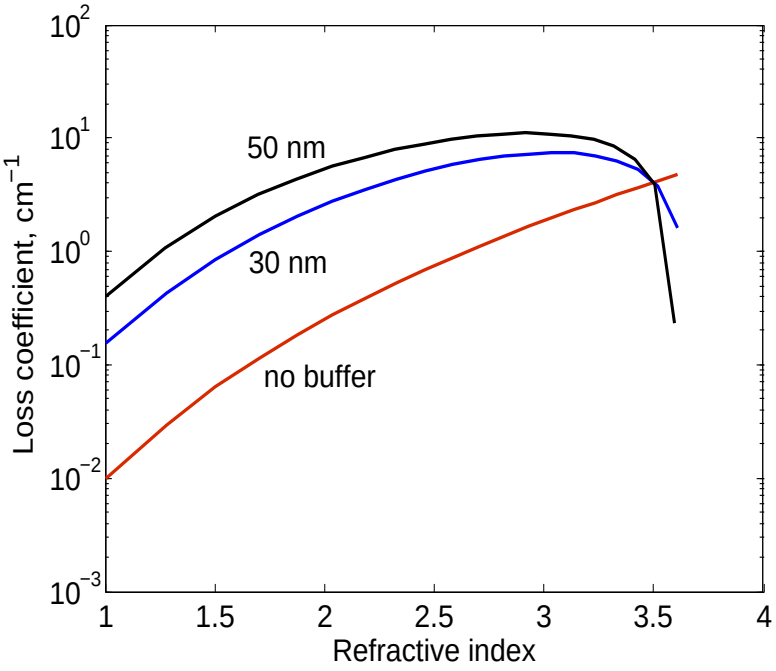

Figure 6.19: SP waveguide loss vs cladding refractive index for different values of buffer thickness, $\epsilon_b = 12.25$.

confinement factor for the same structure is shown in Fig. 6.21. Device performance as a function of the claddings refractive index is shown by Figs. 6.22 and 6.23.

6.6.1 Asymmetric structures

In the discussions above, only symmetric SPWG structures were considered, where claddings have the same refractive index and buffers have equal thickness and refractive index. As we know, an asymmetric structure has the issue of LRSP cutoff for high enough degree of asymmetry. In return, asymmetric structures can have a unique characteristic; if designed near cutoff, the LRSP mode has a very low loss. This is a very optimistic feature for applications requiring low loss. From the previous examples, however, low loss comes with the price of low spontaneous emission coupling

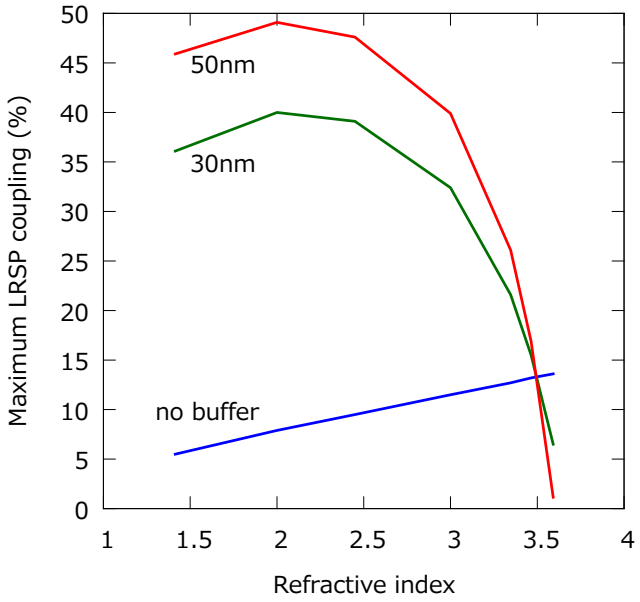

Figure 6.20: Maximum coupling to LRSP vs cladding refractive index for different values of buffer thickness, $\epsilon_b = 12.25$.

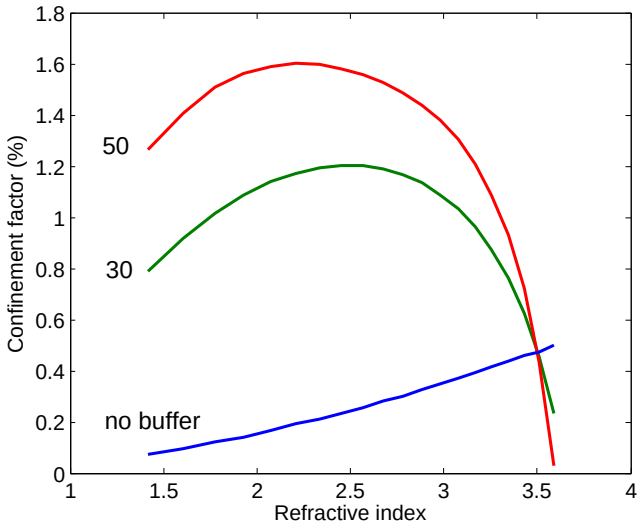

Figure 6.21: Confinement factor vs cladding refractive index for different values of buffer thickness, $\epsilon_b = 12.25$.

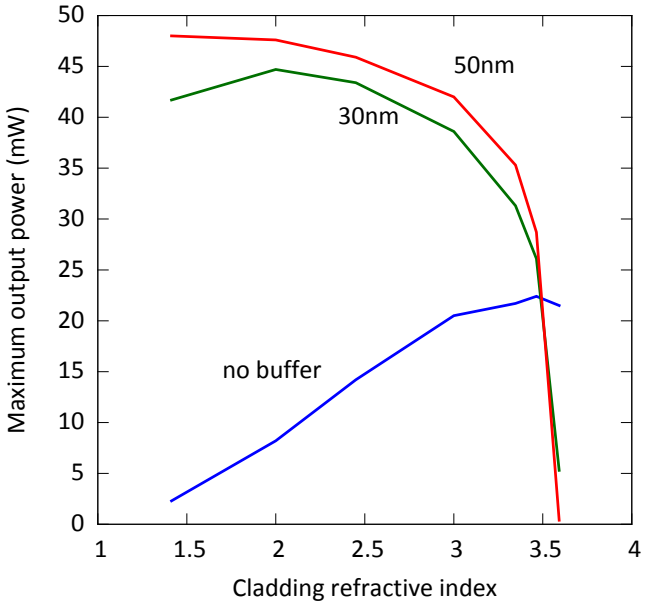

Figure 6.22: Maximum output power vs cladding refractive index for different values of buffer thickness.

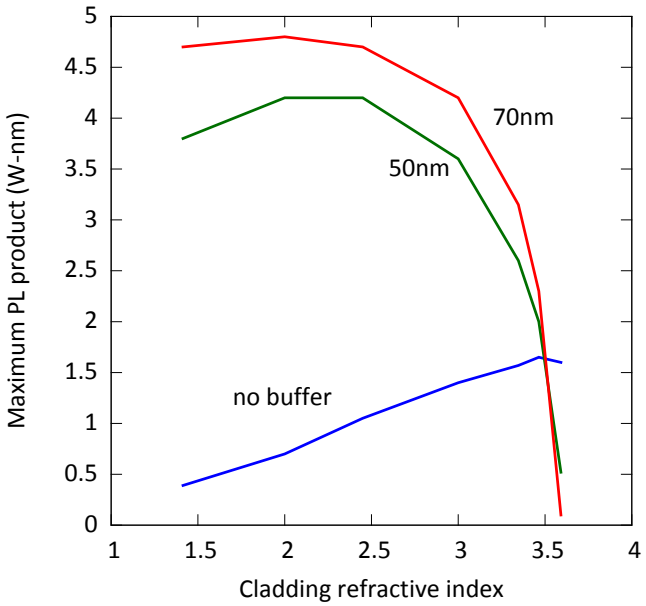

Figure 6.23: Maximum power-linewidth product vs cladding refractive index for different values of buffer thickness.

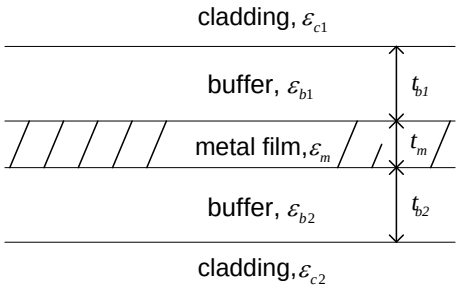

Figure 6.24: Five-layer asymmetric SPWG structure.

factor. With asymmetric structures it is occasionally possible to choose a structure with a high coupling factor and then introduce a small amount of asymmetry into the structure to control loss without a significant reduction in coupling factor. For example, referring to Fig. 6.24 when $\epsilon_{c1} = 10$, $\epsilon_{c2} = 11.2$, $t_{b1} = 110$ nm, $t_{b2} = 65$ nm, $\epsilon_{b1} = \epsilon_{b2} = 12.25$, $t_m = 5$ nm (silver at 1550 nm), the loss coefficient is as low as 1.5 cm^{-1} and spontaneous emission coupling factor is as high as 53%. While an SPWG with low loss and high coupling factor is advantageous for certain applications, one should also consider the confinement factor if it is meant to be implemented in an SLD. For the same parameters, unfortunately, the confinement factor is about 0.1%. This low confinement factor overruns the aforementioned benefits. A search (with several degrees of freedom) is needed to find any possible set of structural parameters which offers an improved performance over the symmetric structure for SPWG-SLD.

6.7 Conclusion

In order to investigate the idea of using a SPWG in SLD, I needed to gather several ingredients:

– Determining the loss and propagation constants of different SPWG modes. I did

this by first finding the dispersion equation using the transfer matrix method (TMM) [93] and solved it using the powerful and general argument principle method (APM) [94].

– Calculating the spontaneous emission coupling coefficient for the new type of waveguide. I borrowed the CPS theory as explained in Chapter 3 to find different decay rates and probabilities of a dipole near a planar structure. I had to rederive the formulas in the SI (rather than the Gaussian) unit system, and correct several mistakes or typos. Then, I proposed a relation relating the spontaneous emission coupling coefficient to the decay rates.

– Finding a wideband ARC system for the new type of waveguide with low enough reflectivity suitable for the nature of a device like SLD. From several proposed design methods in the literature that I tested, I chose the one represented in Chapter 4.

– Simulating the device performance using a model which takes the broadband nature of SLD into account. Calculating gain and spontaneous emission spectra, as well as different carrier recombination rates at each time step are required in solving the set of multiple coupled carrier and photon equations.

After testing several compositions, in Chapter 6 a multilayer SPWG structure is proposed, which allows for a large spontaneous coupling coefficient and acceptable propagation losses. The performances of several SPWG- and dielectric waveguide-SLDs were compared. The effects of some parameters on the output characteristics of SPWG SLDs were discussed and guidelines were given for optimizing a device for specific output requirements.

Appendix A

Derivation of equation (5.20) [1]

$$|E_f(z+\Delta z, t+\Delta t, \lambda_k)|^2 =$$

$$\left| \exp\left\{ -j\left[\gamma(\lambda_k) + \frac{1}{2}\Gamma\alpha_m g(z,t,\lambda_k)\right]\Delta z + \left[\frac{1}{2}(\Gamma g(z,t,\lambda_k) - \alpha)\right]\Delta z \right\} E_f(z,t,\lambda_k) + \right.$$

$$\left. \Delta z\sqrt{\beta\frac{R_{sp}(z,t,\lambda_k)}{\Delta z v_g}}\exp(j\phi) \right|^2 =$$

$$\left| \exp(j\theta)\exp\left\{ \left[\frac{1}{2}(\Gamma g(z,t,\lambda_k) - \alpha)\right]\Delta z \right\} |E_f(z,t,\lambda_k)| + \Delta z\sqrt{\beta\frac{R_{sp}(z,t,\lambda_k)}{\Delta z v_g}}\exp(j\phi) \right|^2 =$$

$$\left[\exp\left\{ \left[\frac{1}{2}(\Gamma g(z,t,\lambda_k) - \alpha)\right]\Delta z \right\} |E_f(z,t,\lambda_k)|\cos\theta + \Delta z\sqrt{\beta\frac{R_{sp}(z,t,\lambda_k)}{\Delta z v_g}}\cos\phi \right]^2 +$$

$$\left[\exp\left\{ \left[\frac{1}{2}(\Gamma g(z,t,\lambda_k) - \alpha)\right]\Delta z \right\} |E_f(z,t,\lambda_k)|\sin\theta + \Delta z\sqrt{\beta\frac{R_{sp}(z,t,\lambda_k)}{\Delta z v_g}}\sin\phi \right]^2 =$$

$$\exp\left\{(\Gamma g(z,t,\lambda_k) - \alpha)\Delta z\right\}|E_f(z,t,\lambda_k)|^2 + \Delta z\beta\frac{R_{sp}(z,t,\lambda_k)}{v_g} +$$

$$2\exp\left\{ \left[\frac{1}{2}(\Gamma g(z,t,\lambda_k) - \alpha)\right]\Delta z \right\} |E_f(z,t,\lambda_k)| \cdot \Delta z\sqrt{\beta\frac{R_{sp}(z,t,\lambda_k)}{\Delta z v_g}}\cos(\theta - \phi)$$

in which, $\theta = -\left[\gamma(\lambda_k) + \frac{1}{2}\Gamma\alpha_m g(z,t,\lambda_k)\right]\Delta z.$

Bibliography

[1] J. -W. Park, "Modeling, simulation and performance optimization of wide-band semiconductor optical amplifiers," Ph.D. dissertation, McMaster University, Hamilton, Canada, 2004.

[2] T. P. Li, C. A. Burrus and B. I. Miller, "A stripe-geometry double-heterostructure amplified-spontaneous-emission (superluminescent) diode," *IEEE J. Quantum Electron.*, vol. 9, pp. 820–828, 1973.

[3] G. A. Alphonse, D. B. Gilbert, M. G. Harvey and M. Ettenberg, "High-power superluminescent diodes," *IEEE J. Quantum Electron.*, vol. 24, pp. 2454–2457, 1988.

[4] T. Ko, D. Adler, J. Fujimoto, D. Mamedov, V. Prokhorov, V. Shidlovsky and S. Yakubovich, "Ultra high resolution optical coherence tomography imaging with a broadband superluminescent diode light source," *Optics Express*, vol. 12, pp. 2112–2119, 2004.

[5] W. K. Burns, C. L. Chen and R. P. Moeller, "Fiber-optic gyroscopes with broad band sources," *OSA/IEEE J. Lightw. Technol.*, vol. 1, p. 98, 1983.

[6] S. W. James and R. P. Tatam, "Optical fibre long-period grating sensors: characteristics and application," *Meas. Sci. Technol.*, vol. 14, p. 49, 2003.

[7] A. F. Brooks, T. L. Kelly, P. J. Veitch and J. Munch, "Ultra-sensitive wavefront measurement using a hartmann sensor," *Optics Express*, vol. 15, pp. 10 370–10 375, 2007.

[8] G. A. Alfonse and M. Toda, "Mode coupling in angled facet semiconductor optical amplifiers and superluminescent diodes," *OSA/IEEE J. Lightw. Technol.*, vol. 10, pp. 215–219, 1992.

[9] N. S. K. Kwong, K. Y. Lau, N. Bar-Chaim, I. Ury and K. J. Lee, "High power, high efficiency window buried heterostructure gaalas superluminescent diode with an integrated absorber," *Appl. Phys. Lett.*, vol. 51, p. 1879, 1987.

[10] J.W. Park and X. Li, "Theoretical and numerical analysis of superluminescent diodes," *OSA/IEEE J. Lightw. Technol.*, vol. 24, pp. 2473–2480, 2006.

[11] M. J. Hamp and D. T. Cassidy, "Critical design parameters for engineering broadly tunable asymmetric multiple-quantum-well lasers," *IEEE J. Quantum Electron.*, vol. 36, pp. 978–983, 2000.

[12] C. -F. Lin and B. -L. Lee, "Extremely broadband algaas/gaas superluminescent diodes," *Appl. Phys. Lett.*, vol. 71, pp. 1598–1600, 1997.

[13] J. Dakin and R. G. W. Brown, *Handbook of optoelectronics*. New York: Taylor & Francis, 2006.

[14] W. L. Barnes, A. Dereux and T. W. Ebbesen, "Surface plasmon subwavelength optics," *Naure*, vol. 424, pp. 824–830, 2003.

[15] Maier, "Plasmonics: metal nanostructures for subwavelength photonic devices," *IEEE J. Sel. Topics Quantum Electron.*, vol. 12, pp. 1214–1220, 2006.

[16] H. Raether, *Surface plasmons on smooth and rough surfaces and on gratings*. Berlin: Springer-Verlag, 1998.

[17] R. Zia, M. D. Selker, P. B. Catrysse and M. L. Brongersma, "Geometries and materials for subwavelength surface plasmon modes," *J. Opt. Soc. Amer. A*, vol. 21, pp. 2442–2446, 2004.

[18] J. Takahara, S. Yamagishi, H. Taki, A Morimoto and T. Kobayashi, "Guiding of a one-dimensional optical beam with nanometer diameter," *Optics Lett.*, vol. 22, pp. 475–477, 1997.

[19] T. W. Koo, S. Chan and A. A. Berlin, "Single-molecule detection of biomolecules by surface-enhanced coherent anti-stokes raman scattering," *Optics Lett.*, vol. 30, pp. 1024–1026, 2005.

[20] B. Rothenhausler and W. Knoll, "Surface-plasmon microscopy," *Nature*, vol. 232, pp. 615–617, 1998.

[21] Z. Liu, Y. Wang, J. Yao, H. Lee, W. Srituravanich and X. Zhang, "Broad band two-dimensional manipulation of surface plasmons," *Nano Lett.*, vol. 9, pp. 462–466, 2009.

[22] M. Quinten, A. Leitner, J. R. Krenn and F. R. Aussenegg, "Electromagnetic energy transport via linear chains of silver nanoparticles," *Optics Lett.*, vol. 23, pp. 1331–1333, 1998.

[23] S. Maier, M. L. Brongersma, P. G. Kik, S. Meltzer, A. A. G. Requicha and H. A. Atwater, "Plasmonics- a route to nanoscale optical devices," *Adv. Mater.*, vol. 13, pp. 1501–1505, 2001.

[24] K. H. Yoon, M. L. Shuler and S. J. Kim, "Design optimization of nano-grating surface plasmon resonance sensors," *Optics Express*, vol. 14, pp. 4842–4849, 2006.

[25] J. J. Burke, G. I Stegeman, T Tamir, "Surface-plasmon-like waves guided by thin, lossy metal films," *Phys. Rev. B*, vol. 33, pp. 5186–5201, 1986.

[26] S. J. Al-Bader and M. Imtaar, "Azimuthally uniform surface-plasma modes in thin metallic cylindrical shells," *IEEE J. Quantum Electron.*, vol. 28, pp. 525–533, 1992.

[27] ——, "Optical fiber hybrid-surface plasmon polaritons," *J. Opt. Soc. Am. B*, vol. 10, pp. 83–88, 1993.

[28] P. Berini, "Optical waveguide structures," U.S. patent 6,741,782, May 25, 2004.

[29] M. S. Tomaš and Z. Lenac, "Long-range surface polaritons in a supported thin metallic slab," *Solid State Commun.*, vol. 50, pp. 915–918, 1984.

[30] ——, "Coupled surface polariton with guided wave polariton modes in asymmetric metal clad dielectric waveguides," *Opt. Commun.*, vol. 55, pp. 267–270, 1985.

[31] Z. Lenac and M. S. Tomaš, "Attenuation of long-range surface polaritons in a thin metallic slab with a dielectric coating," *Surf. Sci.*, vol. 154, pp. 639–657, 1985.

[32] F. Yang, Z. Cao, L. Ruan, and J. Fang, "Long-range surface modes of metalclad four-layer waveguides," *Appl. Opt.*, vol. 25, pp. 3903–3908, 1986.

[33] J. Guo and R. Adato, "Extended long range plasmon waves in finite thickness metal film and layered dielectric materials," *Opt. Express*, vol. 14, pp. 12 409–12 418, 2006.

[34] R. Adato and J. Guo, "Characteristics of ultra-long range surface plasmon waves at optical frequencies," *Opt. Express*, vol. 15, pp. 5008–5017, 2007.

[35] J. T. Kim, "Characteristics analysis of hybrid plasmonic waveguide for low-loss lightwave guiding," *Opt. Commun.*, May 2011.

[36] B. Yun, G. Hu, and Y. Cui, "Bound modes analysis of symmetric dielectric loaded surface plasmon-polariton waveguides," *Opt. Express*, vol. 17, pp. 3610–3618, 2009.

[37] P. Berini, "Plasmon-polariton modes guided by a metal film of finite width bounded by different dielectrics," *Opt. Express*, vol. 7, pp. 329–335, 2000.

[38] ——, "Plasmon-polariton waves guided by thin lossy metal films of finite width: bound modes of asymmetric structures," *Phys. Rev. B*, vol. 63, p. 125417, 2001.

[39] ——, "Plasmon-polariton modes guided by a metal film of finite width," *Opt. Lett.*, vol. 24, pp. 1011–1013, 1999.

[40] ——, "Plasmon-polariton waves guided by thin lossy metal films of finite width: bound modes of symmetric structures," *Phys. Rev. B*, vol. 61, pp. 10 484–10 503, 2000.

[41] R. Charbonneau, P. Berini, E. Berolo, and E. Lisicka-Skrzek, "Experimental observation of plasmon-polariton waves supported by a thin metal film of finite width," *Opt. Lett.*, vol. 25, pp. 844–846, 2000.

[42] A. Degiron, C. Dellagiacoma, J. C. McIlhargey, G. Shvets, O. J. F. Martin, and D. R. Smith, "Simulations of hybrid long-range plasmon modes with application to 90° bends," *Opt. Lett.*, vol. 32, pp. 2354–2356, 2007.

[43] J. Guo and R. Adato, "Control of 2d plasmon-polariton mode with dielectric nanolayers," *Opt. Express*, vol. 16, pp. 1232–1237, 2008.

[44] R. Adato and J. Guo, "Modification of dispersion, localization, and attenuation of thin metal stripe symmetric surface plasmon-polariton modes by thin dielectric layers," *J. Appl. Phys.*, vol. 105, p. 034306, 2009.

[45] J. Gosciniak, T. Holmgaard, and S. I. Bozhevolnyi, "Theoretical analysis of long-range dielectric-loaded surface plasmon polariton waveguides," *OSA/IEEE J. Lightw. Tachnol.*, vol. 29, pp. 1473–1481, 2011.

[46] J. Carroll, *Distributed feedback semiconductor lasers*. London: IEE Press, 1998.

[47] R. R. Chance, A. Prock and R. Silbey, "Comments on the classical theory of energy transfer," *J. Chem. Phys.*, vol. 62, pp. 2245–2253, 1975.

[48] H. Kuhn, "Classical aspects of energy transfer in molecular systems," *J. Chem. Phys.*, vol. 53, pp. 101–108, 1970.

[49] R. R. Chance, A. Prock and R. Silbey, "Lifetime of an emitting molecule near a partially reflecting surface," *J. Chem. Phys.*, vol. 60, pp. 2744–2748, 1974.

[50] G. W. Ford and W. H. Weber, "Electromagnetic interactions of molecules with metal surfaces," *Phys. Rep.*, vol. 113, pp. 195–287, 1984.

[51] R. E. Collin, *Field theory of guided waves*, 2nd ed. New York: IEEE press, 1991.

[52] P. L. Takunja, "Electromagnetic surface wave propagation applicable to ultra-high energy neutrino detection," Master's thesis, Swidish Institute of Space Physics, Uppsala, Sweden, 2007.

[53] J. R. Wait, "Characteristics of antennas over lossy earth," in *Antenna theory*, R. E. Collin and F. J. Zucker, Ed. New York: McGraw-Hill, 1969.

[54] J. D. Jackson, *Classical Electrodynamics*. New York: John Wiley and Sons, 1999.

[55] R. R. Chance, A. Prock and R. Silbey, "Molecular fluorescence and energy transfer near interfaces," *Adv. Chem. Phys.*, vol. 37, pp. 1–65, 1978.

[56] W. L. Barnes, "Electromagnetic crystals for surface plasmon polaritons and the extraction of light from emissive devices," *OSA/IEEE J. Lightw. Technol.*, vol. 17, pp. 2170–2182, 1999.

[57] C. -T. Tai, *Dyadic green functions in Electromagnetic theory*. Oxford: Oxford University Press, 1995.

[58] R. R. Chance, A. Prock and R. Silbey, "A new probe for the surface electronic structure of liquid metals," *Solid State Comm.*, vol. 18, pp. 1259–1261, 1976.

[59] Y. Kashima, A. Matoba and H. Takano, "Performance and reliability of ingaasp superluminescent diode," *OSA/IEEE J. Lightw. Technol.*, vol. 10, pp. 1644–1649, 1992.

[60] C. E. Zah, J. S. Osinsky, C. Caneau, S. G. Menocal, L. A. Reith, J. Salzman, F. K. Shokoohi and T. P. Lee, "Fabrication and performance of 1.5um gainasp travelling-wave laser amplifiers with angled facets," *Electron. Lett.*, vol. 23, pp. 990–992, 1987.

[61] N. K. Dutta and Q. Wang, *Semiconductor Optical Amplifiers*. New Jersey: World Scientific, 2006.

[62] K. Utaka, S. Akiba, K. Sakai and Y. Matsushima, "Effect of mirror facets on lasing characteristics of distributed feedback ingaasp/inp laser diode at 1.5 um range," *IEEE J. Quantum Electron.*, vol. 20, pp. 236–245, 1984.

[63] I. Cha, M. Kitamura and I. Mito, "1.5 um band travelling-wave semiconductor optical amplifiers with window facet structure," *Electron. Lett.*, vol. 25, pp. 242–243, 1989.

[64] M. S. Lin, A. B. Piccirilli, Y. Twu and N. K. Dutta, "Fabrication and performance characteristics of buried-facet optical amplifiers," *J. Appl. Phys.*, vol. 67, pp. 3943–3947, 1990.

[65] I. M. Joindot and C. Y. Biosrobert, "Peculiar features of ingaasp dh superluminescent diodes," *IEEE J. Quantum Electron.*, vol. 25, pp. 1659–1665, 1989.

[66] K.Gen-ei, A. Tanioka, H. Suhara and K. Chinen, "High coupled power 1.3um

edge-emitting light-emitting diode with rear window and an integrated absorber," *Appl. Phys. Lett.*, vol. 53, pp. 1138–1140, 1988.

[67] H. Nagai, Y. Naguchi and S. Sudo, "High-power high-efficiency, 1.3um superluminescent diode with a buried bent absorbing guide structure," *Appl. Phys. Lett.*, vol. 54, pp. 1719–1721, 1989.

[68] H. A. Macleod, *Thin-film optical filters*. Bristol: Adam Hilger Ltd, 1986.

[69] M. Born and E. Wolf, *Principles of optics*. Cambridge: Cambridge University Press, 1999.

[70] R. H. Clarke, "Theoretical performance of anti-reflection coating for a diode laser amplifier," *Int. J. Electronics*, vol. 53, pp. 495–499, 1982.

[71] T. Saitoh, T. Mukai and O. Mikami, "Theoretical analysis and fabrication of antireflection coatings on laser-diode facets," *OSA/IEEE J. Lightw. Technol.*, vol. 3, pp. 288–293, 1985.

[72] C. Vassallo, "Theory and paractical calculation of antireflection coatings on semiconductor laser diode optical amplifiers," *Proceedings IEE*, vol. 137, pp. 193–202, 1990.

[73] T. J. Menne, "Analysis of the uniform rate equation model of laser dynamics," *IEEE J. Quantum Electron.*, vol. 2, pp. 38–44, 1966.

[74] G. P. Agrawal, *Fiber-Optic Communication Systems*. New York: Wiley-Interscience, 2002.

[75] S. F. Yu, "A quasi-three-dimensional large-signal dynamic model of distributed feedback lasers," *IEEE J. Quantum Electron.*, vol. 32, pp. 424–432, 1996.

[76] W. Li, W. -P. Huang and X. Li, "Multiwavelength gain-coupled dfb laser cascade: design modeling and simulation," *IEEE J. Quantum Electron.*, vol. 36, pp. 1110–1116, 2000.

[77] ——, "Digital filter approach for simulation of a complex integrated laser diode based on the traveling-wave model," *IEEE J. Quantum Electron.*, vol. 40, pp. 473–480, 2004.

[78] J. L. Pleumeekers, M. -A. Dupertuis, T. Hessler, P. E. Selbmann, S. Haacke and B. Deveaud, "Longitudinal spatial hole burning and associated nonlinear gain in gain-clamped semiconductor optical amplifiers," *IEEE J. Quantum Electron.*, vol. 34, pp. 879–886, 1996.

[79] M. J. Connelly, "Wideband semiconductor optical amplifier steady-state numerical model," *IEEE J. Quantum Electron.*, vol. 37, pp. 439–447, 2001.

[80] ——, "Wideband dynamic numerical model of a tapered buried ridge stripe semiconductor optical amplifier gate," *IEE Proc. -Circuits Devices Syst.*, vol. 149, pp. 173–178, 2002.

[81] J. W. Park, X. Li and W. -P. Huang, "Performance simulation and design optimization of gain-clamped semiconductor optical amplifiers based on distributed bragg reflectors," *IEEE J. Quantum Electron.*, vol. 39, pp. 1415–1423, 2003.

[82] ——, "Comparative study of mixed frequency-time-domain models of semiconductor laser optical amplifiers," *IEE Proceedings- Optoelectron.*, vol. 152, pp. 151–159, 2005.

[83] G. P. Agrawal and N. K. Dutta, *Semiconductor Lasers*. New York: Van Nostrand Reinhold, 1993.

[84] X. Li, *Optoelectronic Devices: Design, Modeling and Simulation*. Cambridge: Cambridge University Press, 2009.

[85] W. H. Press, B. P. Flannery, S. A. Teukolsky and W. T. Vetterling, *Numerical Recipes: The Art of Scientific Computing*. Cambridge, MA: Cambridge University Press, 1986.

[86] S. L. Chuang, *Physics of Optoelectronic Devices*. New York: Wiley-Interscience, 1995.

[87] L. M. Zhang, S. F. Yu, M. C. Nowell, D. D. Marcenac, J. E. Carroll and R. G. S. Plumb, "Dynamic analysis of radiation and side-mode suppression in a second-order dfb laser using time-domain large-signal traveling wave model," *IEEE J. Quantum Electron.*, vol. 30, pp. 1389–1395, 1994.

[88] D. Ahn and S. L. Chuang, "A field-effect quantum-well laser with lateral current injection," *Appl. Phys.*, vol. 64, pp. 440–442, 1988.

[89] L. A. Coldren and S. W. Corzine, *Diode lasers and photonic integrated circuits*. New York: Wiley-Interscience, 1995.

[90] P. S. Zory and A. R. Reisinger, "Anomalous length dependence of threshold for

thin quantum well algaas diode lasers," *Electron. Lett.*, vol. 22, pp. 475–476, 1986.

[91] M. F. Khodr, P. J. McCann and B. A. Mason, "Optimizing and engineering euse–$pbse_{0.78}te_{0.22}$–euse multiple-quantum-well laser structures," *IEEE J. Quantum Electron.*, vol. 34, pp. 1604–1611, 1998.

[92] U. T. Schwarz, K. Kojima, S. Nagahama and T. Mukai, "Investigation and comparison of optical gain spectra of (al,in)gan laser diodes emitting in the 375 nm to 470 nm spectral range," *Proc. SPIE*, vol. 6485, pp. 648 506–1—648 606–10, 2007.

[93] J. Chilwell and I. Hodgkinson, "Thin-films field-transfer matrix theory of planar multilayer waveguides and reflection from prism-loaded waveguides," *J. Opt. Soc. Amer. A*, vol. 1, pp. 742–753, 1984.

[94] C. Chen, P. Berini, D. Feng, S. Tanev and V. Tzolov, "Efficient and accurate numerical analysis of multilayer optical waveguides in lossy anisotropic media," *Optics Express*, vol. 7, pp. 260–272, 2000.